UNIVERSITY OF CALIFORNIA SAN DIEGO

The mechanics of flow, contractility and adhesion in soft-bodied locomotion

A dissertation submitted in partial satisfaction of the
requirements for the degree
Doctor of Philosophy

in

Engineering Sciences (Mechanical Engineering)

by

Shun Zhang

Committee in charge:

Professor Juan Carlos del Álamo, Chair
Professor Richard Firtel
Professor Robert Guy
Professor Juan Lasheras
Professor Qiang Zhu

2018

The dissertation of Shun Zhang is approved, and it is acceptable in quality and form for publication on microfilm or electronically:

Chair

University of California, San Diego

2018

EPIGRAPH

这家伙很懒，什么都没有留下。

TABLE OF CONTENTS

LIST OF FIGURES

LIST OF TABLES

ACKNOWLEDGEMENTS

There are so many of people whom I would like to acknowledge for helping me achieve the success of my Ph.D. research and made these last six years an unforgettable life-changing journey.

First of all, I want to thank my advisor, Juan Carlos del Álamo. Without him, none of what you are reading would have been possible. I'm deeply grateful for Juan Carlos offering me such precious opportunity to conduct research in this amazing lab, and open the gate for my academic career. He is a model for me to follow for his professional, passionate and vigorous attitude towards science. During this journey, there were also hesitations, difficulties, and sometimes non of the experimental methods work. His advice, support and encouragement means a lot to me to go through these hard times.

Thanks to Richard Firtel, Robert Guy, Qiang Zhu, for their support, suggestions and their time. An exceptional mention goes to Juan Lasheras. Juan is always an wisdom elder to me, giving me advice not only for my research, but also for my career and my life.

Next, my gratitude goes to all the amazing people currently in or graduated from our research group for their insights, suggestions, inspirations and being great labmates, friends : Ernesto, Ricardiño, Lorenzo, Josh, Maria, Toni, Yi-Ting, Ashish, Amy, Marissa, Cathleen, Stephanie, Ruedi, Manu, Bego, Effie, Katie.

Thanks to all the other students and post docs in the Biomechanics wing of SME and in the Mechanical and Aerospace Engineering department, present and past, for making the workplace the perfect place to spend my days.

I am truly thankful to my friends I met during these years, who have supported me and always made me feel a bit home: Ang, Fangzhou, Shuning, Bing, Shelly, Fei, Jia.

Finally, but perhaps the most important thanks to my family : my parents Guohua and Xiangrong, my fiancee Dan, and my uncles, aunts and nephews. Thanks for always supporting me and being pround of me all the time.

Chapter 2, in part, is a manuscript in preparation. The title of this manuscript is "The coordination between mechanical and chemical subsystems initiate locomotion of *Physarum* plasmodial fragments". The dissertation author is the primary author of this work.

Chapter 3, in part, has been published in the *Journal of The Royal Society Interface*. Lewis, Owen L ; Zhang, Shun ; Guy, Robert D ; del Álamo, Juan C. 2015. The title of this paper is "Coordination of contractility, adhesion and flow in migrating *Physarum* amoebae".

The dissertation author was the co-first author of this paper.

Chapter 4, in part, has been published in the *Journal of Physics D: Applied Physics*. Zhang, Shun ; Guy, Robert D ; Lasheras, Juan C ; del Álamo, Juan C. 2017. The title of this paper is "Self-organized mechano-chemical dynamics in amoeboid locomotion of *Physarum* fragments". The dissertation author was the primary author of this paper.

Chapter 5, in part, has been submitted. Zhang, Shun ; Skinner, Danielle; Joshi, Prateek ; Lasheras, Juan C ; Caffrey, Conor R ; del Álamo, Juan C. 2018. The title of this paper is "Locomotor adaptability of the schistosome pathogen to changes in its physical environment: mechanical principles and implications for drug discovery". The dissertation author was the primary author of this paper.

VITA

2010	B.S. in Mechanical Engineering, Southwest Jiaotong University (China)
2012	M.S. in Engineering Sciences (Mechanical Engineering), University of California, San Diego
2012 - 2018	Graduate Research Assistant, University of California, San Diego
2012 - 2015	Teaching Assistant, University of California, San Diego
2018	Ph. D. in Engineering Sciences (Mechanical Engineering), University of California, San Diego

PUBLICATIONS

Zhang, Shun, Robert D. Guy, Juan C. Lasheras, and Juan C. del Álamo. "Self-organized mechano-chemical dynamics in amoeboid locomotion of *Physarum* fragments", *Journal of Physics D: Applied Physics* **50**, no. 20 (2017): 204004.

Zhang, Shun, Danielle Skinner, Prateek Joshi, Juan C. Lasheras, Conor R. Caffrey, and Juan C. del Álamo. "Locomotor adaptability of the schistosome pathogen to changes in its physical environment: mechanical principles and implications for drug discovery", *Submitted*

Zhang, Shun, Robert D. Guy, Juan C. Lasheras, and Juan C. del Álamo. "The coordination between mechanical and chemical subsystems initiate locomotion of *Physarum* plasmodial fragments", *In preparation*

Lewis, Owen L., Shun Zhang, Robert D. Guy, Juan C. del Álamo. "Coordination of contractility, adhesion and flow in migrating *Physarum* amoebae", *Journal of The Royal Society Interface* **12**, no. 106 (2015): 20141359.

Álvarez-González, Begoña, Shun Zhang, Manuel Gõmez-González, Ruedi Meili, Richard A. Firtel, Juan C. Lasheras, and Juan C. del Álamo. "Two-Layer Elastographic 3-D Traction Force Microscopy", *Scientific reports* **7** (2017): 39315.

ABSTRACT OF THE DISSERTATION

The mechanics of flow, contractility and adhesion in soft-bodied locomotion

by

Shun Zhang
Doctor of Philosophy in Engineering Sciences (Mechanical Engineering)
University of California San Diego, 2018
Professor Juan Carlos del Álamo, Chair

Soft organisms including unicellular amoebae, slime molds and invertebrates without exoskeleton use similar physical mechanisms to adhere to and crawl over surfaces. Despite the wide range of length scales covered by these organisms (10^{-5} m – 10^{-1} m), and the variety of biological processes involved in the regulation of force generation, all these organisms apply waves of traction (i.e. shear) stresses on their substrate. Given this remarkable evolutionary conservation of the mechanics of soft adhesive locomotion, its study is relevant to a broad number of areas in medicine, ecology and engineering.

Soft adhesive locomotion has been studied theoretically and experimentally for over a century. However, given that most organisms control their size very tightly, the impossibility of decoupling lengthscale dependence from organism dependence has made it difficult to experimentally test theoretical hypotheses. In this work, we focused on the multinucleated slime mold *Physarum polycephalum* because it is possible to prepare motile amoeboid specimens of this organism with sizes spanning two orders of magnitude (10^{-5} m – 10^{-2} m). Given its relatively large size and simple structure, *Physarum* relies on periodic back-and-forth intracellular flows (a.k.a. shuttle streaming) to transport chemical signals such as Ca^{2+}. In turn, these signals regulate the generation of contractile forces that drive intracellular flow and facilitate locomotion.

The main goal of this thesis was to study the dynamics and interplays of these biophysical processes, and their roles in the onset of locomotion and persistent directional migration. To this end, we combined measurements of traction force, fragment morphology, endoplasmic and ectoplasmic velocity, ectoplasmic microrheology properties and endoplasmic Ca^{2+} concentration with experimental manipulations of cell-substrate adhesion, cortical strength and cell size. In parallel, we worked closely with mathematicians to develop a model of a motile fragment which includes forces from the viscous cytosol, a poro-elastic, contractile cytoskeleton and adhesive interactions with the substrate.

Our results suggest that the onset of locomotion is governed by an interfacial instability which is strongly affected by fragment size, cell-substrate adhesion and cortical strength. We also found that most migrating *Physarum* fragments exhibit two types of wave patterns in endoplasmic flow, contractility and chemical signaling. Slow-moving fragments display standing wave patterns similar to amoeboid cells such as leukocytes or Dictyostelium. Fast-moving fragments exhibit traveling wave patterns of traction stress, which are conserved in larger organisms such as annelids or gastropods, and are reminiscent of leg density waves in myriapod locomotion. We show that traveling waves of traction stress provide robust propulsive forces in the presence of heterogeneous friction from the environment, and require tight coordination between contractility and substrate adhesion.

We studied this hypothesis in more detail by investigating the mechanics of locomotion of the flatworm *Schistosoma mansoni* (the most prevalent human endoparasite) under varying levels of confinement, representative of the environments this flatworm encounters in its migratory route from the liver to the intestine. Our results reveal that S. *mansoni* migrates by exerting standing waves of traction stresses with its suckers under no or gentle confinement, but transitions to exerting traveling waves of traction stress along its body when crawling through in highly restrictive conditions.

Chapter 1

Introduction

Adhesive locomotion of soft-bodied organisms is achieved by applying propulsions on their environment through traction stress waves [1]. It covers a wide range of species and legnthscales, plays an important role in many processes and affect everyone's life. For example, amoeboid cell migration is soft adhesive locomotion and plays an important role in many physilogically relevent processes including cancer metastasis, the function of immune system, morphogenesis and wound healing. [2–5]. Many of human parasites also share similar mechanism of locomotion, and a better understanding of the mechanics will provide insights on treating the parasite [6–8]. The locomotion of gastropods, most worms and slime molds are also soft adhesive locomotion, and they are crucial in ecology for breaking down organic matters [9–11]. A more comprehensive understanding of the mechanism will also facilitates the design of new generation biomimetic soft robot [12].

In spite of the diverse species and lengthscales, the mechanics of propulsion is very conserved for soft adhesive locomotion : organisms all generate periodic traction stress waves as thrust to migrate. For example, single cellular systems like *Dictyostelium* generate clear standing wave patterns of traction stress to migrate on flat surface [13, 14], while slime, flat worms, gastropods all organized their traction stress in the form of traveling waves [10, 11]. Despite the vast existing knowledge about the biochemical processes involved, our understanding of the underlying mechanical processes behind these traction stress waves is still rather phenomenological. Furthermore, micro and macro-scaled soft-bodied organisms are always treated as separated research regimes. The link and transition in the mechanisms of locomotion between micro and macro sized organisms are barely touched.

This work mainly focuses on the model organism *Physarum* polycephalum, which is

a multinucleated slime mold that forms fast moving amoebae. During locomotion, the cytoplasm flows periodically forward and backward [15], which is driven by a periodic contraction of the cortex. The cortical contractions are regulated by calcium ions [16, 17], whose propagation is in turn governed by the flow. These well-defined mechanochemical subsystems make it an ideal model to study their coordination in locomotion. Furthermore, unlike other cell types with a well defined size, we can easily vary the size of *Physarum* microamoebae in the range from 50 μmto 1 mm. This allows us to study the fundamental flow physics involved in amoeboid cell migration in a wide range of regimes, thus bridging the gap of migration between micro and macro sized soft organisms.

Recently there has been an intense effort devoted to the fundamental study of active fluids try to understand the complex dynamics and mechanics of cells [18, 19]. Despite this foundational theoretical development, a gap remains between these theories and the actual cellular systems. Particularly, cell-substrate interactions, large-scale cytoskeletal remodeling and cell shape changes have been largely neglected. In this work, we simultaneously quantified the traction stresses exerted on the substrate, the cytoplasmic velocity field, morphology, and the transport of the intracellular calcium ions that regulate cellular contraction. The resulting experimental characterization are unprecedented both in terms of completeness and level of detail. We will perform measurements and develop models in tandem, with our model development motivated by experimental observations, and our model predictions tested by additional experiments. Numerical simulations give us the ability to explore hypotheses based on our experimental observations, to push the boundaries of parameters without undesired downstream effects, and to examine quantities that are not easily measured in experiments. Together our models and experiments will give a more comprehensive and integrative view of the flow physics and design principles underlying soft-adhesive locomotion.

In Chapter 2, we have combined traction force and morphology measurements with experimental manipulations of cell-substrate adhesion, cortical strength and cell size of *Physarum* fragments to understand the contribution of these mechanical factors to symmetry breaking and motility initiation in flow driven amoeboid cell. Our experimental evidence suggests a close dependence of probability of motility initiation with size and morphology. Furthermore, this relation is strongly affected by cell-substrate adhesion and cortical strength.

In Chapter 3, we have examined the relationship between spatio-temporal coordi-

nation of intracellular flow and traction stress and the speed of amoeboid locomotion of microplasmodia of *Physarum polycephalum*.We simultaneously perform particle image velocimetry and traction stress microscopy to measure the velocity of cytoplasmic flow and the stresses applied to the substrate by migrating *Physarum* microamoebae. In parallel, we develop a mathematical model of a motile cell which includes forces from the viscous cytosol, a poro-elastic, contractile cytoskeleton and adhesive interactions with the substrate. Our experiments show that flow and traction stress exhibit back-to-front-directed waves with a distinct phase difference. The model demonstrates that the direction and speed of locomotion are determined by this coordination between contraction, flow and adhesion. Using the model, we identify forms of coordination that generate model predictions consistent with experiments. We demonstrate that this coordination produces near optimal migration speed and is insensitive to heterogeneity in substrate adhesiveness.

In Chapter 4, we measure the spatio-temporal distributions of the velocities of the endoplasm and ectoplasm of migrating *Physarum* fragments, the traction stresses it generates on the substratum, and the concentration of free intracellular calcium. Using these unprecedented experimental data, we classify migrating *Physarum* fragments according to their dynamics, finding that they often exhibit spontaneously coordinated wave patterns of flow, contractility and chemical signaling. We show that *Physarum* fragments exhibiting symmetric spatio-temporal patterns of these quantities migrate significantly slower than fragments with asymmetric patterns. In addition, our joint measurements of ectoplasm velocity and traction stress at the substratum suggest that forward motion of the ectoplasm is enabled by a succession of stick-slip transitions, which we conjecture are also organized in the form of waves. Combining our experiments with a simplified convection-diffusion model, we show that the convective transport of calcium ions may be key for establishing and maintaining the spatio-temporal patterns of calcium concentration that regulate the generation of contractile forces.

In Chapter 5, we explored the mechanics of locomotion of the schistosome pathogen under physiologically relevant conditions using self-designed experimental setups and devices. We revealed, for the first time, that S. *mansoni* change the locomotion mechanisms when facing different physiologically relevant mechanical challenges. S. *mansoni* exclusively use their oral and ventral suckers generating forces to migrate in the environment without confinement around their body. When subjecting to flow of varying magnitude, S. *mansoni* actively adjust their grabbing strength via their suckers to remain attached to the substrate.

However, S. *mansoni* switched to a completely different locomotion strategy when crawling through restrictive conditions by applying traveling waves of strong traction stress along the body. Strikingly, we discovered the sucker action and body contraction wave can be coordinated to achieve faster locomotion when migrating under restrictive environment.

Chapter 2

The coordination between mechanical and chemical subsystems initiate locomotion of *Physarum* plasmodial fragments

2.1 Introduction

Amoeboid motility is defined by large shape changes associated with locomotion [2, 3, 20]. Flow-driven amoeboid motility is an interesting paradigm because this motility mode is fast and robust to changes in the extracellular environment without creating specific chemical bonds with the substrate, which involves the interplay between intracellular flow, chemical signaling, cellular contraction, cell-substrate adhesion etc [11, 15, 21]. Many experimental and computational works are focused on revealing the mechanism of mechanochemical oscillations that lead to persistent locomotion in flow driven amoeboid cell [11, 21]. This has also spurred the exploratory design of bio-inspired amoeboid robots at millimetric scales made of active self-oscillating hydrogels [22].

Although the biochemical and mechanical mechanisms that control steady-state migration in flow driven amoeboid cells have been well characterized, the mechanism of spontaneous symmetry breaking and motility initiation, which require nonlinear amplification of stochastic fluctuations in chemical or mechanical signals [23], are still poorly understood. Especially, the effect of mechanical properties of the cell, cell-substrate adhesion and mor-

phological changes on motility initiation haven't been quantified.

Recently, several papers examined instabilities using a generic poroelastic two-phase model in a system with active stresses arising from a chemical transported through the cytosol [24–26], which revealed different forms of mechanochemical waves including traveling, standing, and rotating waves by employing linear stability analysis and numerical simulations. Despite these foundational theoretical development, these models have been so far limited to fixed simple geometries or have neglected key aspects of the mechanochemical feedback such as cell-substrate interactions, large-scale cytoskeletal remodeling and cell shape changes. Erin *et al.* have shown the balance between cell-substrate adhesion and myosin contraction determines the frequency of motility initiation in fish keratocytes [27]. However, this is not directly applicable to flow-driven amoeboid cell that rely on pressure-driven cytoplasmic flows for migration without creating specific binding sites on the substrate.

The plasmodium *Physarum* polycephalum, a true slime mold, has been widely used as a model organism in studies of flow-driven amoeboid locomotion. The plasmodium is a single cell with multiple nuclei and is composed of a gel like outer ectoplasmic layer and a sol-like inner endoplasm. The endoplasm exhibits streaming movements induced by the periodic contraction of the ectoplasm, which is in turn governed by the transportation of calcium ions of the flow [11]. The size of the plasmodia can be easily controlled by the way it prepared. Experiments with small plasmodia of sizes ranging from tens to a few hundred microns provide the possibility to study internal amoeboid dynamics and motility initiation of *Physarum* without the pronounced vein structures usually present in *Physarum* fragments of larger size.

In this work, we have combined traction force and morphology measurements with experimental manipulations of cell-substrate adhesion, cortical strength and cell size of *Physarum* fragments to understand the contribution of these mechanical factors to symmetry breaking and motility initiation in flow driven amoeboid cell. Our experimental evidence suggests a close dependence of probability of motility initiation with size and morphology. Furthermore, this relation is strongly affected by cell-substrate adhesion and cortical strength.

2.2 Methods

2.2.1 Preparation of *Physarum* fragments

Physarum polycephalum plasmodia were cultured on 1% agar plate with oat flakes. Small portions were cut from the parent plasmodia and transferred plain agar plate and kept in a dark humid environment at room temperature for 10 hours. We subsequently excised multiple tens to hundreds micron sized pieces from the marching end with a scalpel and placed them over collagen coated polyacrylamide (PA) gels embedded with fluorescent beads. A cap made of 1% agar of 1 mm thickness was then placed over the *Physarum* fragments. The samples were put under microscope to acquire image sequences immediately after.

2.2.2 Gel fabrication

Collagen-coated PA gels of 1.5 mm thickness were prepared for traction force microscopy as previously described [28]. The gels contained a thin top layer (10 μm) containing 1 μm fluorescent beads (FluoSperes; molecular probes) that were used as fiduciary markers to track substrate deformation. Gels were fabricated using 5% acrylamide and 0.3% bisacrylamide (Fisher BioReagents), resulting in a Young's modulus of 8.73 kPa. The Poisson's ratio of the gel was measured to be 0.46, following an elastographic traction force microscopy method developed by our group [29]. PA gels were activated with sulfo-SANPAH (Thermal Scientific) under UV light and coated with 0.15 mg/ml collagen I (Corning).

2.2.3 Microscopy

A Leica DMI 6000B inverted microscope controlled by a PC running Micro-Manager software was used for image acquisition [30]. An automated stage (ASI) was utilized to highly improve the throughput. Two acquisition protocols were followed for different experiments reported in this work. The bright field only image sequences were acquired under 10X with 30 seconds time interval for 8 hours. For experiments used to quantify the traction stress, both bright and fluorescent field images were acquired with time interval of 5 minutes for 8 hours. The fluorescent filed was constructed by a 40-image fluorescence z-stack ($\Delta z = 1$ μm) for 3D traction force microscopy.

2.2.4 Traction force microscopy

The 3D deformation of the top surface of PA substrate induced by *Physarum* fragments were measured by tracking the motion of the fluorescent beads. Each instantaneous fluorescence z-stack was cross-correlated with a reference z-stack which was recorded at the end of experiment once the amoebae moved out of the field of view. Using these measurements as boundary conditions, we solved the equation of mechanical equilibrium for the PA gel as previously described [28, 31]. Using this solution, we computed the deformation field in the whole polyacrylamide substrate, as well as the traction stress vector $\boldsymbol{\tau} = (\tau_{xz}, \tau_{yz})$ on its top surface. The spatial resolution was 6.5 μm and 10 μm under 16X and 10X, and 1 μm in z.

2.2.5 Pharmacological treatment

Phalloidin and Latrunculin A have been reported that can be used to significantly increase the thickness of cortical layer [32] or to disrupt the cortex of *Physarum* fragments [33], respectively. To test the effect stronger cortical tension on motility initiation, 1 mM Phalloidin (Sigma) was injected into the parent mold under a Nikon SMZ-10 microscope using a PM 1000 cell micro-injection system (MicroData Instrument, Inc). The injected amount(100 nl) is less than 1% of the volume of parent mold, which was calculated by the measured diameter of the tubular structure of parent mold. After waiting for 2 hours, we excised multiple micro amoebae from the marching end and placed them over collagen coated PA gels as described before. To generate *Physarum* fragments with weaker cortex, the micro amoebae generated as described in Section 2.2.1 were transferred to 5 μM Latrunculin A (Cayman) solution for 10 minutes, and then washed by MQ water before seeded on PA gel.

2.2.6 Adjust the substrate adhesion

To decrease or increase the substrate adhesion, agar cap and PA gel were immersed in 0.2% Pluronic F-127 (Sigma) or 2.5 mg/ml Poly-L-Lysine solution for 1 hour, respectively. Followed by washing thoroughly with MQ water 3 times before seeding the *Physarum* fragments.

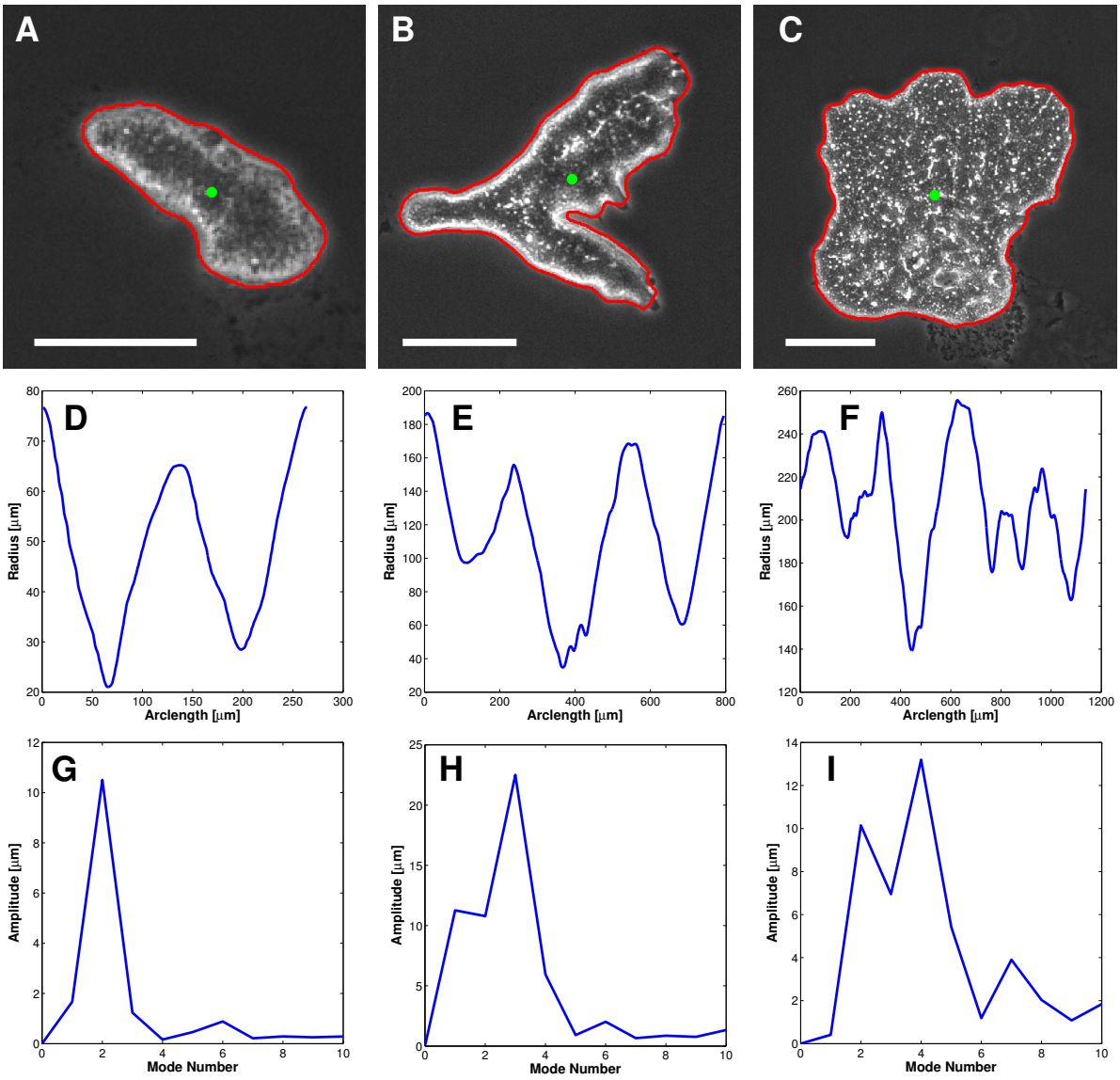

Figure 2.1: Shape analysis. (**A**,**B**,**C**) Snapshots of bright field images with different dominant surface modes. Red curve is detected boundary, green dot is centroid. (**D**,**E**,**F**) The radial distance from the centroid to points on detected boundary in (**A**,**B**,**C**) are plotted as a function of arclength of the boundary. (**G**,**H**,**I**) Amplitude of the mode number n which is derived from the Fourier transform of (**D**,**E**,**F**), with dominant surface mode number 2,3,4, respectively.

2.2.7 Shape analysis

The shape analysis is illustrated in Figure 2.1. First, the boundary and centroid of the fragments at each frame was detected by our customized code (Figure 2.1A,B,C). Then the distance between the centroid and the boundary points were measured as a function of the arclength along detected boundary (Figure 2.1D,E,F), and thus defined as R(s). A

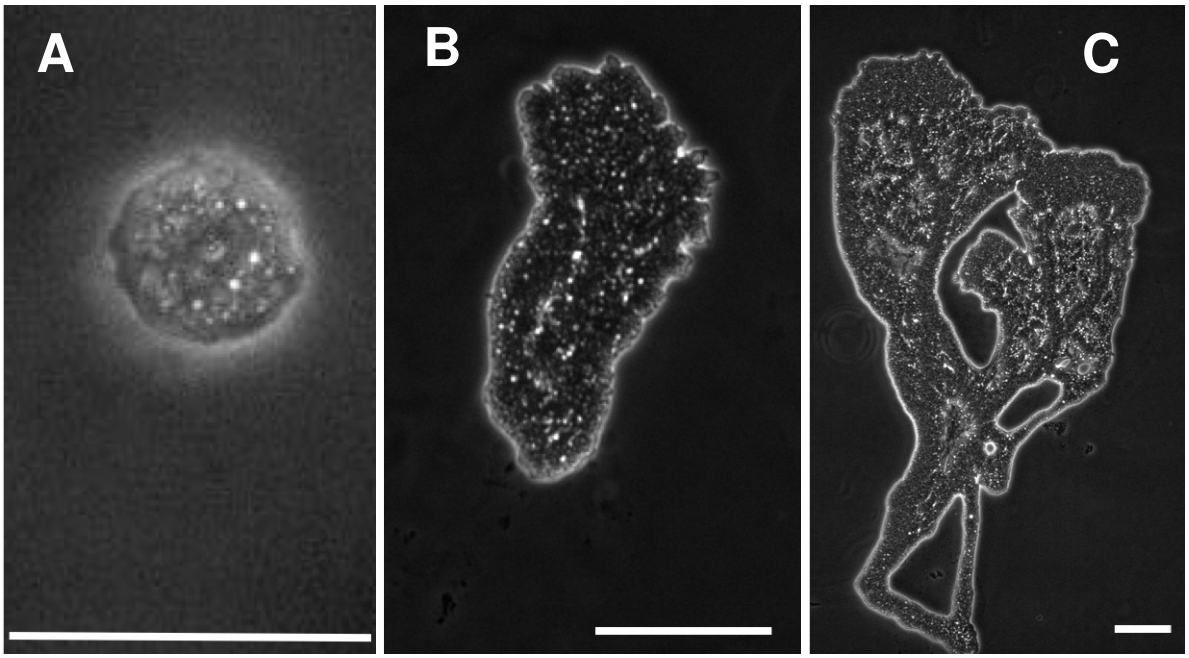

Figure 2.2: Typical morphology of *Physarum* fragments with different size. (**A**) Small fragments (R $<$ 30 μm) are mostly rounded. (**B**) Fragments with 100 μm characteristic radius develop tadpole like shape. (**C**) Larger fragments (R $>$ 1mm) develop complex branched structure.

Fourier analysis of R(s) resulted in a spectrum from which the amplitude of the surface wave mode numbers was determined (Figure 2.1G,H,I).

2.3 Results

Unlike other cell types which have a well defined size, the size of *Physarum* fragments can be varied across a few orders of magnitudes by how the samples were prepared. They exhibit distinct morphologies with different length scale. For fragments with characteristic radius R $<$ 40 μm, most of them are rounded and not able to initiate persistent locomotion (Figure 2.2A). Larger fragments which are bigger than a few hundred of microns generally adapt to a complex morphology with a sheet-like frontal part and well developed tubular veins at the rear (Figure 2.2C). In this work, we focused on the fragments with characteristic radius less than 200 μm. Under which the *Physarum* fragments are not large enough to develop tubular network with voids within the detected boundary.

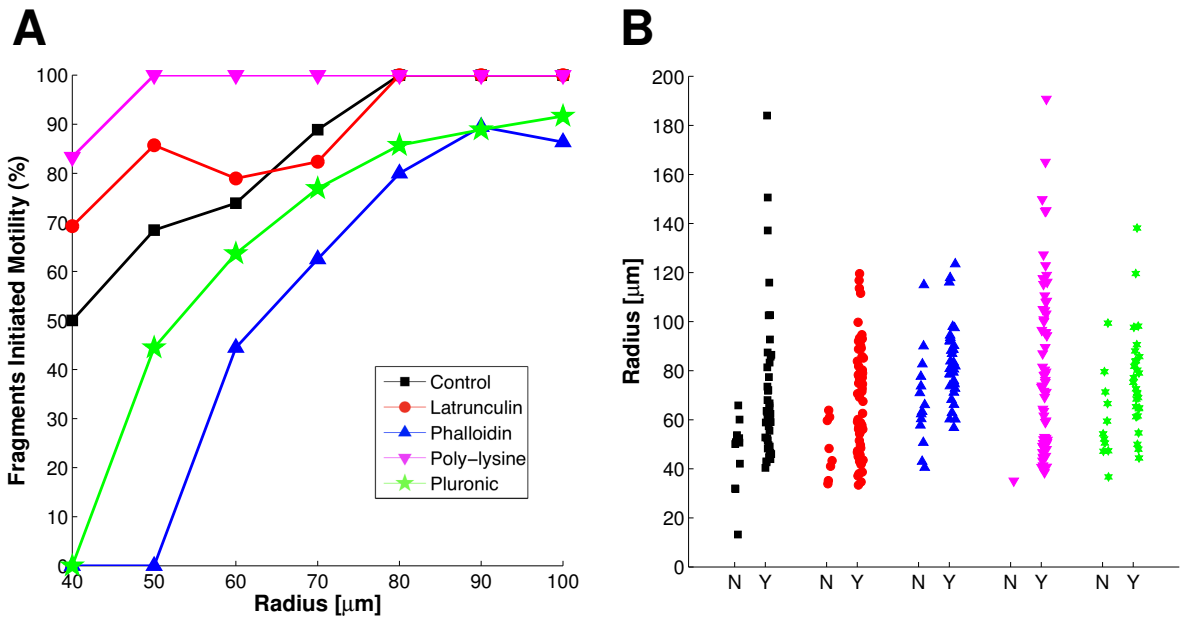

Figure 2.3: Size, cortical strength and substrate adhesion determines the frequency of motility initiation. (**A**) Percentage of fragments initiated motility as a function of size. Data is binned with 10 μmin size. Black-control, red-weaker cortex, blue-stronger cortex, magenta-increase adhesion, green-decrease adhesion. (**B**) The raw data used to generate (**A**). Y-fragments initiated motility, N-fragments not initiated motility. Colors are consistent with (**A**).

2.3.1 The frequency of motility initiation depends on fragment size and is affected by substrate adhesion and cortical strength

After seeding samples of various size on substrate, it seems that larger fragments are more likely to initiate persistent locomotion than smaller ones. This phenomenon is quantitatively characterized in Figure 2.3, where a monotonic direct relationship between the percentage of fragments initiated locomotion and their size has been revealed. All fragments with a characteristic radius larger than 80 μmin control group initiated locomotion.

Although cell-substrate adhesion is directly involved in the process of motility initiation, it has been neglected for many computational works and its role is still not well understood. We next investigated the effect of adhesion strength on motility initiation by performing experiments on Pluronic or Poly-L-Lysine treated substrate, which decrease or increase substrate adhesion, respectively. We found fragments of similar size are more likely to initiate locomotion on more adhesive substrate, which is a clear evidence that increased adhesion strength facilitates motility initiation. This hypothesis is further validated by the

opposite effect we found that the frequency of motility initiation decreased as adhesion strength decreased.

Cortical tension is another mechanical factor that could strongly affect the motility initiation process. *Physarum* has been reported with strong and thick cortical layer which is crucial for maintaining its shape. The effect of cortical tension in flow driven amoeboid motility should be similar with surface tension in well studied hydrodynamic instability problems, which stabilizes the system. We investigated the role of cortical strength by pharmacological treatment with Phalloidin or Latrunculin A, which strength or weaken the cortex, respectively. As expected, we found stronger cortex suppress the motility initiation while weaker cortex facilitate this process (Figure 2.3).

2.3.2 Shape oscillations are governed by a dominant mode and are affected by substrate adhesion and cortical strength

During the experiment, fragments were continuously shifting their shapes. The shape at each frame can be extracted as surface modes (Figure 2.1). After normalizing with fragment size and averaging over time, we find 281 out of 287 fragments exhibit a dominant mode of mode 2 (except for mode 0 which stands for a circle), and the other 6 pieces show a dominant mode 3 (2.4A). However, for the pieces with dominant surface mode 3, we didn't find any distinctions on size, whether or not initiated motility, migration velocity, magnitude of traction stress etc. Since the shape oscillations of *Physarum* fragments are dominated by surface mode 2, we only focused on mode 0 and 2 for our shape analysis in this study. Essentially, mode 0 stands for a circle with the same size as the fragment, thus is related to the roundness of the fragment. While mode 2, on the other hand, stands for how elongated the fragment is.

Depending on the locomotion speed, the temporal evolution can be clearly divided into stationary and persistent motion phase. Interestingly, the average amplitude of mode 0 are not significantly different for these two phases (Figure 2.4B), which differs from the traditional view that the shape in the stationary phase should be more rounded while be more elongated at the persistent motion phase. We then plot the average amplitude of mode 0 and 2 of the whole time sequence as a function of fragment size, and find that larger fragments are more elongated (Figure 2.5).

Since the frequency of motility initiation is strongly affected by adhesion strength and

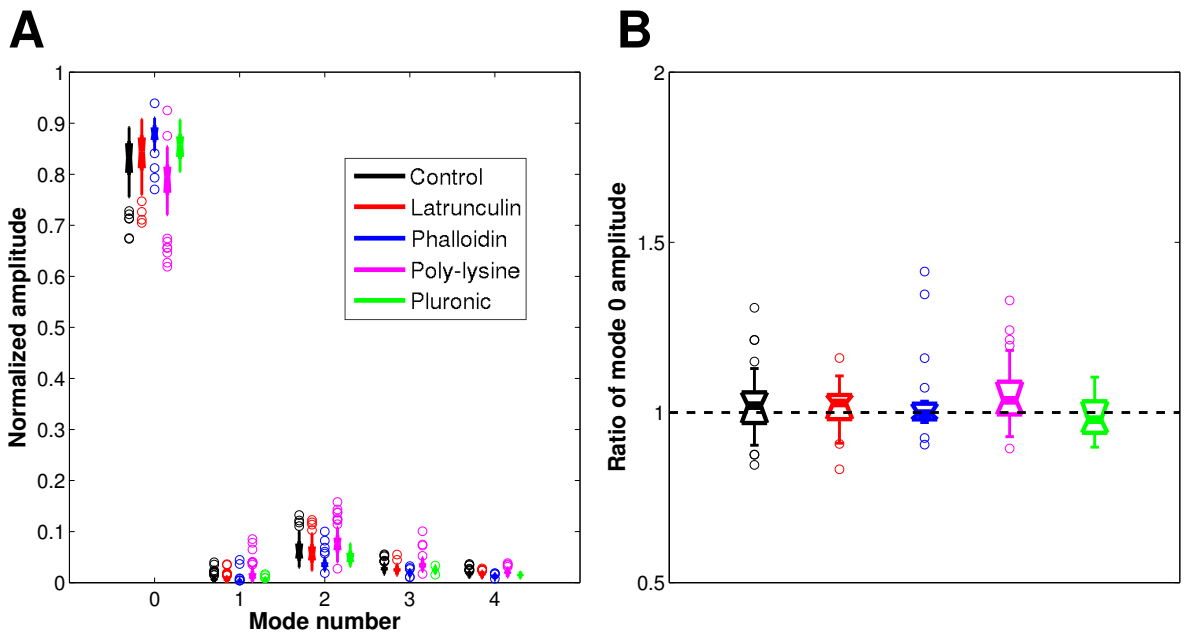

Figure 2.4: (**A**) Box plot of the normalized amplitude of first 5 surface modes. Black-control, red-weaker cortex, blue-stronger cortex, magenta-increase adhesion, green-decrease adhesion. (**B**) Ratio of amplitude of mode 0 between stationary phase and persistent locomotion phase. Colors are consistent with (**A**).

cortical tension, we hypothesized varying these quantities will also affect the morphologies of the fragments. We found fragments of similar size are more rounded on less adhesive substrate and are more elongated if being placed on more adhesive substrate. Callan-Jones *et al.* [34] performed a flow instability analysis and proved that lower modes are less stable as a function of increasing friction, which is consistent with our findings. As we mentioned in previous section, cortical tension plays an important role for stabilizing the system. We found fragments of similar contact area are more rounded with stronger cortex, as expected. However, we didn't find a clear opposite trend for fragments with weaker cortex. Possibly due to some cascade effects from treating with Latrunculin A.

Our findings reveled a clear dependence of percentage of motility initiation and morphology on fragment size, thus it is not surprised that the percentage of motility initiation and morphology are also closely related (Figure 2.6). Strikingly, we didn't find a significant difference between the morphologies of fragments that are not able to initiate motility under various conditions (supplementary material). This essentially means no matter what method is used to vary the shape, the dependence of frequency of motility initiation on the morphology is similar.

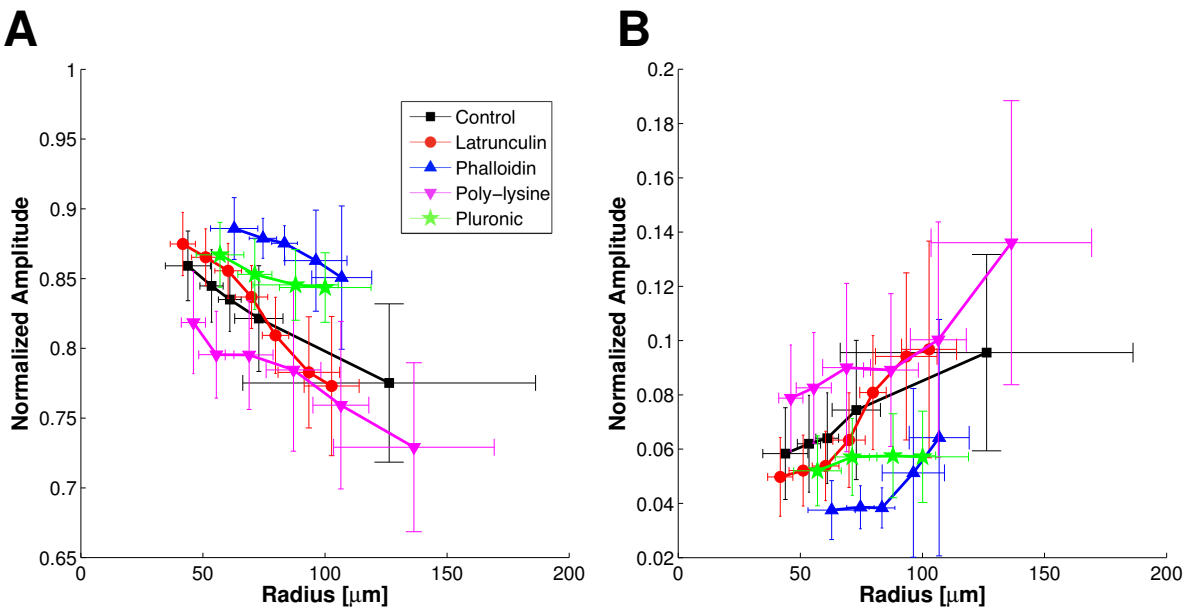

Figure 2.5: Size, cortical strength and substrate adhesion determines the morphology of fragments. (**A**) Normalized amplitude of surface mode 0 as a function of size. Black-control, red-weaker cortex, blue-stronger cortex, magenta-increase adhesion, green-decrease adhesion. (**B**) Normalized amplitude of surface mode 2 as a function of size. Colors are consistent with (**A**).

2.3.3 Traction stress correlates with the contract area, and is affected by varying cortical strength and substrate adhesion

To understand the effect of varying cortical strength and substrate adhesion to the underlying mechanochemical oscillations, we measured the traction stress they exerted on the substrate from the beginning until they achieve persistent locomotion and migrate out of the acquisition window. In our experiments, *Physarum* fragments showing an inward contractile pattern with larger stresses along the cell periphery all the time (Figure 2.7A). This pattern has been proposed to be analogous to a surface tension, and has been recently linked to the cortical F-actin filaments and their cross-linkers in Dictyostelium amoebae [13]. In the same time, they exert a downward stress in the vertical direction within the cell periphery (Figure 2.7B). We found in-plane traction stress is in counterphase with the oscillations of contract area, which is in agreement with previous findings (Figure 2.7G). But for the first time, we revealed that the vertical traction stress is in phase with the horizontal one. (Figure 2.7H) When the *Physarum* fragment contracts with minimum contract area, both horizontal and vertical stresses increase and when the amoeba relaxes with maximum area, both traction

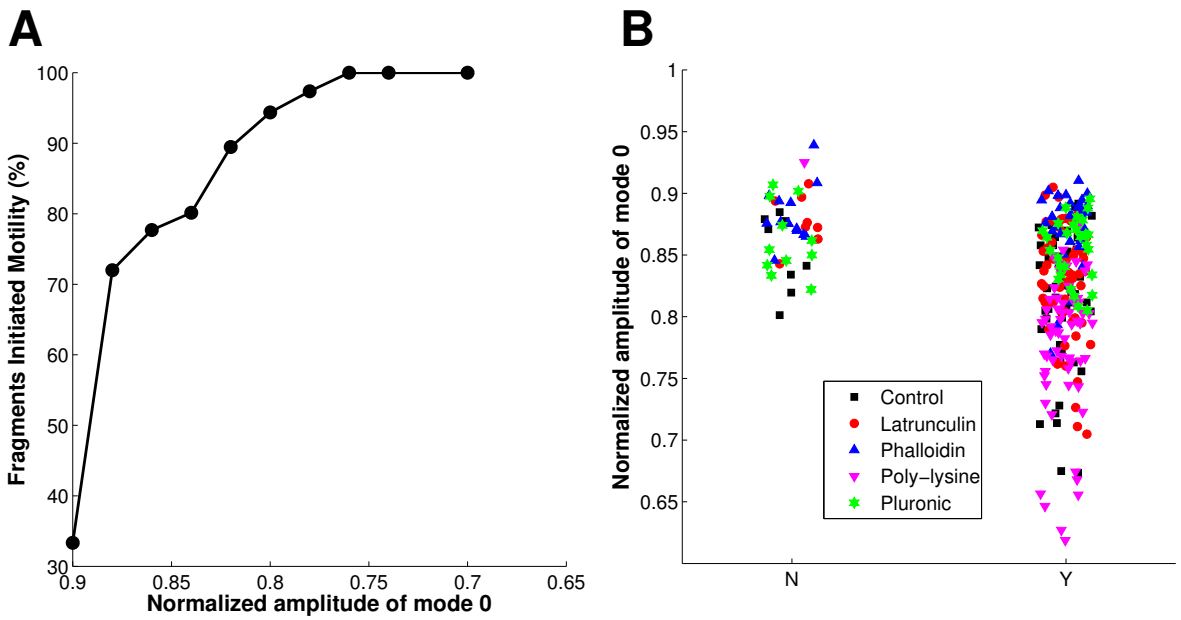

Figure 2.6: Morphology determines the frequency of motility initiation. (**A**) Percentage of fragments initiated motility as a function of normalized amplitude of surface mode 0. Data is binned with 0.03 in amplitude. (**B**) The raw data used to generate (**A**). Y-fragments initiated motility, N-fragments not initiated motility. Black-control, red-weaker cortex, blue-stronger cortex, magenta-increase adhesion, green-decrease adhesion.

stresses decrease (Figure 2.7C,D).

For all the experiments we analyzed, strong normal compressive forces appeared near the cell center (Figure 7 2.7B). This compressive force is positively related with the intracellular pressure of the fragment, which directly related with the cortical tension. Even though an accurate measurement of cortical tension is not applicable for this study, the compressive forces can still be used as an indicator for cortical strength. As expected, we found fragments with weaker cortex exerted significantly smaller magnitude of both horizontal and vertical traction stresses, while the ones with stronger cortex exerted larger stress (Figure 2.7J). These findings also validate the pharmacological treatment we used for modifying cortical strength in this study.

The effect of varying substrate adhesion on the traction stress has also been quantified. When being placed on more adhesive substrate, the fragments exert much larger (significantly different) in-plane traction stress while seems to be a smaller (not significantly different) out-of-plane traction stress (Figure 2.7I,J). The correlation between horizontal and vertical stresses are also weaker (Figure 2.7G,H). As for the experiments performed on low adhesive substrates, fragments exerted a smaller traction stress in horizontal direction (significantly

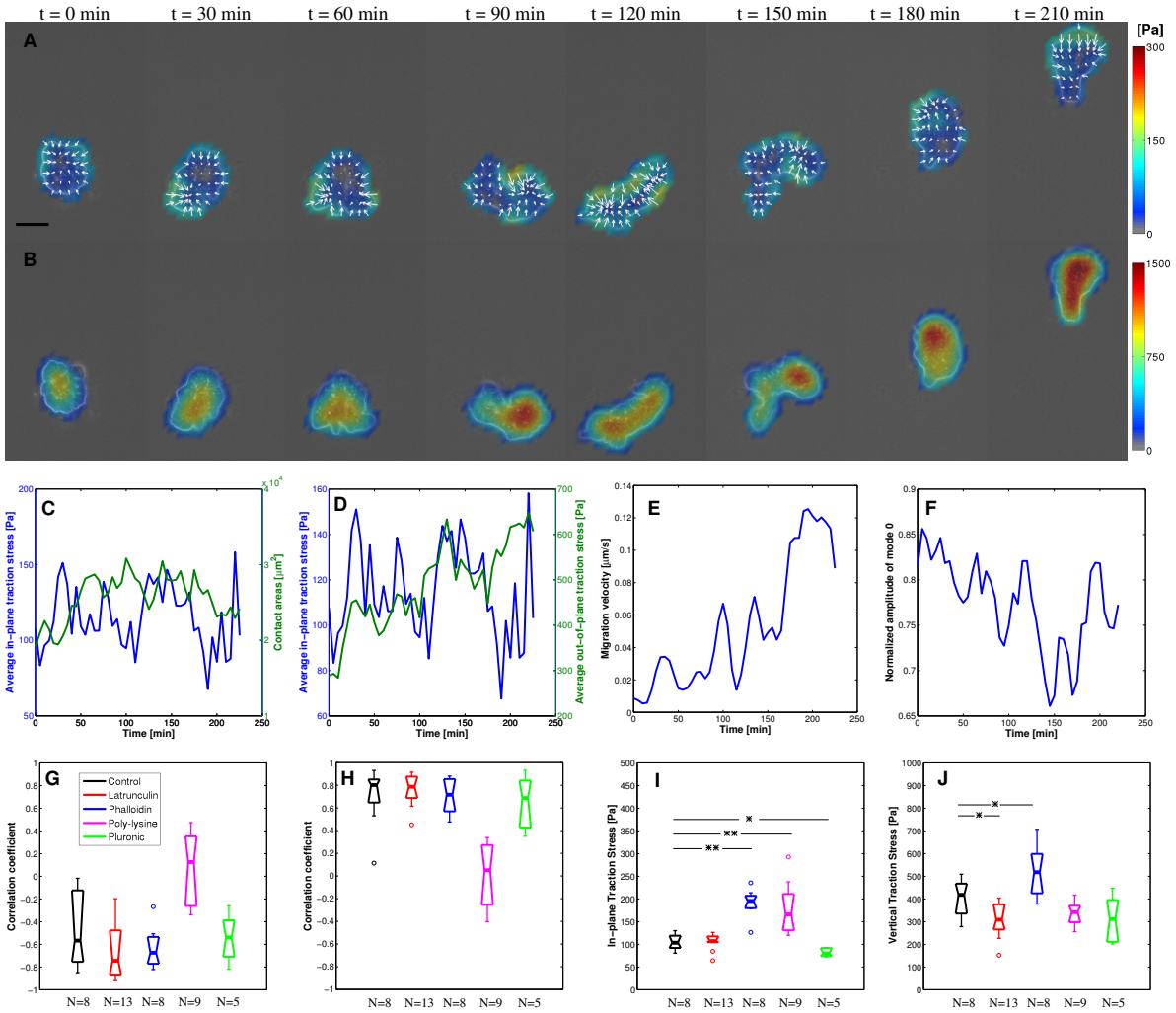

Figure 2.7: (**A**) Instantaneous in-plane traction stress exerted on the substrate by a *Physarum* fragment during locomotion initiation. (**B**) Instantaneous out-of-plane traction stress exerted on the substrate by a *Physarum* fragment during locomotion initiation. (**C**)Time evolution of average in-plane traction stress (blue) and contract area (green). (**D**)Time evolution of average in-plane traction stress (blue) and out-of-plane traction stress (green). (**E**) Time evolution migration velocity. (**F**) Time evolution of normalized amplitude of mode 0. (**G**) Spearman correlation coefficient for temporal evolution of in-plane traction stress and contract area. Black-control, red-weaker cortex, blue-stronger cortex, magenta-increase adhesion, green-decrease adhesion. (**H**) Spearman correlation coefficient for temporal evolution of in-plane traction stress and out-of-plane traction stress. (**I**) Average magnitude of the in-plane traction stress. (**J**) Average magnitude of the out-of-plane traction stress. The number of fragments (N) are indicated beneath the box plot. (Asterisks) Statistically significant differences between each specific group and its corresponding control distribution (Wilcoxon ranksum test, $*$ $p < 0.05$, $**$ $p < 0.01$).

different). The vertical traction stress also looks smaller compare with the control group, but it is not significantly different.

2.4 Discussion

This study has revealed a close relation of adhesion strength, morphology and cortical strength with symmetry breaking and motility initiation process of flow driven amoeboid cell, which were often neglected in the theoretical and computational models. The experimental data presented in this work will motivate related theoretical work to include these parameters to the theory development aiming at understanding the complex dynamics of mechanochemical systems of the cell. Furthermore, these experimental measurements provide detailed quantitative data of how these mechanical factors working together in live cells, thus can be used as important validations for model development.

The contact area has been used throughout the manuscript to indicate the size of *Physarum* fragments. It is a rather crude approximation since the fragments underwent very dynamic oscillations in contract area and thickness. However, the experimental setup of agar cap provides a gentle confinement on the thickness variation of the fragments thus prevent drastic changes in contract area. Furthermore, the results in this work are still valid even if we take the errors caused by approximating size using contract area into consideration. For example, the group of fragments with stronger cortex are thicker because they exerted significantly stronger compressive normal forces on the substrate. This essentially means that with the same contact area, the ones treated with Phalloidin are larger in size, which will shift the curve stands for the group of stronger cortex to the right along x axis in Figure 2.3. After applying this argument to all the groups with variations in substrate adhesion and cortical strength, we find our conclusions are still valid.

2.5 Acknowledgements

Chapter 2, in part, is a manuscript in preparation. The title of this manuscript is "The coordination between mechanical and chemical subsystems initiate locomotion of *Physarum* plasmodial fragments". The dissertation author is the primary author of this work.

Chapter 3

Coordination of contractility, adhesion and flow in migrating *Physarum* amoebae

3.1 Introduction

Cell migration plays a critical role in a wide variety of biological processes, including morphogenesis, wound healing and the immune response. Amoeboid motility is a fast type of cell migration defined by large shape changes as the cell extends and retracts various pseudopodia and blebs [35]. These extensions are driven by the interplay between substrate adhesion, the polymerization of filamentous actin and the pressure driven flow of cytoplasm [2]. Research on amoeboid motility has recently intensified in part because this migration mode is robust to changes in the extracellular matrix and the specific molecular nature of the cell-matrix adhesions [3, 4]. That is to say, amoeboid cells are able to cross barriers, move through confined channels, or squeeze through 3-D matrices by contracting and pushing-off the surrounding environment. This versatility has also spurred the exploratory design of bio-inspired millimetric robots made of active self-oscillating hydrogels [22]. Despite the vast existing knowledge about the biological and molecular processes involved in cell migration, our understanding of the underlying mechanical processes is still rather phenomenological. In particular, the coordination of contractility, adhesion and flow of cytoplasmic material that enables pseudopod extension is not fully understood. In fact, it is not even clear if coordination of these processes is necessary for motility in all scenarios [3].

This work investigates the coordination of cellular contractile force, substrate adhesion and cytoplasmic flow in migrating amoebae of the slime mold *Physarum polycephalum*. *Physarum* plasmodia generate a periodic flow of cytoplasm (known as shuttle streaming) through a tubular network. This flow is driven by pressure gradients created by contraction of the actomyosin network within the plasmodium [36–38]. Small-scale *Physarum* amoeabe ($\sim 100\,\mu$m in length) can exhibit a similar behavior where a rhythmic flow of cytoplasm moves back and forth along the centerline of a roughly tadpole shaped cell. The onset of this behavior has been observed to coincide with a drastic increase in the locomotion speed of growing *physarum* [39]. Larger scale plasmodia ($l \sim 500\mu m$) can develop more complex morphologies including chains of round contractile heads connected by relatively inert tubes, as shown by Rieu et al in a companion paper [40].

Due to the relatively large scale of the organism, Particle Image Velocimetry (PIV, [41]) experiments allow researchers to measure the intracellular fluid velocity in *Physarum* amoebae using cell organelles as flow tracers. The periodic waves of cytoplasmic streaming in tadpole shaped cells have been well characterized by PIV and it has been argued that the traveling-wave nature of the intracellular flow is responsible for generating directed motility [15]. However, a purely hydrodynamic explanation of *Physarum* amoeboid motility does not address the transmission of traction stress to the underlying substrate, which is ultimately necessary for cellular migration to take place. It is unclear if passive, uncoordinated cell-substrate interactions are sufficient for *Physarum* plasmodia to effectively "flow" across a substrate. Alternately, the motility of *Physarum* plasmodium might depend upon cell-substrate adhesion being dynamically coordinated relative to the stresses generated by the flow. It is known that substrate bound structures are mechanically linked the to actomysosin network within the plasmodium [42]. However, the precise nature of these structures is not well studied, and there currently exists no quantitative description of the stresses which the cell exerts on the substrate as it migrates, nor how these stresses are correlated to the cytoplasmic flow.

To answer these questions, we concurrently perform Traction Force Microscopy (TFM) and PIV measurements on migrating *Physarum* amoebae. In the past, TFM has been used to study the adhesive forces that enact locomotion of a diverse array of unicellular and multicellular organisms ranging from a few microns to a few centimeters in size [9, 31, 43, 44]. In conjunction with these experiments, we develop a computational model for migrating *Physarum* amoebae based on a modified Immersed Boundary (IB) [45]. The model ac-

counts for hydrodynamic effects, elastic forces within the cell interior, and adhesive coupling of the cytoskeleton to the substrate. We use the model to examine how cytoskeletal contraction, cyotosolic flow, and cell-substrate adhesion work together to generate cell locomotion.

Our measurements show that traction stresses in migrating *Physarum* amoebae are mainly distributed along the cell periphery forming an inward contractile pattern. These stresses are spatiotemporally modulated to establish a rythmic contraction wave that travels in the direction of cell migration. The contractile wave has the same time period as the intracellular flow waves previously described, and a phase lag of approximately $1/3$ of a cycle. These spatiotemporal flow and stress patterns are reproduced by the numerical simulations using an idealized model of adhesion. We apply this adhesion model to investigate the strength of adhesion and its coordination *relative* to the rhythmic flow of cytoplasm. Specific coordination patterns are identified which are consistent with experimental data. These parameters are seen to be optimal in that they (nearly) maximize migration velocity of the model cell for a given strength of actomyosin contraction. Finally, we perform numerical simulations of the model cell crawling across randomly heterogeneous substrates and show that the speed of migration is only mildly perturbed. These simulations imply that the proposed model of motility is robust to perturbations of adhesiveness of the extracellular substrate.

3.2 Experimental Materials and Methods

This section summarizes the cell culture, microscopy and analysis methods employed to prepare migrating *Physarum* microamoebae, and to jointly measure the intracellular flows and traction forces generated by these amoeabe while migrating. A more exhaustive description of these methods can be found in the Supplementary Information. *Physarum* plasmodia were obtained from a generous gift by Toshiyuki Nakagaki (Research Institute for Electronic Science, Hokkaido University) and cultured as previously described [15]. Small portions of area $\sim 0.2 \times 0.2\ mm^2$ were cut from the parent plasmodia to produce migrating amoebae, which were transfered to collagen-coated polyacrylamide (PA) gels embedded with fluorescent beads. The PA gels were prepared as previously described [28]. We kept the PA gel humidified throughout the experiment and flattened the amoebae to facilitate intracellular flow visualization by placing an agarose cap on top of the PA gel containing the specimen.

Using an inverted microscope, we simultaneously acquired transmitted-light and fluo-

rescence z-stack image sequences of the migrating *Physarum* amoebae with time resolutions of 0.2 s and 12 s respectively. These data enabled us to jointly measure the intracellular flow and traction forces generated by the amoebae, which oscillate with a much slower period of ~ 100 sec [15].

Physarum's dense distribution of intracellular vesicles was exploited to determine intracellular streaming velocities from the transmitted light images using particle image velocimetry (PIV) [15, 41]. The raw image sequences were pre-processed for PIV by applying high-pass, band-pass and low-pass temporal filters, which allowed us to resolve the flow inside narrow channels (see Figure 3.2(a)). The resulting spatial resolution of the flow measurements was 6.5 μm.

The three-dimensional deformation produced by *physarum* amoebae on the PA substrate was measured by tracking the displacements of the embedded fluorescent beads as described by del Álamo et al. [28]. From the measured deformation, we computed the traction stresses (see Figure 3.2(b)) and strain energy (see Figure 3.9) generated by the cells using Fourier TFM methods described elsewhere [28, 31]. The spatial resolution of these measurements was 13 μm.

3.3 Mathematical Model

Our model of the cell incorporates the effects of intracellular liquid (cytosol), the solid internal cell structure (cytoskeleton), and interaction with the extracellular substrate (through adhesion) in a moving geometry defined by the cell membrane and underlying cortex (see Figure 3.1). The model is described by the balance of forces on three materials: the liquid cytosol, the porous elastic cytoskeleton, and the adhesive complexes which mechanically couple the cell interior to the substrate. The velocity of the viscous cytosol ($\vec{u}_f$) satisfies the forced Stokes equations. The fluid forces (viscosity and pressure) are balanced by body forces from the drag due to the internal cytoskeleton ($\vec{f}_{\text{drag}}$) and the elastic forces on the membrane/cortex which bounds the cell ($\vec{f}_{\text{mem}}$). The forces acting on the cytoskeleton are the elastic forces due to deformation ($\vec{F}_e$), an active contractile force due to myosin molecular motors in the actin network ($\vec{F}_a$), drag due to the cytosol ($\vec{F}_{\text{drag}}$), forces due to adhesions to the substrate ($\vec{F}_{\text{adh}}$), and forces generated by attachment of the cytoskeletal network to the surrounding membrane/cortex ($\vec{F}_{\text{net}}^{\text{attach}}$). Finally, the adhesion complexes are subject to forces applied by the external substrate ($\vec{F}_{\text{subs}}$), balanced by the forces which the complexes

apply to the internal cytoskeleton. The system of equations which describe these force balances is

$$\mu \Delta \vec{u}_f - \nabla p + \vec{f}_{\text{drag}} + \vec{f}_{\text{mem}} = 0, \tag{3.1}$$

$$\nabla \cdot \vec{u}_f = 0, \tag{3.2}$$

$$\vec{F}_e + \vec{F}_a + \vec{F}_{\text{drag}} + \vec{F}_{\text{adh}} + \vec{F}_{\text{net}}^{\text{attach}} = 0, \tag{3.3}$$

$$\vec{F}_{\text{subs}} - \vec{F}_{\text{adh}} = 0. \tag{3.4}$$

These equations effectively describe the cell interior as an actively contractile poro-elastic network. A similar model (with an additional description of chemical kinetics) has been used to investigate symmetry breaking and the onset of contractile waves in *Physarum* microplasmodia [24, 46]. For a description of how we compute these forces and the material parameters, see [47].

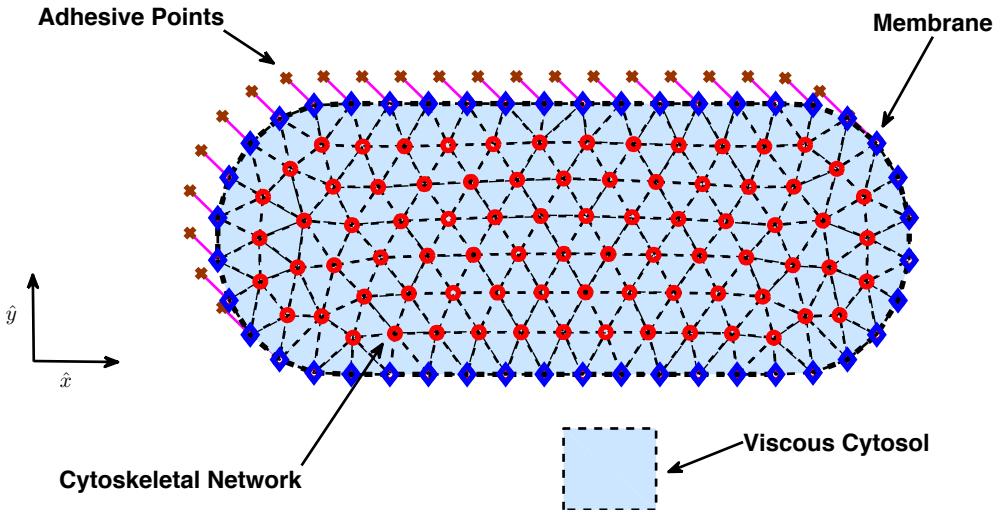

Figure 3.1: A schematic of our computational model of a *Physarum* plasmodium. Cytoskeletal network points are shown as red circles. Membrane points are shown as blue diamonds. Adhesive points are illustrated as brown exes. Viscous cytosol that permeates the porous media is illustrated as light blue shading.

The active contractile force ($\vec{F}_a$) drives the deformation of the cell and the flow of cytosol. We assume that this force is generated by a traveling wave of isotropic contractile

stress with magnitude

$$\Sigma_a(x,t) = \frac{C}{2}\left(\cos\left(\frac{2\pi}{\ell_{\text{cont}}}x - \frac{2\pi}{T}t\right) + 1\right), \tag{3.5}$$

where C is the maximum contractile stress, ℓ_{cont} is the wavelength, and T is the period. The spatial variable x is the the longitudinal body coordinate of the cell. The wave travels along the body (from posterior to anterior) with wavespeed ℓ_{cont}/T. We assume that the resulting wave of cell shape deformation is directly correlated with the underlying cytoskeletal contraction and choose $\ell_{\text{cont}} = 1600$ μm (four body lengths) and $T = 100$ sec, which is consistent with the wavelength and period of deformation reported in [15] and with our own experiments. Similarly, the value of C is chosen so that the resulting deformations of the model cell are on the same scale as those observed in experiments.

Many of the material parameters can be measured or estimated. Conversely, the precise nature of the proteins with which *Physarum* adheres to the substrate is not known, even if some candidates have been identified [48]. The period of the deformations observed in *physarum* is long (~ 100 sec) compared to the timescale of the dynamics of a cell-substrate bond, and so we represent the dynamics of adhesion via a viscous drag law [49] of the form

$$\vec{F}_{\text{subs}} = -\zeta(x,t)\vec{U}_{\text{adh}}, \tag{3.6}$$

where $\vec{U}_{\text{adh}}$ is the velocity of the adhesion complexes (relative to the substrate), and ζ is a viscous interaction coefficient. In Section 3.4.5 we investigate an idealized ζ of the form

$$\zeta(x,t) = \frac{A}{2}\left(\cos\left(\frac{2\pi}{\ell_{\text{adh}}}x - \frac{2\pi}{T}t + \phi\right) + 1\right) + \epsilon. \tag{3.7}$$

This choice of ζ is inspired by the observation that both the deformation of, and associated flow within *Physarum* appear to propagate from the posterior to the anterior of the cell as a traveling wave (discussed in more detail in Section 3.4). The wavelength ℓ_{adh} and period T of the adhesion modulation are assumed to be the same as those of the contractile wave. The parameter ϕ represents the phase of the coordinated adhesion *relative* to the traveling wave of contraction strength (eq. (3.5)). The amplitude parameter A is a measure of the strength of active coordinated adhesion, and will often be referred to as the "coefficient of adhesion" in the following text. The parameter ϵ represents nonspecific adhesive interactions between the substrate and the basal surface of the cell. We report coefficient of adhesion in

nondimensional units of $[A/\epsilon]$.

3.4 Results

3.4.1 Cell Behavior

Upon reaching an adequate size (approximately 100 μm across), we observe the cells elongate into a tadpole-like shape concurrent with the onset of a rhythmic, pulsating flow of cytosol. In most cases, this behavior is similar to that reported in [15], with waves of contraction and flow traveling from posterior to anterior along the long axis of the cell. We refer to these cells as "peristaltic." We also observe a second mode of deformation which we call "amphistaltic" due to the fact that the front and rear contract and relax in an anti-phase manner. The amphistaltic amoeboid mode could be the precursor of the contractile dumbbells found by Rieu et al. in the companion paper [40]. Of the 21 cells we study, 10 of them clearly exhibit the peristaltic behavior, while 6 are amphistaltic. For an illustration of the difference between these modes, see Supplementary Information. Approximately 5 of the cells we observe do not obviously fall into the category of peristaltic of amphistaltic mode, and exhibit characteristics of each. The peristaltic mode appears to be stable on timescales of at least 1000 sec. After this, the cells migrated far enough to leave the observation window. In this work we focus only on the peristaltic cells due to the fact that they migrate approximately twice as fast as amphistaltic cells, and are consistent with the experiments of previous investigations [15].

In peristaltic cells, the cytoplamsic flow is primarily directed along the cell centerline from its anterior to its posterior end (hereafter referred to as the longitudinal or cell axis), and has a distinct period of 90 ± 12 sec (measured over 10 cells). A region of cytoplasmic flow directed forward develops at the cell rear. This pattern of forward flow becomes more prominent and travels along the cell axis toward the cell front. Eventually, a region of flow directed backwards emerges at the cell rear, and it also propagates toward the the cell front, before the entire pattern repeats. Figure 3.2(a) shows three instantaneous measured velocity fields: a fully developed forward flow pattern, a fully developed backward directed flow pattern, and the final stages of the backward flow pattern, as a new forward flow begins at the posterior of the cell. The emergence of this periodic wave of back-and-forth flow is observed to coincide with a dramatic increase in the migration velocity of the cell [39].

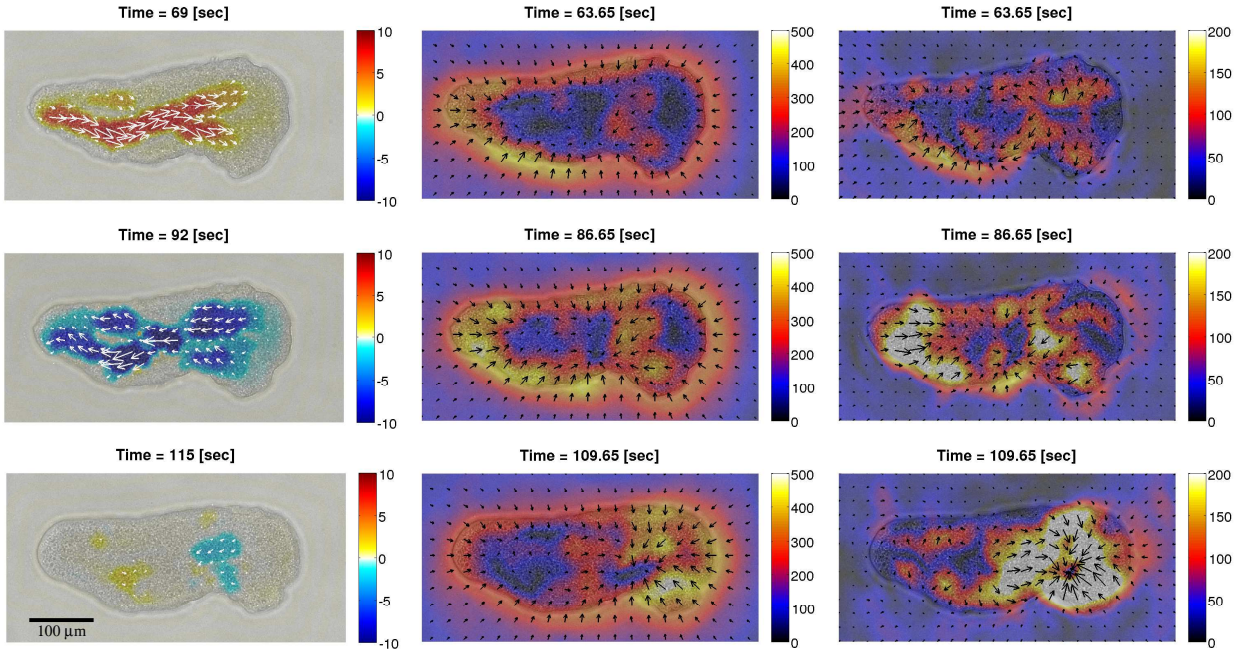

Figure 3.2: (a) Instantaneous intracellular flow observed in migrating *physarum*. Arrows indicate the direction of flow, colormap indicates the projection of flow velocity onto the cell axis [μm/sec]. (b) Instantaneous traction stresses exerted on the substrate. Arrows indicated the direction of traction stress, colormap indicates the magnitude [Pa]. (c) Traction stresses with the moving cortical average removed. Arrows indicate the direction of stresses, colormap indicates the magnitude [Pa]. All arrow fields are downsampled by a factor of 4 in each direction for visual clarity.

The migration of the cell is necessarily accompanied by the application of traction stresses to the substrate. Figure 3.2(b) shows a sequence of the stresses applied to the substrate by *Physarum* at three time points which are approximately those reported in Figure 3.2(a). There is a slight time difference between the images of (a) and (b) due to changing the imaging channel of the microscope from bright field to fluorescent field. Supplementary Movie 1 shows the joint time evolution of intracellular flow and traction stresses for the cell in Figure 3.2.

The dominant feature of this traction stress pattern is purely contractile, with the larger stresses distributed along the cell periphery. This behavior has been observed in other cell types, and it has been hypothesized that this effect is due to strong stresses associated with the cell cortex and directed out of the plane of the substrate [13]. Because our model only considers in-plane stress, we remove the average "cortical" stress from the measured stress field to compare with model predictions. At each instant of time, the average trac-

tion stress field is compiled from the traction stresses recorded during the previous, current and following periods of the observed behavior. We then remove the average contractile stress from the instantaneous traction stress field, yielding the stress patterns shown in Figure 3.2(c). This procedure reveals loci of expansive and contractile stress that propagate from the posterior to the anterior. As the expansive locus leaves the front of the cell, a new one develops behind the contractile locus.

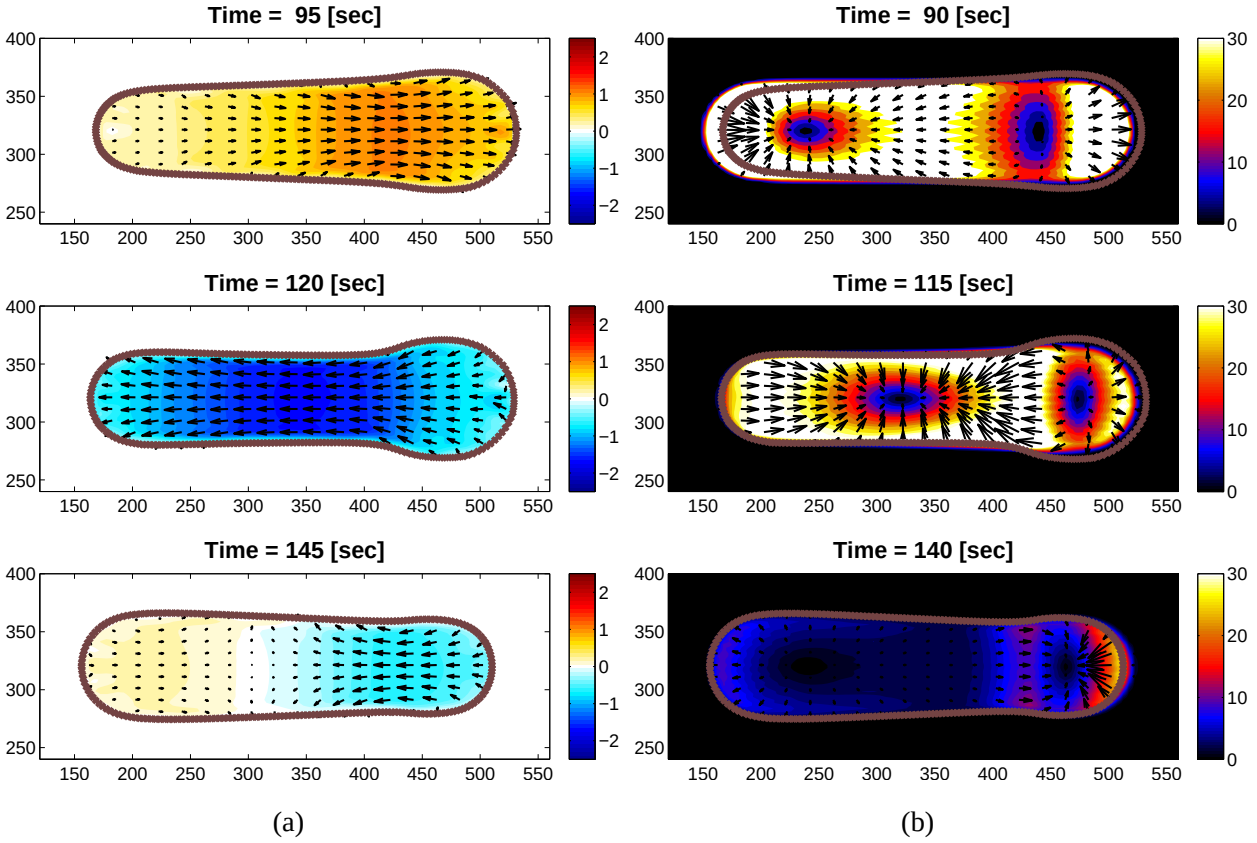

Figure 3.3: (a) Instantaneous intracellular flow computed in model cell. Arrows indicate the direction of flow, colormap indicates the projection of flow velocity onto the cell axis [μm/sec]. (b) Instantaneous traction stresses computed in model cell. Arrows indicate the direction of stress field, colormap indicates the magnitude of stress field [Pa]. Again, all arrow fields are downsampled by a factor of 4 in each direction for visual clarity.

3.4.2 Comparison of Model Behavior

In this section, we illustrate the behavior of our model simulations and compare with experimental observations. All simulations were run with $\phi = 3\pi/2$ and $A = 100\epsilon$, respectively. In Sections 3.4.4 and 3.4.5 we justify this choice and consider other adhesion

parameters. In Figure 3.3(a) we show instantaneous fluid velocity fields obtained from the model at time intervals analogous to Figure 3.2. The three panels illustrate a fully developed forward flow, a fully developed region of backward flow, and the onset of a forward flow pattern at the posterior of the cell (Supplementary Movie 2 shows the time-resolved animation). Qualitatively, they are very similar to the behavior shown in Figure 3.2(a). In Figure 3.3(b) we provide illustrations of traction stress fields ($\vec{F}_{\text{trac}}$) generated by our model cell during the same simulation shown in Figure 3.3(a). The time points shown are offset from those in Figure 3.3(a) for a more direct comparison with experiments. The three panels show the forward propagation of a contractile locus of stress through the cell body, as well as a locus of expansive stress that exits the anterior of the cell before a weaker one emerges at the posterior (Supplementary Movie 3 shows the time-resolved animation). In this regard, the model again reproduces the qualitative behavior observed in live *physarum*.

To further analyze the flow patterns that we observe (or our model predicts), we generate kymographs of the measured (or calculated) longitudinal flow averaged over each lateral cross section of the cell,

$$\overline{U}(x,t) = \frac{\int_{\Omega_c} \vec{u}_f \cdot \hat{x}\, dy}{\int_{\Omega_c} dy}, \tag{3.8}$$

where Ω_c denotes the interior of the cell, x is the longitudinal coordinate, y is the coordinate orthogonal to the longitudinal axis, and $\hat{x}$ is unit vector oriented towards the anterior of the cell. Similarly, we compare kymographs of the observed and measured traction stresses by defining

$$\overline{S}(x,t) = \frac{\int_{\Omega_c} \vec{F}_{\text{trac}} \cdot \hat{x}\, dy}{\int_{\Omega_c} dy}, \tag{3.9}$$

which measures the average traction stress *in the direction of motion* at each cross section of the cell body.

Figure 3.4 shows experimental measurements of $\overline{U}$, together with results for the model cell. For both our experiments and simulations, we observe flows in good agreement with those reported previously [15]. A periodic pattern is clearly evident, where regions of forward and rearward flow are generated at the back of the cell, and quickly propagate toward the front in an approximately linear fashion. We refer to this pattern as a "phase wave," and to its propagation speed as the "phase velocity", c_ϕ. In previous experiments this phase velocity was reported as $c_\phi = 12 \pm 1$ μm/sec [15]. Here, we measure higher phase velocities,

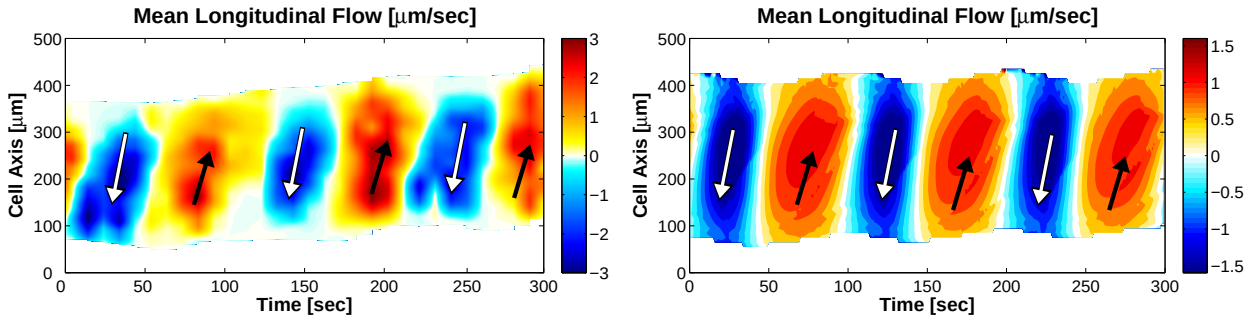

(a) (b)

Figure 3.4: Kymographs of mean longitudinal flow $\overline{U}$. (a) Data recorded in migrating phys. (b) Values predicted by model simulation. Filled arrows indicate flow directed foward. Open arows indicate regions of backward flow.

$c_\phi = 23.8 \pm 12.0$ μm/sec across our experiments, and our model predicts $24 \leq c_\phi \leq 38$ μm/sec.

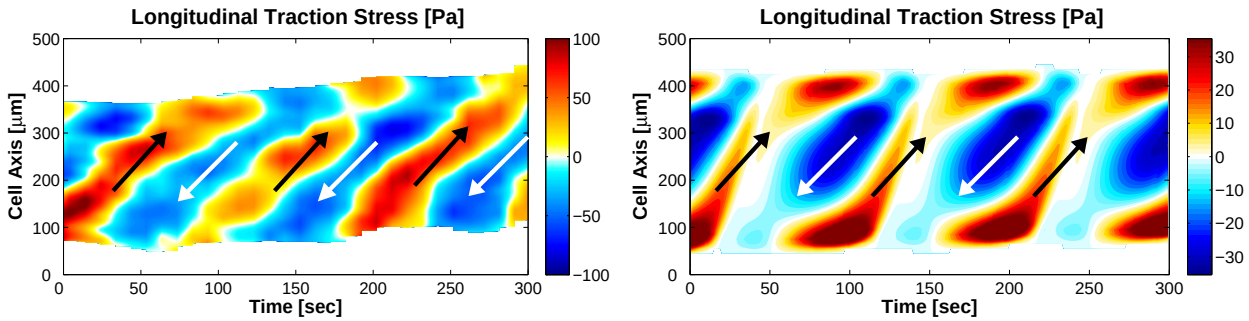

(a) (b)

Figure 3.5: Kymographs of mean traction stress $\overline{S}$. (a) Data recorded in migrating phys. (b) Values predicted by model simulation. Filled arrows indicate regions of stress directed forward. Open arrows indicate stress directed backward.

Figure 3.5(a) shows a kymograph of traction stresses measured in the same experiment as Figure 3.4(a) (with average cortical stresses removed). The data displayed are qualitatively representative of a large number of experiments. For comparison, Figure 3.5(b) shows a traction stress kymograph for the model cell. In the kymographs, we see a distinct phase wave of adhesion stress similar to the flow pattern in Figure 3.4. However, we note that in both experiments and our model, the phase velocity of the flow patterns is approximately four times faster than that of the traction stress patterns. The numerically calculated traction kymograph reproduces the main features of the traction stresses observed in live *physarum*. However, model and experiment do not agree in all respects. For example,

for these parameters our model predicts the maximal forward stresses occur at the anterior and posterior of the cell while this does not appear to be the case in experiments. Altering parameters changes this aspect of the model predictions, but may cause other disagreements with experiments. It is difficult to identify by visual inspection which adhesion parameters *most closely* reproduce the spatiotemporal dynamics of the adhesion stress observed in experiments. In Section 3.4.5, we develop a more quantitative analysis of the coordination of adhesion to compare experiments and calculations.

3.4.3 Role of Flow

It is argued in [15] that the asymmetry in the motion of a fluid particle in such a flow pattern is directly responsible for the net displacement of the cell. Figure 3.6(a) illustrates this argument by showing particle paths in an idealized flow where regions of forward and backward flow propagate through the cell body. A particle translates forward and then backward with the same speed over one period of the wave. The particle is in a region of forward flow for more than half the period, resulting in net forward displacement. We define the asymmetry in the flow to be the ratio of the forward and backward displacement of such a particle path. Figure 3.6(b) shows the displacement of the centroid of a *Physarum* specimen. We define the centroid displacement asymmetry to be the ratio of the forward and backward displacements of the centroid over one period. In Figure 3.6(c), we plot the asymmetry in the flow as a function of the centroid displacement asymmetry, measured in our experiments. If the flux of mass due to the intracellular flow wave were solely responsible for the migration of the cell center of mass, then the data in Figure 3.6(c) would lie on the green dashed line with slope 1. However, this line is in fact a poor fit to the data, while the best linear fit (solid blue line) has a much lower slope of ≈ 0.16.

Examining Figure 3.6(c) more closely reveals a critical phenomenon. We observe that 45% of the data points have a flow asymmetry less than unity, despite having a centroid asymmetry greater than unity (lower right quadrant in the figure). Thus, for a significant fraction of our observations the intracellular flow suggests a net *backward* translation of mass, even though the cell has moved forwards. For comparison, in Figure 3.6(d), we show flow kymographs from two cells. Cell A (marked with upward triangles in Figure 3.6(c)) predominantly exhibits a flow asymmetry less than one, while Cell B (marked with downward triangles in Figure 3.6(c)) predominantly exhibits a flow asymmetry greater than one. Both

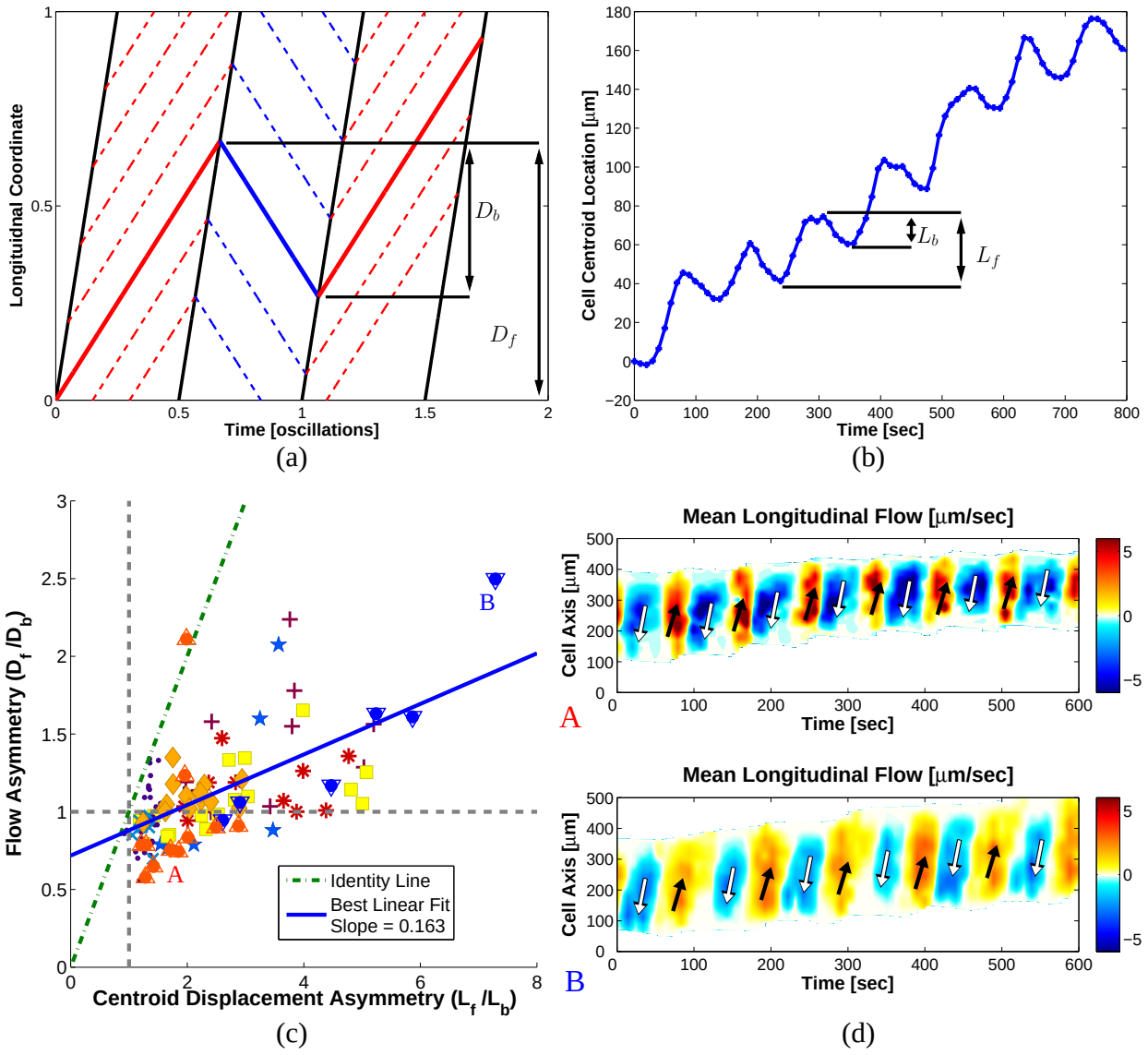

Figure 3.6: (a) An illustration of particle paths associated with a constant phase wave. The forward and backward particle displacements (D_f and D_b) are shown. Flow asymmetry is defined to be D_f/D_b. (b) A time series of the centroid of a migrating *physarum*. The forward and backward centroid displacements (L_f and L_b) are shown. Centroid displacement asymmetry is defined to be L_f/L_b. (c) Experimentally measured values of flow and centroid displacement asymmetry over 118 periods (each data point) and 9 cells (distinguished by distinct markers). The best linear fit is shown in blue. The line $D_f/D_b = L_f/L_b$ in green for comparison. (d) Flow kymographs from the cells marked A (upward triangles) and B (downward triangles) in (c), illustrating flow asymmetry less than and greater than one respectively.

exhibit similar phase velocities of the flow wave. While intracellular flow is likely to play a role in the migration of *physarum*, our experiments (and model predictions in Section 3.4.4)

indicate that intracellular flow kinematics alone cannot determine the migration of the cell.

3.4.4 Adhesion Coordination and Crawling Speed

Figure 3.7 shows the centroid trajectories and flow kymographs for three cells generated with the model using different forms adhesion coordination. Cell A utilizes a phase parameter of $\phi = 3\pi/2$ and an adhesion coefficient of $A = 100\epsilon$. Cell C utilizes the same adhesion coefficient, and a reversed phase parameter of $\phi = \pi/2$. Cell B was simulated with $\phi = 3\pi/2$ and adhesion coefficient $A = 0$. All three of these cells are driven with the same contraction pattern, but more importantly exhibit very similar flow patterns which are all consistent with both our experiments and experiments of others [15, 39]. However, while cell A migrates forward consistent with experimental observations, cell B shows no net translation over the course of the simulation, and cell C migrates *backwards*. The implication is that while hydrodynamic effects may generate stresses integral to motility, it is the coordination of the transmission of those stresses to the substrate that ultimately determines motility. Furthermore, from Cell B we see that *coordinated* adhesion is critical to motility. A cell migrating using just the nonspecific, uncoordinated adhesion (ϵ) fails to migrate.

For comparison, Figure 3.6(b) provides a time course of the center of a *Physarum* specimen migrating in the lab. Qualitatively, the predicted migration behavior of model cell A closely matches that observed in our experiments. We see a distinct, periodic translation forward and backward, with a pronounced asymmetry to the two translations resulting in a net forward displacement of the cell. For the simulation shown, the net displacement of the model cell is approximately 6 μm per period, which is is equivalent to an average migration velocity of ≈ 0.06 μm/sec. In the laboratory, we measure *Physarum* migrating at speeds of 0.169 ± 0.041 μm/sec across the 10 cells which exhibit peristaltic behavior. Thus, our model predicts *Physarum* migration in reasonable agreement with experiments, and suggests that coordination of adhesion and contraction is essential for efficient locomotion.

We now explore the speeds of migration predicted by the model as a function of adhesion strength and coordination. We perform simulations varying the phase parameter (ϕ) over eight equally spaced values from 0 to 2π, and the coefficient of adhesion (A) over 6 orders of magnitude. All parameter values give rise to similar periodic displacements (as shown in Figure 3.7). However, depending on the phase and strength of adhesion, our model predicts various translation velocities and *directions* of migration (Figure 3.8).

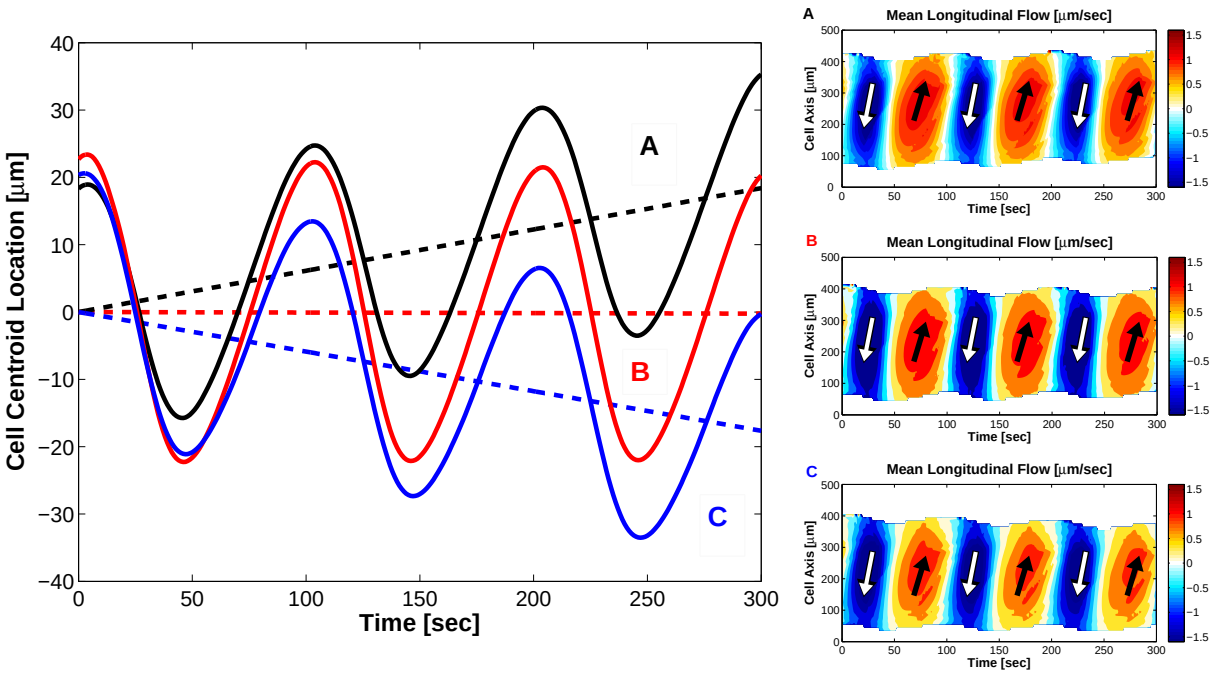

(a) (b)

Figure 3.7: Numerically calculated time sequence of cell center is shown in (a). The solid lines indicate the centroids of individual cells, while the corresponding dashed lines indicates a best (least squares) linear fit. Migration speeds reported are given by the slope of this fit. The flow kymographs of $\overline{U}$ for each cell are shown in (b). Filled arrows indicate forward flow. Open arrows indicate regions of backward flow.

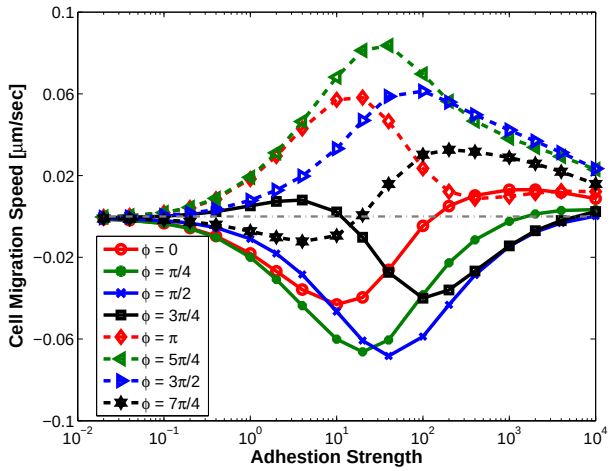

Figure 3.8: Average cell crawling speed as a function of adhesion coefficient and adhesion phase. Adhesion coefficient is reported in non-dimensional units $[A/\epsilon]$. Dashed grey line indicates zero migration velocity.

We observe that the migration velocity of the model cell is a non-monotonic function of adhesion coordination and strength. Indeed, the cell speed is maximal at moderate values of coordinated adhesion, while uncoordinated or strongly adherent cells display negligible migration. In the limit $A << \epsilon$, the coordinated adhesion is negligible compared to the uniform, uncoordinated adhesion and the cell cannot move directionally despite generating periodic cell shape changes (see cell B in Figure 3.7). In the limit of strong adhesion $A >> \epsilon$, the cell is effectively stuck to the substrate and cannot move even if this adhesion is highly coordinated. Experiments performed on highly adhesive substrates coated with collagen and the polycation poly-L-Lysine [50] are qualitatively consistent with the model predictions. *Physarum* amoebae migrating on these sticky substrates adopt a tadpole shape, and create peristaltic contraction waves and intracellular streaming. However, they barely move (see Supplementary Movie 4).

As each simulation is driven with active contractions of the same amplitude and form, we may consider migration speed of the cell as a measure of efficiency. The cell translates most efficiently with an active adhesion coefficient of $A/\epsilon \sim$ 10–100, and a coordination phase of $\phi \sim \pi$–$3\pi/2$. Thus, the model predicts an optimal parameter regime in which to drive motility. However, the parameters A and ϕ are not measurable in our experiments. In the next section, we develop a quantitative measure of the relative timing of *flow* and *adhesion* within *physarum*. This will be used to determine if these model parameters are consistent with experiments.

3.4.5 Adhesion Correlation

We examine the time evolution of the strain energy exerted by live migrating *Physarum* on their substrate (Equation S.5), and compare it with the evolution of the average intracellular flow velocity. The results show a distinct periodic pattern in both variables, with the flow wave preceding the adhesion wave by approximately a quarter period (Figure 3.9, left panel). This behavior is robust across the 9 reported experiments. To more precisely quantify this phase relationship between flow and adhesion energy, we calculate the cross correlation of flow and adhesion energy, as well as the autocorrelation of the flow wave (Figure 3.9, right panel). The distance between peaks of the autocorrelation function is interpreted as the period of the flow wave oscillation (T). The position of the first peak (restricted to times $t > 0$) of the cross correlation function indicates the relative timing of the flow and energy

waves (θ). The ratio θ/T defines the relative phase (between 0 and 1), which we measured to be 0.34 ± 0.07 in our experiments.

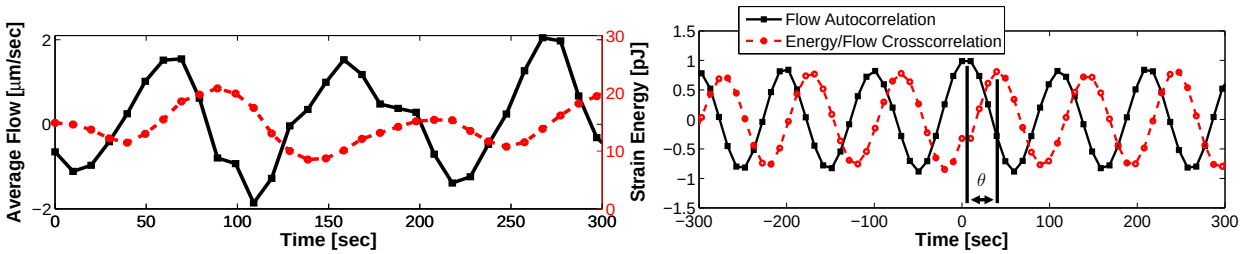

Figure 3.9: Experimentally measured flow (solid) and energy (dashed). Left panel shows average flow velocity within the cell interior, as well as total strain energy of adhesion as a function of time. Right panel shows auto and cross correlation of flow and energy, as well as the relative timing θ.

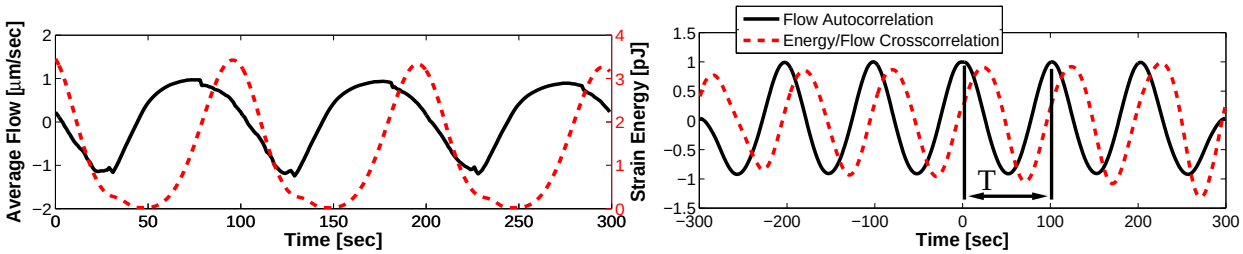

Figure 3.10: Numerically calculated flow (solid) and energy (dashed). Left panel shows average flow velocity within the cell interior, as well as total strain energy of adhesion as a function of time. Right panel shows auto and cross correlation of flow and energy, as well as the period T.

We perform the same analysis for the model simulations. Figure 3.10 shows the average intracellular fluid velocity and strain energy within the model adhesions, as well as the auto and cross correlation of these two time sequences. The data shown is for a cell with $\phi = 3\pi/2$ and $A = 100\epsilon$, which is the same parameter set used for the forward moving cell in Figure 3.7, as well as Figures 3.4 and 3.5. For these parameters, the model reproduces accurately the observed phase relationship between flow and energy waves. We see a clear phase lag of approximately a quarter period.

Given the good agreement between model and experiments, we utilize the phase relationship between flow and energy to identify plausible adhesion parameters in the model. The results are shown in Figure 3.11(a), where we report the relative phase lag of the energy wave, in periods of the wave, for all simulations shown in Figure 3.8. For reference, the relative phase observed in experiments (0.34 ± 0.07) is illustrated with the solid and

dashed grey lines. The relative phase of adhesion energy appears to be highly sensitive to ϕ, and relatively insensitive to adhesion strength (beyond the range $A \approx \epsilon$). Values of ϕ in the range $3\pi/2$–2π (2π and 0 are equivalent) produce a relative timing which is consistent with experimental measurements. Of these parameter values, $\phi = 3\pi/2$ is the only one which produces migration in the forward direction regardless of the strength of coordinated adhesion. For cells using $\phi = 3\pi/2$, the phase lag between flow and strain energy remains in the range 0.21–0.33 when varying the adhesion strength over 6 orders of magnitude. Specifically, in the case of highest migration velocity, we measure a phase lag of 0.25. In Figure 3.11(b) we show the average adhesion timing θ/T (calculated for all values $A > \epsilon$) and the maximum signed migration velocity for each value of the coordination parameter ϕ. Again, we see that of the values of ϕ which are consistent with experiment, $\phi = 3\pi/2$ produces the maximum migration velocity.

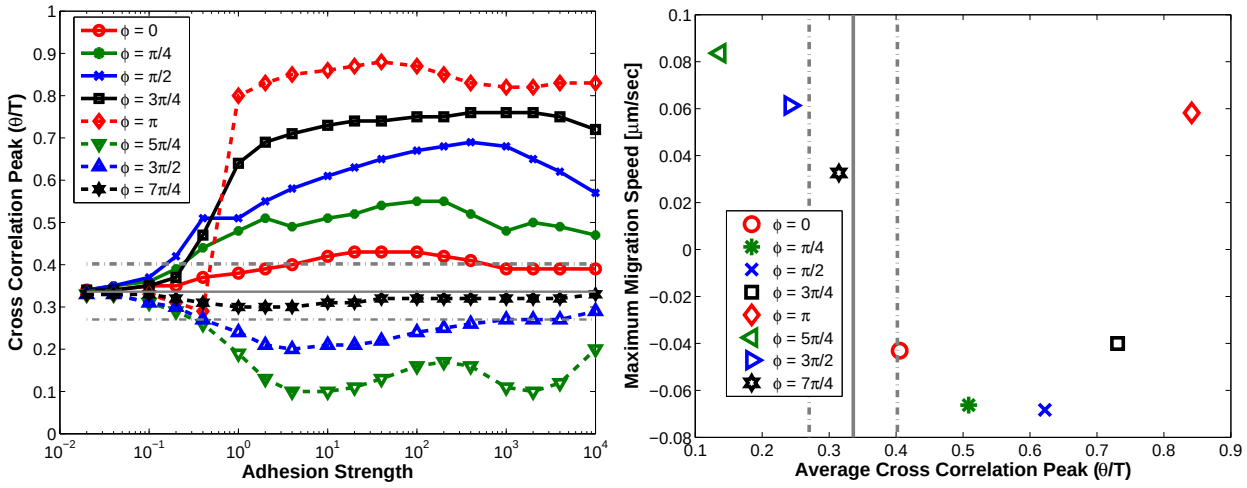

Figure 3.11: Panel (a) shows maximum cross correlation of elastic energy of adhesion and average cytoplasmic flow. Adhesion coefficient is reported in non dimensional units $[A/\epsilon]$. Horizontal grey lines indicates experimentally measured phase of 0.34 ± 0.07. Panel (b) shows the average adhesion timing and maximum migration speed for each value of adhesion coordination ϕ. Vertical grey lines indicates experimentally measured phase of 0.34 ± 0.07

3.4.6 Robustness

From the criteria discussed above, the spatiotemporal pattern of adhesion which is most consistent with experimental evidence corresponds to a phase lag of $\phi \approx 3\pi/2$ and

a strength of $A \approx 100\epsilon$. Furthermore, these parameters predict nearly optimal migration velocity within the constraints of the model. It is noteworthy that this optimal migration velocity is not sensitive to the strength of adhesion. Returning to Figure 3.8, we see that the model predicts a migration velocity above 0.03 μm/sec (roughly 50% of maximal) over more than *two decades* of adhesion strength. Thus far, our simulations consider only spatially uniform substrates. In relevant environments, the strength of adhesive interactions between the cell and substrate is not homogenous, as numerous extracellular and intracellular factors may affect such interactions. Therefore, we modify our model to quantify the robustness of migration with respect to spatial variations in adhesion strength. We alter the model of cell adhesions to the substrate in order to incorporate spatial heterogeneity. The existing form of adhesion (eq. (3.7)) is replaced with

$$\zeta(x,t) = \frac{A}{2} g(x_{\text{lab}}, y_{\text{lab}}) \left(\cos\left(\frac{2\pi}{\ell_{\text{adh}}} x - \frac{2\pi}{T} t + \phi \right) + 1 \right) + \epsilon, \tag{3.10}$$

where $g(x_{\text{lab}}, y_{\text{lab}})$ is a randomly constructed function of fixed laboratory coordinates. By construction, this function has mean of $\mu_r = 1$ and standard deviation $\sigma_r = 0.34$. This has the effect of spatially modulating the strength with which the cell adheres to the substrate.

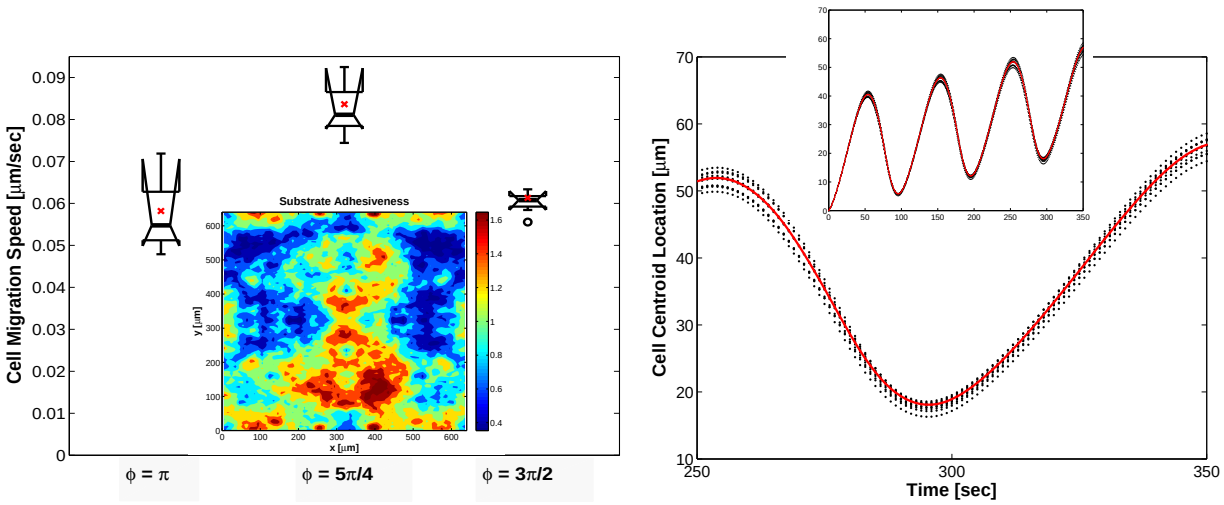

(a) (b)

Figure 3.12: (a) Open circles indicate outliers in data set. Filled red points indicate the migration velocity calculated for a cell migrating across a homogeneous substrate. The inset shows a single randomly generated example of the spatial heterogeneity $g(x, y)$. (b) Dashed black lines indicate time course of centroids of cells migrating across random substrate. Solid red line indicates cell migrating across homogeneous substrate. $\phi = 3\pi/2$ in all cases.

Using the randomly constructed function g to represent a heterogeneous substrate, we simulated cells migrating across ten different substrates. We performed these simulations for the three values of ϕ which generically resulted in forward migration, and values of coordinated adhesion that results in the greatest migration velocity for each phase parameter. This means $\phi = \pi,\ 5\pi/4,$ and $3\pi/2$, with $A = 20\epsilon,\ 40\epsilon,$ and 100ϵ, respectively. The results are summarized in the box plot of Figure 3.12(a). The spread of the data shows that migration speed is relatively insensitive to substrate heterogeneity for the considered values of ϕ. Notice that the value $\phi = 3\pi/2$, which is most consistent with our live *Physarum* experiments, produces a substantially lower spread in migration speed, with half the data falling within $\pm 2.5\%$ of the median value. Thus, this spatiotemporal pattern of adhesion coordination is highly robust with respect to local variations in the strength of substrate adhesiveness.

Figure 3.12(b) shows the time evolution of the centroid of the 10 cells with random adhesion strength for $\phi = 3\pi/2$ (black), compared with the homogeneous substrate case (red). The inset shows the full time course, while the main panel shows just the final 100 sec of migration. Over time, the location of the cells migrating across random substrates begins to deviate as random effects accumulate over time. However, these deviations are quite small compared to the scale of cell migration. This result indicates that, for the set of model parameters that reproduce the experimental measurements, the instantaneous speed of migration is remarkably insensitive to the spatial heterogeneity of the substrate throughout the whole oscillation period.

3.5 Discussion

Migrating amoeboid cells such as *Physarum* microplasmodia apply highly dynamic traction forces on their surroundings, leading to large shape changes and fast intracellular streaming flows. However, there is a paucity of simultaneous measurements of traction forces and intracellular streaming, which has made it difficult to develop mechanistic models that relate the forces driving amoeboid motion and the cellular deformations realizing this motion.

In this work, we combine simultaneous measurements of cytoplasmic flow and the traction stresses in migrating *physarum* microplasmodia, with detailed computational models of amoeboid migration that resolve the mechanics of cellular deformation and substrate adhesion. Our measurements reveal that *Physarum* amoebae move by creating traveling

waves of contractile traction stresses with a well defined period of ~ 100 sec. The traction stress waves are similar in character to the previously observed waves of intracellular flow, but the flow waves consistently precede the stress waves by $\sim 1/4$ cycle. Inspired by this observation, we use our numerical model to investigate the consequences of migration using traveling waves of coordinated contraction and adhesion. Our investigations show that, by altering the timing of adhesion relative to the flow wave, the cell is able to migrate with different velocities and in different directions. These findings transform the previously established view that directional migration of *Physarum* amoebae is caused by the directionality of the flow waves [15].

By juxtaposing our modeling and experimental work, we have identified specific forms of generation and transmission of cellular forces which plausibly drive the migration of *Physarum* amoebae. Within the context of our adhesion model, our simulations and experiments reveal a distinct pattern of spatiotemporal coordination between contraction and adhesion which reproduces the experimentally measured cytoplasmic flows and traction stresses, and the scale of cell migration speed. This coordination pattern consists of a phase lag of 3/4 cycle between adhesion and contraction ($\phi \approx 3\pi/2$). In addition to validating the model, this result provides insight into the underlying mechanism of amoeboid motility. The particular adhesion coordination pattern we highlight is extremely robust to perturbations in adhesive interactions with the extracellular environment, and results in nearly maximum migration speed within the context of the model. Interestingly, the adhesion coordination pattern that produces maximum migration speed ($\phi = 5\pi/4$) is less robust, possibly because it does not properly reproduce the relative timing of flow and traction stress. This insight into the potential compromises of different adhesion coordination would not have been possible through experimental investigations alone. Our model allows us a direct control over the coordination of adhesion that we are unable to control in a laboratory setting.

We note that our frictional adhesion model is rather independent of the precise nature of the cell-substrate interactions. While this model could be justified as a time averaged effect of integrin-like molecular binding, this assumption is not necessary to arrive at the precise mathematical form that we use. Indeed, it is unclear how *Physarum* exerts stresses on its surroundings. Previous models have suggested that wave-like patterns of contraction may spontaneously arise from the coupling of the mechanics and chemistry of contraction in *Physarum* [24, 46]. It is plausible that a similar mechanism may give rise to a wave-like modulation of the strength of adhesive interactions. Though it is unlikely that microplasmodia

migrate utilizing adhesive patterns as simple as our idealized wave of adhesion, our modeling assumptions are consistent with a variety of possible mechanisms. More experimental investigation into the specific nature of *physarum*-substrate interaction is required.

While somewhat unique, the motility of *Physarum* microplasmodia shares fundamental characteristics with other forms of amoeboid migration. Rythmic cellular contractions of period ~ 100 sec are known to drive the motion of neutrophil-like and *Dictyostelium* amoeboid cells [14, 31]. In particular, while intracellular flow kinematics do not fully determine the motility of *physarum*, our results suggest that cellular contractions are used to generate intracellular flows and cell locomotion. The use of pressure-driven flows of cytoplasm to generate translation has been widely observed in motile cells [2, 14, 51]. This is in contrast to cell types which utilize the polarity of actin filaments to generate polymerization-driven protrusions such as lamellapodia and filapodia [52]. Our experimental model does not generalize to this type of motility, but our modeling framework could be adapted to account for network polarity and polymerization stresses. Furthermore, the observed motility of *Physarum* is consistent with a model of cell-ECM interaction that does not require specific integrin-like binding molecules. It has been shown that neutrophils undergo amoeboid migration in three dimensional environments in the absence of specific binding molecules [4]. This contributes to the growing notion that friction mediated motility is biologically advantageous, as it is robust to geometric and mechanical changes in the ECM [3, 51].

The form of amoeboid motility we observe in *Physarum* also shares many characteristics with locomotion in higher organisms. The traveling wave of contraction is similar to contraction patterns observed in migrating gastropods, annelids, and *dictyostelium* slugs. In both experimental and theoretical investigations of these organisms, it has been seen that the direction of contraction wave propagation is not the critical factor in determining migration direction. Rather, migration results from the timing of interactions between the organism and substrate [9, 53]. As we have previously discussed, this same behavior is observed in our model.

While *Physarum* locomotion shares this behavior with various gastropods and annelids, we note that the amoeba moves on a vastly different scale than these organisms. The slugs observed in [9] ranged from 0.7-28 cm in length, while *Physarum* microplasmodia begin to migrate in this fashion after reaching a size of approximately 100 μm. This seems to indicate that a motility mechanism predicated on traveling waves of strain and appropriately timed adhesive interactions represents a robust design principle; one which is viable across

length scales from cellular to macro. Indeed, the advantageous characteristics of *Physarum* have not gone unnoticed by the robotics community, where the organism has been the inspiration for biomimetic design [22, 54].

We would like to thank T. Nakagaki and J.P. Rieu for their stimulating discussions, which contributed to this work. We would also like to acknowledge the input of Ruedi Meili and Juan C. Lasheras. Authors Lewis and Guy were supported by NSF grant DMS–1160438 and NSF grant DMS–1226386. Authors Zhang and del Álamo were supported by NSF grant CBET–1055697 and National Institutes of Health grant 5R01GM084227–03.

3.6 Acknowledgements

Chapter 3, in part, has been published in the *Journal of The Royal Society Interface*. Lewis, Owen L ; Zhang, Shun ; Guy, Robert D ; del Álamo, Juan C. 2015. The title of this paper is "Coordination of contractility, adhesion and flow in migrating *Physarum* amoebae". The dissertation author was the co-first author of this paper.

Chapter 4

Self-organized mechano-chemical dynamics in amoeboid locomotion of *Physarum* fragments

4.1 Introduction

Amoeboid locomotion is a fast type of cellular locomotion that involves large shape changes mediated by cell contractility, and does not require biochemically regulated adhesion to the extracellular environment [3, 4, 20, 55]. In addition to its conspicuous biomedical applications, the study of amoeboid locomotion has been recently applied to the biomimetic design of fluid filled, highly deformable robots [22, 56]. Amoeboid organisms such as *Amoeba proteus* and *Physarum polycephalum* are particularly interesting model organisms for biomimetic design because they develop significant intracellular pressure-driven flows [57, 58]. Because diffusion across these giant cells is slow, intracellular flows are important not only to drive motility but also for the transport of chemical signals and nutrients (see §4.3.4 below and [59]). The non-linear feedback between pressure-driven flow, molecular transport and cell contractility can lead to rich dynamics that differ from those observed in smaller cells, and which are yet poorly understood.

This study examines the spatio-temporal dynamics of flow driven amoeboid locomotion in the true slime mold *Physarum polycephalum*. The *Physarum* plasmodium is a multi-nucleated slime mold that is composed of a gel-like ectoplasm and a sol-like endoplasm [60]. During locomotion, the endoplasm flows back and forth in a periodic manner, which

is customarily characterized as 'shuttle flow' [15, 57]. This flow is driven by periodic contractions of cross linked actomyosin fibrils in the ectoplasm [21, 61, 62]. The contraction is regulated by waves of calcium ions [16, 17], whose propagation is notably influenced by the endoplasmic flow [63, 64]. The interactions between these physical phenomena can be associated with the complex spatio-temporal patterns observed in a variety of *Physarum* preparations, including non-locomoting protoplasmic droplets, and locomoting plasmodial fragments of small ($\sim 100\,\mu$m) [21] and intermediate ($\sim 1\,\mu$m) size [65]. These experiments reported homologous spatio-temporal patterns for a range of different geometries, biological strains and environmental conditions, implying that the spatio-temporal coordination of motility in *Physarum* plasmodia could be achieved via remarkably robust physical mechanisms. However, investigating the details of these mechanisms has been difficult since the vast majority of previous experiments recorded a limited amount of data, namely the fragment thickness as estimated indirectly from image brightness. In particular, there is very limited information about the spatio-temporal dynamics of calcium ions and their relation with endoplasmic flow and ectoplasmic contractility [64].

Mathematical models facilitate the investigation of spatio-temporal coordination of *Physarum* motility by integrating the available experimental data into quantitative frameworks including variables that may be hard to measure experimentally. Various models have been constructed under this premise, and the numerical results have reproduced a variety of experimentally observed spatio-temporal patterns [21, 24, 46, 66]. However, these models have been so far limited to fixed simple geometries or have neglected key aspects of the mechano-chemical feedback present in locomoting *Physarum* fragments.

This paper presents novel multi-channel measurements of mechanical and chemical variables in plasmodial fragments of *Physarum polycephalum* undergoing directional migration. These measurements provide simultaneous spatio-temporal maps of the contractile forces generated by the fragments on their substratum, the velocities of their endoplasm and ectoplasm, and the distribution of free intracellular calcium concentration ($[Ca^{2+}]i$). The experimental data are analyzed to study how a biological system like *Physarum* coordinates the generation of mechanical forces with their shape changes and internal flows via adhesion to its substratum, and how these pressure driven flows transport the chemical signals that regulate force generation in the first place. The ultimate goal of the analysis is to understand how these phenomena are spontaneously organized to enable the directional flow driven locomotion of amoeboid organisms.

4.2 Methods

4.2.1 Preparation of *Physarum* fragments

Motile *Physarum* fragments of approximately 500 μm in length were prepared as in our previous study [21]. *Physarum* plasmodia were grown on 1% agar gel (Granulated; BD) using 150×15 mm culture plates (BD), fed with oat flakes (QUAKER) and kept in a dark humid environment at room temperature. Small portions of $\sim 0.2 \times 0.2$ mm^2 were cut from the parent plasmodia, transfered to collogen coated polyacrylamide (PA) gels embedded with fluorescent beads. A cap made of agarose was placed over the *Physarum* fragments immediately after. After several hours, the fragments adapted to tadpole like shape and perfomed directed migration, with noticeable intracellular streaming.

4.2.2 Gel Fabrication

Collagen-coated PA gels were prepared for traction force microscopy as previously described [28]. The gel was $\sim$ 1.5 mm thick and consisted of two layers, the top layer was thin ($\sim$ 10 μm) and contained 0.5 μm florescent beads (FluoSperes; Molecular Probes). The gels were fabricated using 5% acrylamide and 0.3% bisacrylamide (Fisher BioReagents), resulting in a Young's modulus value equals to 8.73 kPa [67]. The Poisson's ratio of the gel was measured to be 0.46 using the forces generated by the *Physarum* fragments themselves, following an elastographic traction force microscopy method recently developed by our group [29]. The cap, made of 0.8% agarose with thickness of 3 mm, prevented the PA gel from drying out and generate gentle confinement (a $\sim$ 30 Pa and a $\sim$ 1 KPa Young's modulus) to facilitate the measurement of intracellular flow. More details about the effect of the agar cap on our measurements and the migration of *Physarum* fragments can be found in [21, 29].

4.2.3 Microscopy

A Leica DMI 6000B inverted microscope and a PC running Micro-Manager software were used for image acquisition [30]. Time-lapse sequences were acquired at 16X in both bright-field and fluorescent-field. First, 10 images were acquired in the bright field at a frame rate of 5 Hz for flow quantification. Then, a 40-image fluorescence z-stack ($\Delta z = 1$ μm) was acquired over 10 sec for traction force microscopy. This 12-second acquisition cycle was repeated until the cell moved out of the field of view, providing quasi-simultaneous

recordings of intracellular streaming and traction stresses, given that the variables oscillate with a much longer period of ~ 100 sec [15].

4.2.4 Flow Quantification

The cytoplasm of *Physarum* amoebae is densely packed with intracellular vesicles, which were used as fiduciary markers to quantify the intracellular streaming velocity by particle image velocimetry (PIV) [15, 41]. The intracellular domain can be separated as endoplasmic flow phase and ectoplasmic gel phase with respective characteristic velocities of 10 μm/s and 0.15 μm/s. Different algorithms were used to determine the velocities range across 2 orders of magnitude. For $\vec{V}_{sol}$, we pre-process the raw image sequences using high-pass, band-pass and low-pass temporal filters as described in our previous paper [21]. Then we ran an in-house PIV algorithm on each filtered image sequences and asigned the velocity vector resulting from the sequences that maximizes the PIV signal-to-noise ratio at each point. As for $\vec{V}_{gel}$, we ran PIV on image pair consists of the first and last image in bright field of each acquisition cycle. The rather long time interval (1.8 second) allowed us to detect the low velocities of the ectoplasmic gel phase. Points with velocity lower than 0.2 μm/s were considered as ectoplasm. The PIV interrogation window size and spacing were respectively 32 and 8 pixels, yielding a spatial resolution of 6.5 μm.

4.2.5 Traction force microscopy

The $3D$ deformation of the PA substrate was measured at its top surface on which the *Physarum* amoebae were migrating as reported by del Álamo et al. [28]. Each instantaneous fluorescence z-stack was cross-correlated with a reference z-stack which was recorded at the end of experiment once the amoebae moved out of the field of view. Using these measurements as boundary conditions, we computed the three-dimensional deformation field in the whole polyacrylamide substrate by solving the elasto-static equation. We then compute the traction stress $\vec{\tau} = (\tau_{xz}, \tau_{yz}, \tau_{zz})$ exerted by the cell on the substrate using Fourier TFM methods described elsewhere [28, 31]. The spatial resolution of $\vec{\tau}$ was 13 μm in x,y and 1 μm in z.

4.2.6 Measurement of free calcium concentration

Single-wave length calcium indicators like Calcium Green-1 (Molecular Probes) exhibit an increase in fluorescence upon binding calcium ions and have been successfully applied to monitor the dynamics of $[Ca^{2+}]i$. However, the recorded intensity of these indicators can vary with other factors such as cell thickness. In our experiments, the local thickness of *Physarum* fragments can vary up to 50% during migration. Dual-wavelength ratiometric dyes, with distinct spectra of calcium free and calcium bond forms, can be used to minimize the effect of variation in cell thickness. However, dual-wavelength dyes require excitation in the UV range, for which *Physarum* fragments exhibit significant auto-fluorescence. To solve this problem, Texas Red (Molecular Probes), which is a calcium insensitive fluorescent dye, is co-injected into the sample together with Calcium Green-1. The ratio of fluorescent intensity between calcium sensitive dye and background dye are used to monitor the variation of $[Ca^{2+}]i$. Both dyes were dextran-conjugated and had a molecular weight of 10 kDa, which dramatically reduced leakage and compartmentalization compared to their non-conjugated forms. The dyes were coinjected into the parent mold under a Nikon SMZ-10 microscope using a PM 1000 cell micro-injection system (MicroData Instrument, Inc). Time-lapse sequences were acquired under 20X in bright-field, FITC and TRITC. 10 images in bright field were acquired first at 5 Hz for flow quantification, followed by one snapshot in FITC for Calcium Green-1 and another one in TRITC for Texas Red. This 5-second acquisition cycle was repeated for at least 10 minutes, allowing us to obtain a quasi-simultaneous quantification of intracellullar flow and $[Ca^{2+}]i$ during *Physarum* migration. Preliminary results obtained from this acquisition protocol were presented in [64].

4.2.7 Fragment shape statistics

Cell contours are extracted from bright-field microscopy time-lapse sequences as described previously [31]. Raw images are digitally thresholded, eroded and dilated in order to obtain a time-dependent scalar field $\Omega_c(t, x, y)$ containing ones inside the fragment and zeroes outside of it. The statistical distributions of fragment shape are determined from $\Omega_c(t, x, y)$ following the method outlined in ref. [68]. At each instant of time, $\Omega_c(t, x, y)$ is rotated so that the major axis of the fragment coincides with the x direction, and translated so that the origin $(x, y) = (0, 0)$ is set at the centroid of the fragment. The probability density function of a point belonging to the interior of the fragment in this reference frame

is calculated simply as

$$P(x,y) = \frac{1}{N_c}\sum_{i=1}^{N_c}\frac{1}{N_{t,i}}\sum_{j=1}^{N_{t,i}}\Omega_{c,i}(t_j,x,y), \tag{4.1}$$

where N_c is the number of cells and $N_{t,i}$ is the number of temporal observations corresponding to the i-th cell. According to this definition, the median cell shape is defined by the iso-contour $P(x,y) = 0.5$.

4.2.8 Kymographic representation

To facilitate the analysis of the spatio-temporal organization of endoplasmic flow, traction stresses, free intracellular calcium, etc., we generated kymographs for the quantities of interest. We followed the approach introduced by Bastounis *et al.*[14] for migrating amoeboid cells. At each instant of time (t) the major axis of cell is aligned vertically (x), and the measured quantity ($\mathbf{q}(t,x,y)$) is projected and the averaged over the cross section of the *Physarum* fragment, *i.e.*

$$\overline{q}(t,x) = \frac{\int \Omega_c(t,x,y)\mathbf{q}(t,x,y)\cdot\mathbf{u_x}\ \mathrm{d}y}{\int \Omega_c(t,x,y)\ \mathrm{d}y}, \tag{4.2}$$

where Ω_c denotes the interior of the *Physarum* fragment, and $\mathbf{u_x}$ is a unit vector oriented towards the fragment's front. Plotting two-dimensional maps of $\overline{q}$ produces kymographs that can reveal patterns of organization in the spatio-temporal dynamics of migrating *Physarum* fragments.

4.3 Results and Discussion

4.3.1 The spatio-temporal organization of endoplasmic flow and traction stresses reveals distinct dynamical modes in migrating *Physarum* fragments

A few hours after seeding the *Physarum* fragments on PA gel, we observed that fragments of diameter larger than ~ 100 μm performed persistent locomotion. Fragments larger than ~ 500 μm formed complex branched structures markedly different from an amoeboid

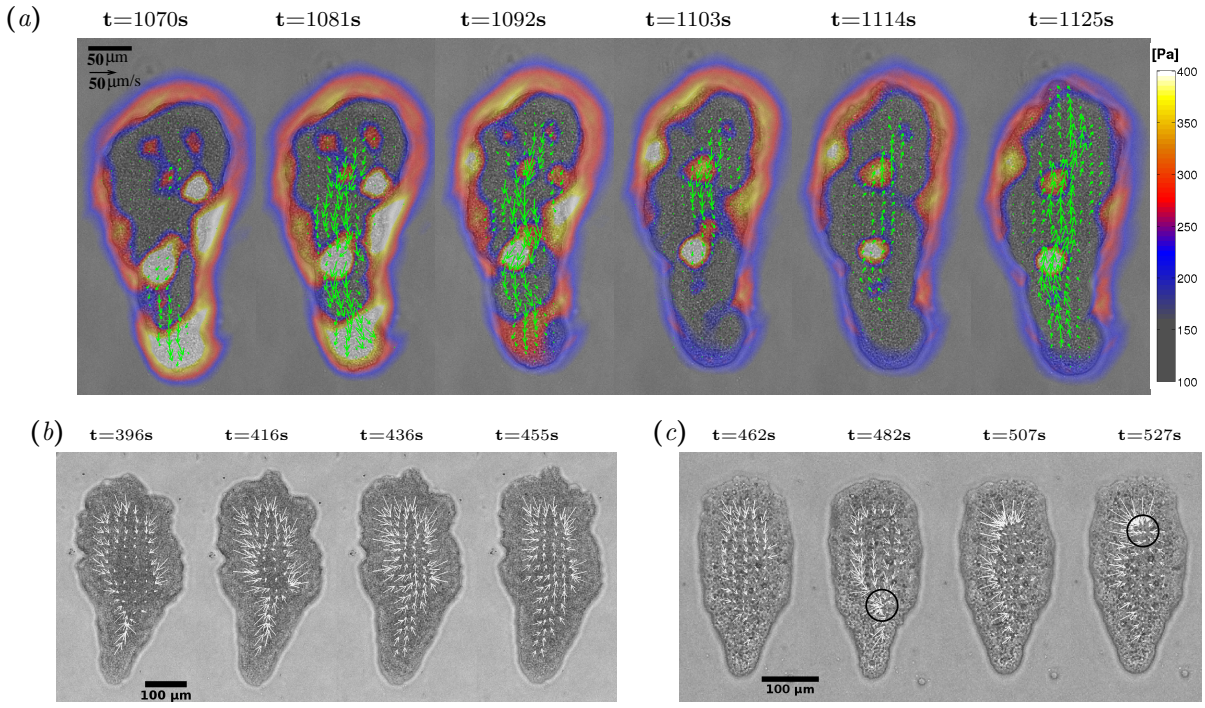

Figure 4.1: (a) Instantaneous endoplasmic flow speed and traction stresses exerted on the substrate by a migrating *Physarum* fragment. Arrows exhibit the flow speed and colormap shows the magnitude of traction stresses. (b, c) Instantaneous traction stresses exerted by two *Physarum* fragments with different dynamical behaviors, with the stress vectors along the cell boundary removed. Black circles indicate the location of contraction centers.

shape, and were not considered in this study. We focused our investigation on fragments of size ~ 300 μm, which generally adopted a tadpole-like shape, with a more rounded head and a tapering tail.

Directional locomotion of *Physarum* fragments requires the spatio-temporal coordination of endoplasmic flows and traction stresses exerted on a contact surface [21]. Most of the fragments analyzed in this study developed organized endoplasmic flows that oscillated between forward and backward motion with a well defined periodicity (Figure 4.1a). The traction stresses exerted by these locomoting fragments oscillated with a similar period, all the time showing an inward contractile pattern with larger stresses along the cell periphery. This pattern has been proposed to be analogous to a surface tension [62, 69], and has been recently linked to the cortical F-actin filaments and their cross-linkers in *Dictyostelium* amoebae [13]. Removing the stress vectors near each fragment's boundary renders the traction stress generated under the fragment's body easier to analyze, and unmasks waves of contraction with distinct spatio-temporal dynamics (Figure 4.1b, c).

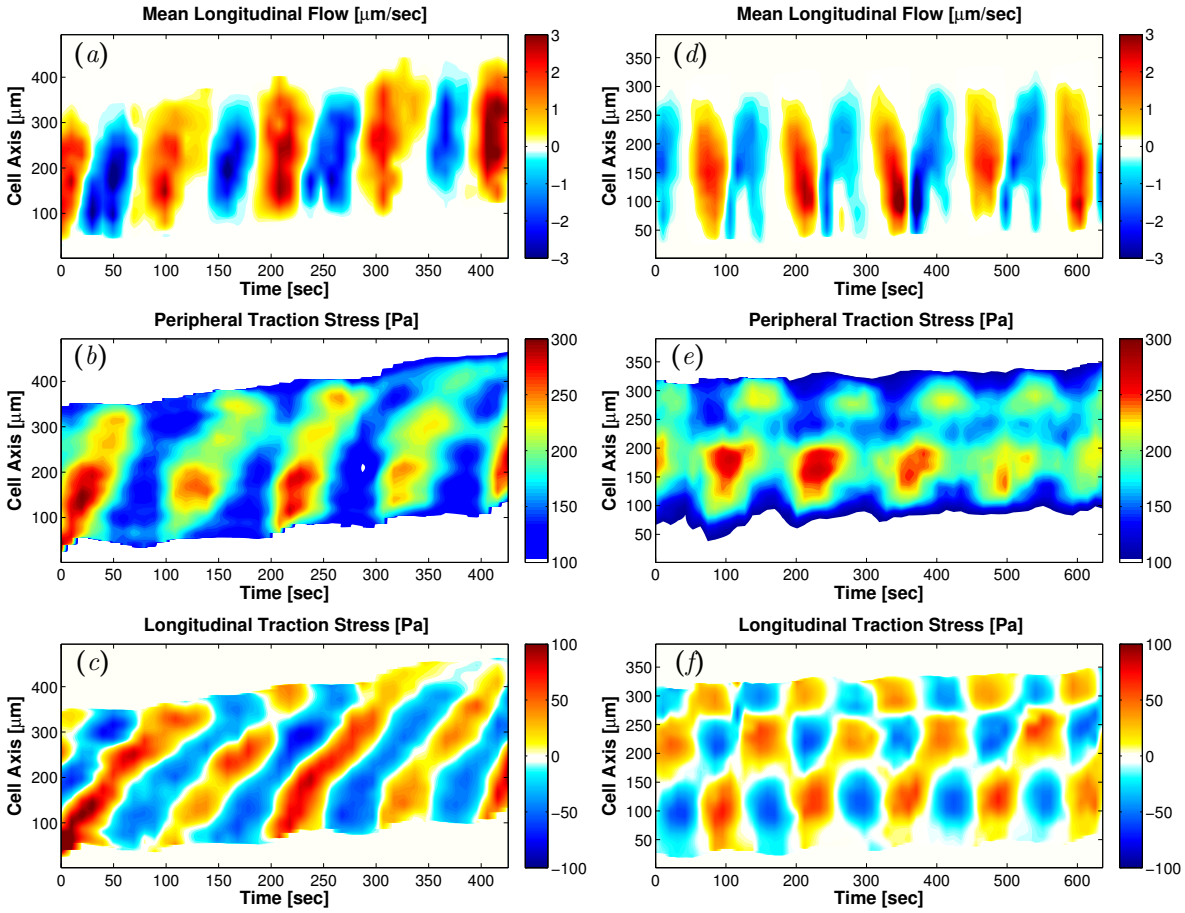

Figure 4.2: Kymographs of longitudinal endoplasm flow velocity (*a*, *d*), peripheral traction stress (*b*, *e*), and longitudinal traction stress (*c*, *f*) for a peristaltic (*a*– *c*) and an amphistaltic (*d*– *f*) *Physarum* fragment.

The most common organized pattern consisted of traveling waves that propagated forward along the center line of the motile fragment (Figure 4.2*a*–*c*). We labeled this migration mode as *peristaltic* because their motion was driven by forward traveling waves of contraction and relaxation (Figures 4.1*b* and 4.2*b*,*c*). This terminology is based on previous studies of *Physarum* migration [15, 60, 70], in which peristaltic fragments were designated by analyzing the dynamics of fragment width change rather than their force generation dynamics. In *Physarum* fragments undergoing peristaltic locomotion, both the forward and backward endoplasmic flow waves are generated from the tail and propagate forward in an approximately linear fashion. This mode has drawn more attention in previous studies because it occurs more often and leads to faster migration than other modes [15, 21, 57, 71]. However, it is not the only migration mode of *Physarum* locomotion with organized spatio-temporal dynamics.

We also observed a less frequent yet distinct mode of locomotion in which the head and tail contracted and relaxed in an anti-phase manner, and which we named the *amphistaltic* mode. This mode sustains waves of forward and backward endoplasmic flow that alternate periodically, similar to the peristaltic mode. However, in *Physarum* fragments undergoing amphistaltic locomotion, the waves of forward endoplasmic flow originate at the fragment's front and propagates backward, whereas the waves of backward flow originate at the fragment's back and travel forward. This dynamics leads to evident 'V'-shaped patterns in the flow kymograph (Figure 4.2*d*). The instantaneous spatial patterns of traction stresses in amphistaltic *Physarum* fragments showed inward contraction similar to peristaltic ones (Figure 4.1*c*). However, the traction stress kymographs revealed remarkable differences in their spatio-temporal dynamics. Instead of traveling waves, amphistaltic fragments sustained standing waves of traction stress with alternating peaks and valleys at the front and rear of the fragment (Figure 4.2*e*, *f*). Consistently, traction stress snapshots of amphistaltic fragments show localized contraction centers in the front and rear part of the fragment (black circles in Figure 4.1*c*). This pattern of contraction resembles that of the *Physarum* "dumbbells" previously described by others [38, 42, 62, 72]. These dumbbells form two thick round heads connected by a tube that contract alternatively while the fragment stays in place. We also observed a few contractile dumbbells in our experiments. However, the amphistaltic *Physarum* fragments reported here always adopted a tadpole-like shape and were able to move persistently.

Out of the 40 fragments in our study, 20 exhibited peristaltic behavior, 8 were amphistaltic, and 2 alternated between peristaltic and amphistaltic. In addition, 5 fragments had organized spatio-temporal dynamics that did not match either the peristaltic or amphistaltic patterns, and 5 more fragments had disorganized dynamics. Once a *Physarum* fragment began migrating either by the peristaltic or by the amphistaltic mode, the fragment would sustain the same mode for the duration of the whole experiment, *i.e.* $\gtrsim 30$ mins $\gtrsim 20$ cycles. Thus, the spatio-temporal dynamics of migrating *Physarum* fragments appear to settle into relatively robust oscillatory behaviors. This observation generally agrees with Rodiek *et al.*[65], who measured the height oscillations of ~ 1 mm–long *Physarum* fragments while they were migrating freely without being constrained by an agarose cap. These authors reported two spatio-temporal patterns in their measurements that resemble the peristaltic and amphistaltic behaviors found in our experiments: traveling waves that propagated at $\sim 5\mu$m/s, and standing waves with multiple spatial nodes separated

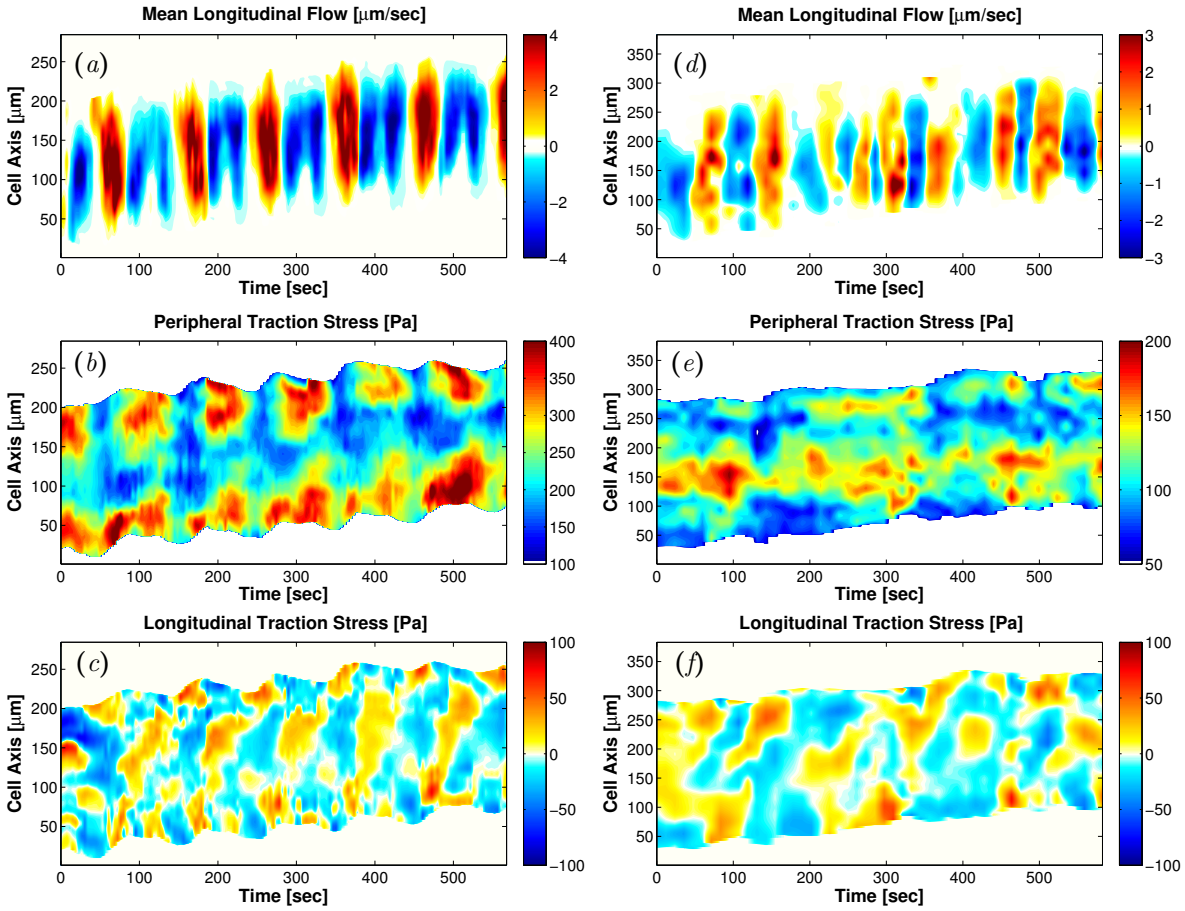

Figure 4.3: Kymographs of flow and traction stress of two *Physarum* that exhibited uncommon spatio-temporal dynamics. (*a*, *b*, *c*) Kymographs for a fragment exhibiting organized dynamics with two consecutive backward flow waves for each forward flow wave (reminiscent of a period doubling state). (*d*, *e*, *f*) Kymographs for a fragment exhibiting disorganized dynamics.

by wavelength of $\sim 100\,\mu$m with period of 10 minutes. We observed a few fragments that shifted spontaneously between the peristaltic and the amphistaltic mode while migrating, as well as other organized spatiotemporal patterns including 2-to-1 backward/forward flow waves (Figure 4.3*a*,*b*,*c*) and disorganized patterns (Figure 4.3*d*,*e*,*f*). This type of behavior is typical for systems with complex non-linear dynamics. Consistently, previous experimental studies on *Physarum* protoplasm droplets found traveling waves, standing waves, and chaos in local droplet thickness [73, 74]. In addition, recent mathematical models that include feedback between contraction, endoplasmic flow and calcium signaling in simplified non-migratory geometries have predicted a number of dynamical regimes depending on the level of mechano-chemical feedback and the rheological properties of the endoplasm [25, 66].

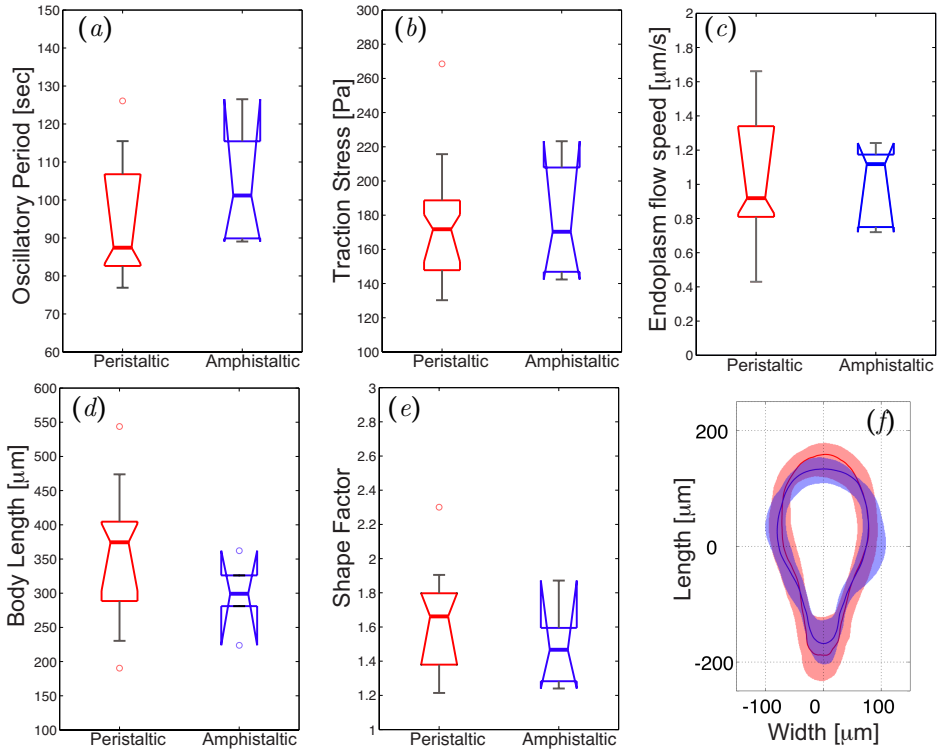

Figure 4.4: (*a*)–(*e*) Box plots of motility parameters corresponding to peristaltic ($N = 20$) and amphistaltic ($N = 8$) *Physarum* fragments. (*a*) Average oscillation period. (*b*) Average magnitude of the traction stresses. (*c*) Average endoplasmic flow speed. (*d*) Average fragment length. (*e*) Shape factor. (*f*) Average shape of peristaltic (red line) and amphistaltic (blue line) types. Shaded regions contain 90% of the statistical distribution of shapes for each fragment type.

In an attempt to find differences in the properties of peristaltic and amphistaltic *Physarum* fragments that could explain their distinct dynamics, we compared their oscillation period, average traction stress magnitudes and average endoplasmic flow speeds. However, we did not find any significant difference in these parameters between the two types of fragments (Figure 4.4*a*-*c*). Furthermore, both peristaltic and amphistaltic fragments adopted a similar tadpole-like shape during migration (Figure 4.4*f*). Rieu *et al.*previously reported that *Physarum* fragments with distinct dynamics of force generation can be differentiated by the number of membrane invaginations [62]. To quantify whether there were differences in the number of membrane invaginations of *Physarum* fragments undergoing peristaltic and amphistaltic locomotion, we measured the shape factor $S_f = P^2(4\pi A)^{-1}$, where P is each fragment's perimeter and A is its area. This parameter is unity for a perfect circle and increases as the number of lobes and invaginations in the perimeter of the fragment increases.

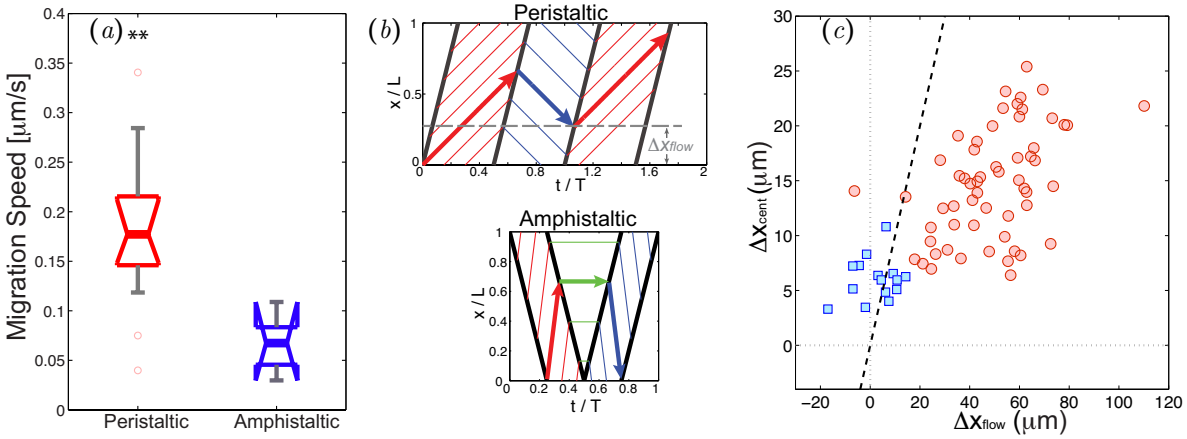

Figure 4.5: (a) Box plot of average migration speeds in peristaltic ($N = 20$) and amphistaltic ($N = 8$) *Physarum* fragments. Two asterisks denote statistically significant differences between medians ($p < 0.01$). (b) Simplified model schematic for the distance traveled by endoplasmic fluid particles per oscillation cycle. Top panel, peristaltic fragments; bottom panel, amphistaltic fragments. (c) Scatter plot of the distance Δx_{cent} traveled by the centroid of the *Physarum* fragment per oscillation cycle vs. the net distance Δx_{flow} traveled by an endoplasmic fluid particle. ●, peristaltic fragments; ■, amphistaltic fragments. The dashed line is $\Delta x_{cent} = \Delta x_{flow}$.

No significant difference was found between the two types of fragments (Figure 4.4e). Ongoing measurements of the endoplasmic rheological properties [75] should clarify if these properties play an important role in establishing the spatio-temporal dynamical state of migrating *Physarum* fragments, as predicted by some mathematical models [25, 66]. Despite these similarities, the average migration speeds of peristaltic and amphistaltic fragments were significantly different, as shown in the next section.

4.3.2 The spatiotemporal dynamics of endoplasmic and ectoplasmic flows affect the migration speed of *Physarum* fragments

We found that *Physarum* fragments undergoing peristaltic migration were in average $\sim$ 3 times faster than those undergoing amphistaltic migration (Figure 4.5a). This difference in locomotion speed is particularly remarkable considering that both peristaltic and amphistaltic fragments have similar sizes and shapes, and that their traction stresses and internal flow speeds have similar magnitudes and oscillation periods (Figure 4.5). A possible explanation can be found by noting the different asymmetries in the motion of endoplasmic fluid particles that arise from the different spatio-temporal dynamics of flow

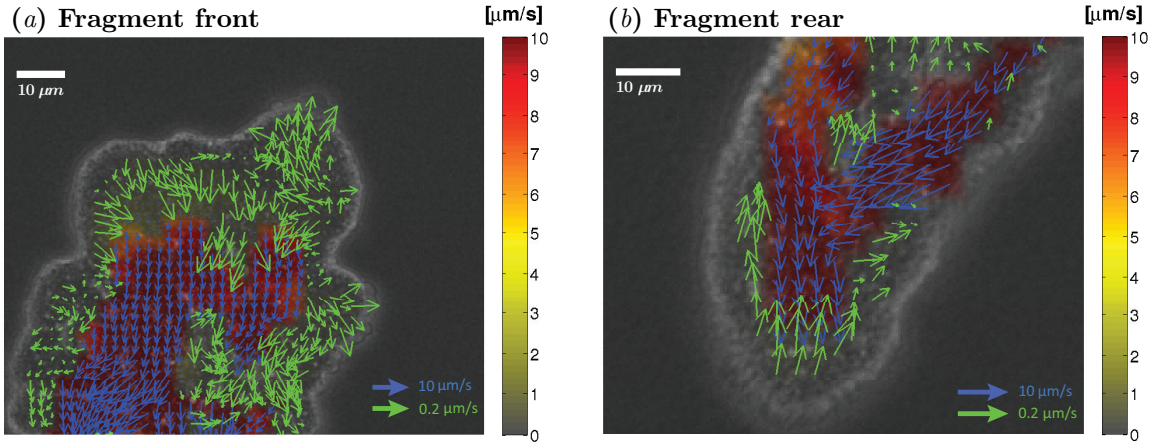

Figure 4.6: Instantaneous snapshots showing velocity vectors for endoplasm (blue) and ectoplasm (green) flows in a migrating *Physarum* , superimposed on the bright field image of the fragment. The pseudo-color map indicates the magnitude of velocity according to the colorbar in the right hand side of the panel. (a) Frontal part of the fragment. (b) Rear part of the fragment.

waves in each locomotion mode. Figure 4.5 presents this idea by plotting spatio-temporal particle trajectories in a simplified model in which the endoplasmic flow has constant speed and waves propagate forward and backward with constant wave speeds along the *Physarum* fragment. In peristaltic fragments, Matsumoto *et al.*[15] noted that fluid particles spend longer times traveling forward than backward, yielding net forward displacement every cycle period ($\Delta x_{flow} > 0$, Figure 4.5c). Extending this argument to amphistaltic *Physarum* fragments predicts that fluid particles approximately return to their original location at the end of each period (Figure 4.5c). Consistent with this reasoning, a scatter plot of the net forward motion of the centroid of a fragment (Δx_{cent}) vs. Δx_{flow} clearly segregates the amphistaltic and peristaltic locomotion modes (Figure 4.5b).

It should be noted that the flow kinematics argument hold as long as the *Physarum* fragments do not experience shape changes over time scales longer than their ~ 100 s oscillation period. This could explain Rodiek's *et al.*[65] observation that unconstrained *Physarum* fragments that sustain traveling waves in their height advance their front slower than fragments that sustain multi-nodal standing waves, because their fragments undergo substantial elongation and flattening during the duration of the experiment. In our experiments, this secular thickness variations are constrained by agarose cap placed on top of the sample.

While it provides a plausible explanation for the major differences in migration speed found between peristaltic and amphistaltic fragments, the flow kinematics hypothesis also

poses a paradox because it predicts that amphistaltic fragments should not be able to migrate. Furthermore, we previously used mathematical modeling to show that the asymmetry of endoplasmic flow velocity alone cannot determine the migration speed of migrating *Physarum* fragments [21]. The data in figure 4.5(b), which shows that Δx_{cent} is significantly lower than Δx_{flow}, agrees with this idea. *Physarum* plasmodia are often conceptualized as being composed of a two-phase fluid in which the sol and gel phases respectively represent the endoplasm and the ectoplasm. Therefore, it is reasonable to expect that the dynamics of the ectoplasm may contribute to the net migration speed of the plasmodium.

We still know little about the dynamics of the ectoplasm because its motion is significantly slower and harder to measure than that of the endoplasm. In this study, we expanded the image processing algorithm for the quantification of intracellular flow [21], in order to measure the flow velocity of the ectoplasm in addition to that of the endoplasm (see §4.2 and Figure 4.6).

Ectoplasm velocity is organized spatio-temporally in the form of traveling waves and standing waves in peristaltic and amphistaltic fragments respectively (Figure 4.7a,d), consistent with the dynamics of the traction stresses generated by the fragments (Figure 4.7b,e) and their endoplasm flow velocity (Figure 4.7c,f). However, in both types of fragments the ectoplasm velocity is asymmetric reaching substantially higher values during forward motion than during backward motion, particularly in the rear. These results suggest that the dynamics of the ectoplasm also contribute to the net motion of *Physarum* fragments.

4.3.3 Dynamics of substratum adhesion experience smooth slip-stick transitions

Inspection of Figure 4.7 suggests that traction stresses generation is closely related to the motion of the ectoplasm over the substratum, which is sound considering that the ectoplasm forms a cortical layer directly in contact with the plasmodial membrane. We explored this relationship in more detail in order to gain insight about the regulation of substratum adhesion in migrating *Physarum* fragments, which is not well understood since integrin-like adhesion proteins have not been identified yet for this organism.

We plotted the time evolution of the ectoplasm speed together with that of the traction stresses at the front of a fragment (Figure 4.8a), and with the phase difference between these two variables. The time lag between the two signals was calculated by maximizing their

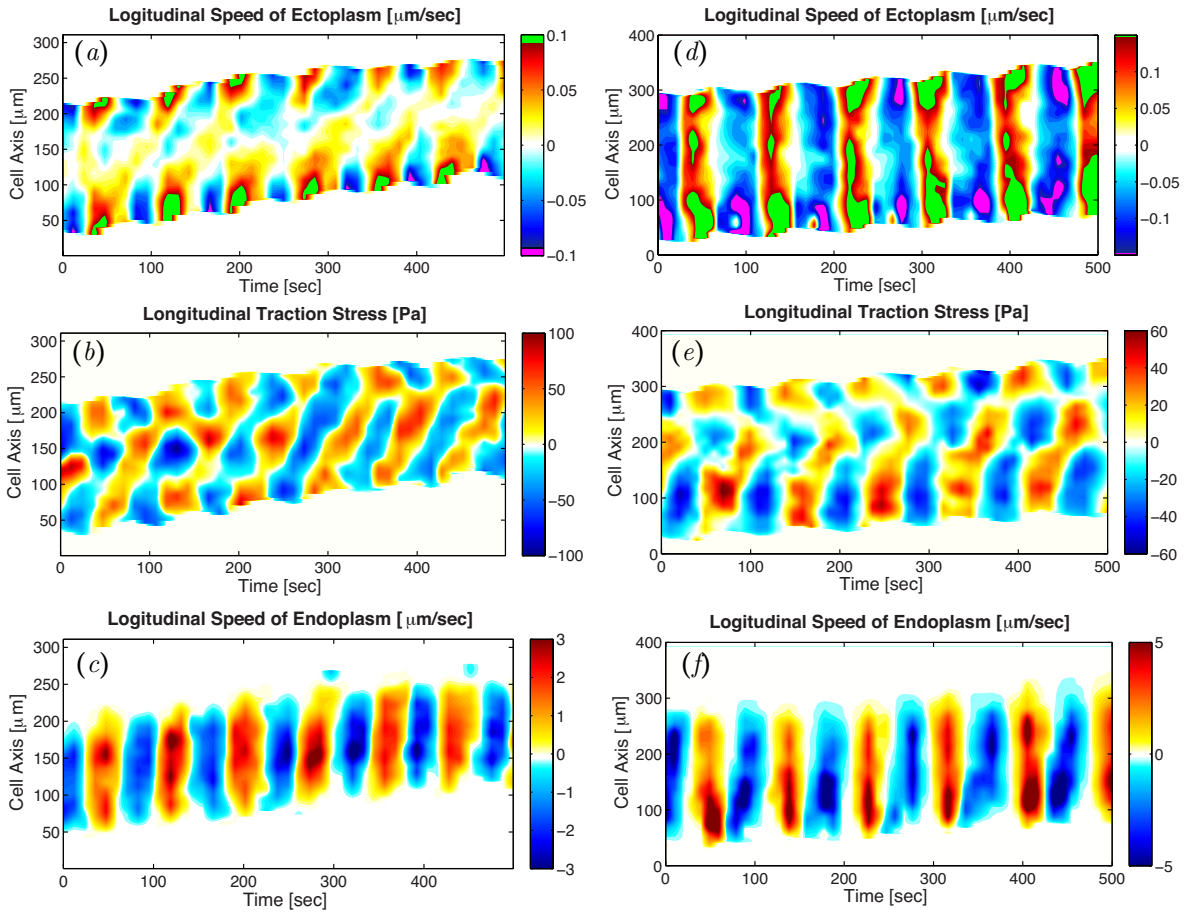

Figure 4.7: Kymographs of longitudinal ectoplasm flow velocity (*a*, *d*), longitudinal traction stress (*b*, *e*), and longitudinal endoplasm flow velocity (*c*, *f*) for a peristaltic (*a*–*c*) and an amphistaltic (*d*–*f*) *Physarum* fragment. In panels (*a*, *d*), we have added bright green and purple at the floor and ceiling of the colormaps to emphasize asymmetries in the velocity data.

cross-correlation over interrogation windows of 95 seconds and 50% overlap. The instantaneous phase difference was then obtained as the ratio of time lag and the averaged oscillation period (83 seconds). This analysis revealed that the traction stresses and ectoplasm velocity oscillate in phase for the most part. This result suggest that adhesion in this region follows the viscous-like regime $\tau = \xi v$ where τ is the adhesion stress, v the ectoplasm velocity and ξ is a friction factor. This result is in agreement with theoretical studies describing biological friction as the consequence of the thermally driven formation and rupture of molecular bonds [49].

In contrast to our observations at the front of the fragments, the time evolutions of ectoplasm speed and traction stresses have a complex relationship at the rear, alternating

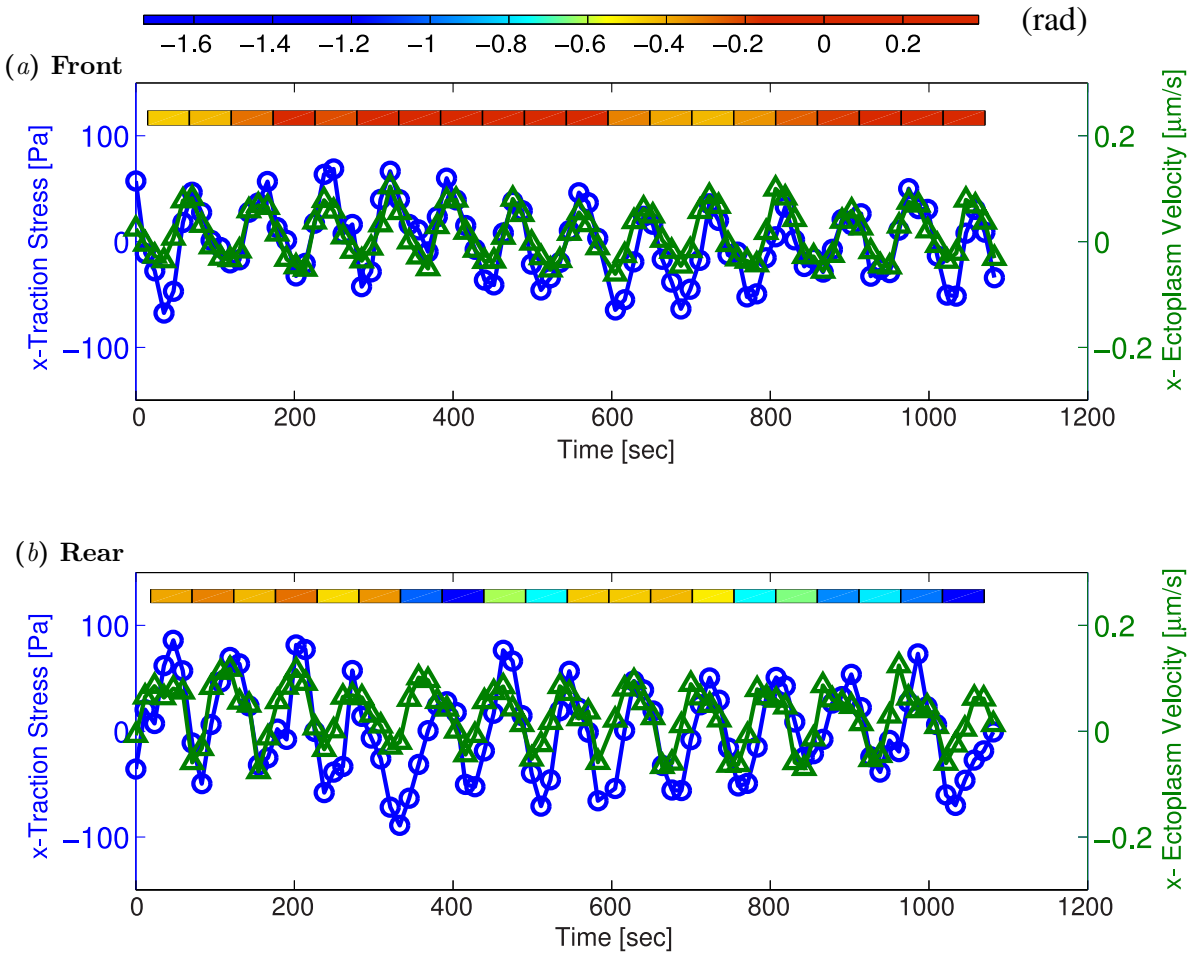

Figure 4.8: Time histories of longitudinal ectoplasm velocity (—△—) and longitudinal traction stresses (—○—) at two specific locations in the front (panel *a*) and the back (panel *b*) of the peristaltic *Physarum* fragment shown in Figure 4.7. The tiled bars at the top of the plots represent the time-dependent phase differences (in radians) between the ectoplasm velocity and the traction stresses. Blue and orange tiles represent phase differences near $-\pi/2$ (cell and substrate stick) and zero (cell and substrate slip) respectively, as indicated by the color scale at the top of the figure.

intervals at which they oscillate in phase with intervals in which the ectoplasm velocity precedes the traction stresses by approximately 1/4 of an oscillation period. Since a time integration of endoplasm velocity (*i.e.* endoplasm displacement) would generate the same phase difference of 1/4 period, we interpret this result as indicative of the occurrence of stick-slip transitions at the rear of *Physarum* fragments. Slip-stick transitions occur when ξ has a non-monotonic dependence with the ectoplasm velocity, which is a common behavior in biological friction [49]. This type of transitions have been linked to the dramatic shape oscillations experienced by cells such as keratocytes when crawling on flat substrata [76],

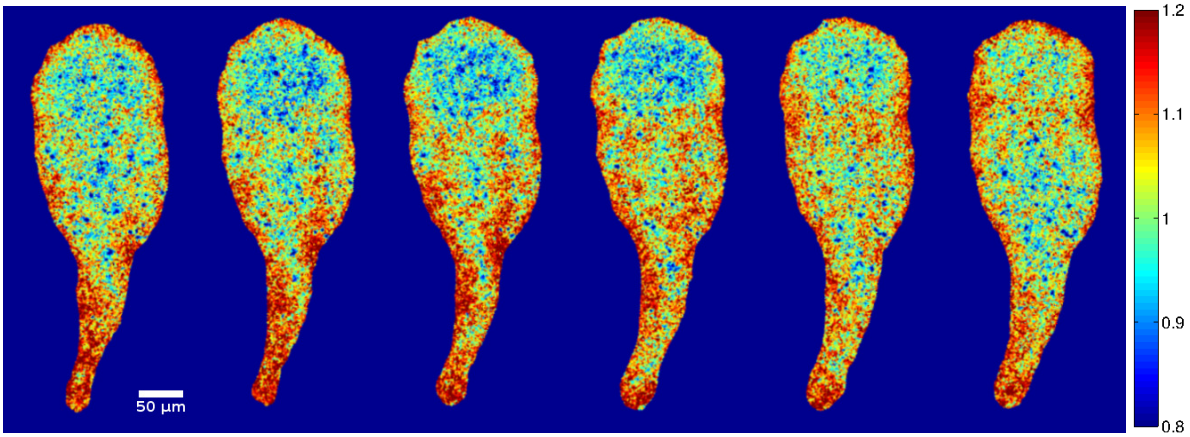

Figure 4.9: Time sequence of ratiometric measurememt of [Ca^{2+}]i during the locomotion of a typical peristaltic cell showing a Ca^{2+} wave propagating forward.

and it has been proposed that the frequency of these oscillations correlates with the speed of cell crawling [31, 68, 76, 77]. In the present experiments, we did not observe sharp changes in traction stress, ectoplasm speed or fragment length occurring at the stick-slip transitions, suggesting that these transitions are mild in migrating *Physarum* fragments. We analyzed kymographs of the phase difference between the time evolutions of traction stress and ectoplasm speed (not shown). While these data were somewhat noisy, they suggested that periodic stick-slip transitions propagate from the rear to the front of peristaltic fragments, while a standing stick-slip transition seems to form near the front of amphistaltic fragments. The dynamics of these transitions could provide a mechanism for *Physarum* to regulate the strength of their substrate adhesion in a way that supports asymmetry in the motion of the ectoplasm. However, additional experiments and further analysis are needed to confirm these ideas.

4.3.4 Dynamics of free intracellular calcium

The transport of calcium ions in *Physarum* fragments occurs in a complex regime that likely couples convection, diffusion and a time-dependent geometry caused by fluid-structure interactions at the fragment's lengthscale. Using reported values of cytoplasmic Ca^{2+} diffusivity, $D = 5.3 \times 10^{-10} m^2/s$ [78], and our measurement of intracellular flow speed $v \sim 5\mu m/s$, we estimate that characteristic timescales for Ca^{2+} diffusion and convection over a cell length ($l \sim 100\mu m$) are the same, $t_D = t_C = 20s$. Furthermore, this transport timescale is similar to the period of cellular shape changes ($T \approx 100s$) observed in our

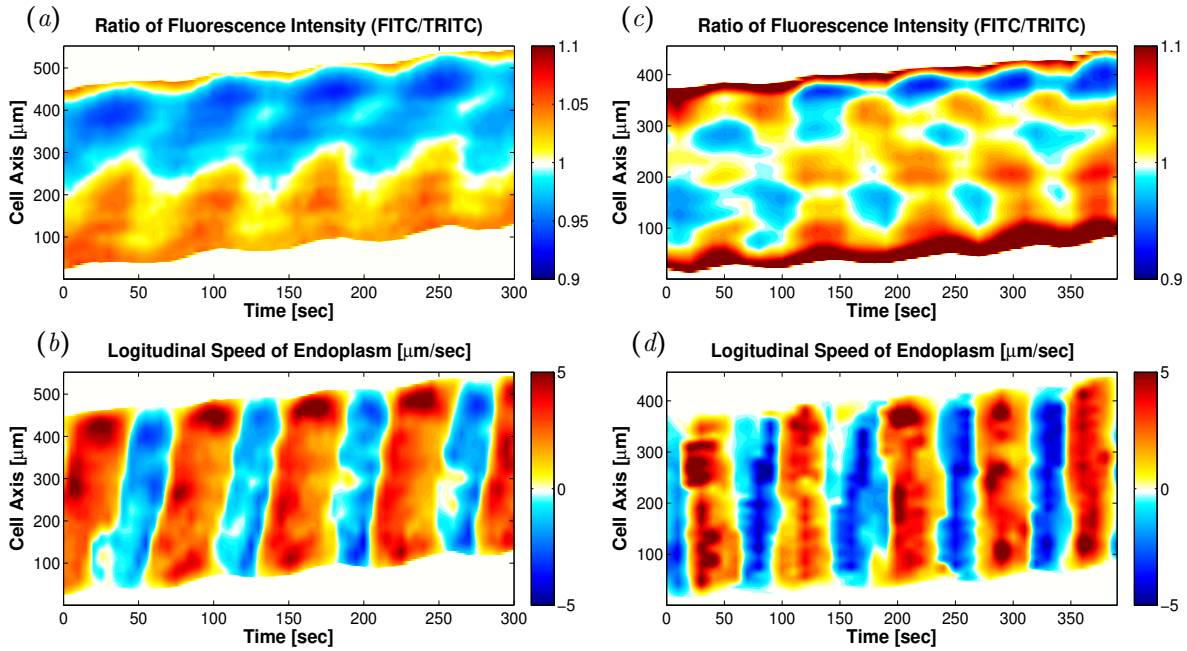

Figure 4.10: (*a*) Kymograph of ratiometric measurement of $[Ca^{2+}]$i in a typical peristaltic fragment. (*b*) Kymograph of instantaneous longitudinal velocities of endoplasmic flow of the same peristaltic fragment in Figure 4.10(*a*). (*c*) Kymograph of ratiometric measurement of $[Ca^{2+}]$i in a typical amphistaltic fragment. (*d*) Kymograph of instantaneous longitudinal velocities of endoplasmic flow of the same amphistaltic fragment in Figure 4.10(*c*).

experiments.

In order to study the relation between endoplasmic flow and the distribution of free intracellular calcium, we performed ratiometric measurements of free ion concentration, $[Ca^{2+}]$i, jointly with intracellular flow. Figure 4.9 shows a time sequence of $[Ca^{2+}]$i throughout one oscillation cycle of a typical peristaltic cell. Although this type of measurement is inherently noisy, it is possible to discern waves of high calcium concentration propagating from the rear to the front of the *Physarum* fragment. The spatio-temporal dynamics of these waves are clearly observed when $[Ca^{2+}]$i is represented in kymographic form. Figure 4.10 shows kymographs of $[Ca^{2+}]$i and intracellular flow that are representative of the peristaltic and amphistaltic migration modes.

Both for the peristaltic and amphistaltic modes, the spatio-temporal patterns of calcium concentration are consistent with the dynamics of the traction stress, endoplasmic flow and ectoplasmic motion. In *Physarum* fragments undergoing peristaltic migration, we found waves of $[Ca^{2+}]$i that traveled from the rear to the front of the fragment (Figure 4.10*a*), whereas patterns of $[Ca^{2+}]$i standing waves were observed for *Physarum* fragments under-

going amphistaltic locomotion (Figure 4.10*c*). The phase speed of the traveling waves was found to agree well with the measured endoplasmic flow velocity, $v_0 \approx 5\,\mu m/s$, suggesting that endoplasmic flows may be important in sustaining the dynamics of $[Ca^{2+}]$i transport.

To test this hypothesis, we considered a simple 1-D model for the transport of a passive scalar in non-dimensional form,

$$\mathrm{St}\,\partial_t c + v_{endo}\partial_x c = \mathrm{Pe}^{-1}\partial_{xx} c \tag{4.3}$$

where v_{endo} is a prescribed velocity normalized with v_0, the spatial variable $x\,\epsilon[0,1]$ is normalized with the fragment length L, and the time variable t is normalized with the period of the flow oscillations T. The two non-dimensional parameters in this equation are the Strouhal number $\mathrm{St} = L/(v_0 T)$ and the Péclet number $\mathrm{Pe} = Lv_0/D$, both of which have values of order unity in migrating *Physarum* fragments according to our experimental measurements and [78]. The solution to this transport equation exhibits traveling waves of passive scalar when v_{endo} is set to mimic our experimental measurements for peristaltic fragments, *e.g.* $v_{endo} = \sin[2\pi(x - \zeta t)]$ where the non-dimensional phase velocity $\zeta \approx 5$ (Figure 4.11*a*–*b*). Likewise, this simple model generates standing waves of passive scalar when the endoplasmic velocity is set to mimic our measurements for amphistaltic fragments (Figure 4.11*c*–*d*). Qualitatively, these results are robust with respect to changes in the parameter values, and in the boundary conditions (e.g. Neumann vs. Dirichlet) and initial conditions. For instance, the passive scalar in Figure 4.11 evolves from random initial conditions into temporally periodic pattern in about one oscillation cycle.

It is evident that a flow-transport-only model for the dynamics of intracellular calcium does not capture many of the quantitative features observed in our measurements of Figure 4.10. It is also evident that such a simplistic model neglects potentially relevant phenomena such as chemical kinetics of phosphorylation/dephosphorylation of the myosin light chain, Ca^{2+} influx through various calcium channels on plasma membrane, Ca^{2+} release from the sarcoplasmic reticulum and endoplasmic reticulum through IP_3 channels, etc [79–84]. Nevertheless, the ability of such a simple model to generate traveling waves and standing waves of a passive scalar highlight the importance of endoplasmic flow in the self-organization of dynamical patterns in migrating *Physarum* fragments.

The molecular regulation of acto-myosin contractility by calcium should be the same for *Physarum* fragments following the peristaltic and amphistaltic migration modes, given

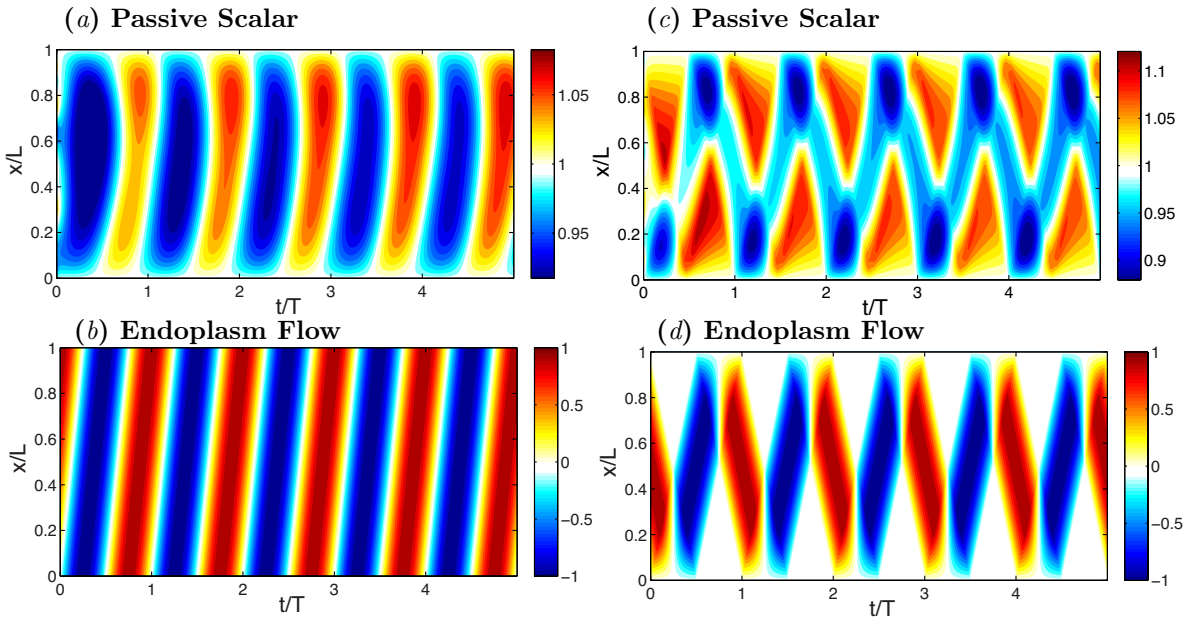

Figure 4.11: (a) Kymograph of concentration of passive scalar in a mimic peristaltic fragment. (b) Kymograph of longitudinal velocities of endoplasmic flow representative of a peristaltic fragment. (c) Kymograph of concentration of passive scalar in a mimic amphistaltic fragment. (d) Kymograph of longitudinal velocities of endoplasmic flow of endoplasmic flow representative of an amphistaltic fragment.

that we prepared all the fragments using the same protocol and the emergence of these modes was spontaneous. Thus, we hypothesized that the phase coordination between the dynamics of calcium and contractility waves would be the same for both migratory modes. While it was not possible to measure $[Ca^{2+}]i$ and traction stresses simultaneously in our experiments, we measured both $[Ca^{2+}]i$ jointly with endoplasmic flow, and traction stresses jointly with endoplasmic flow. The flow data were then used as reference to temporally align the oscillations of $[Ca^{2+}]i$ and traction stress for *Physarum* fragments following the same migration mode. We plotted time profiles at specific locations at the front and rear of each fragment (Figure 4.12), and juxtaposed the time evolution of endoplasmic flow velocity to that of $[Ca^{2+}]i$ or traction stresses (Figure 4.12).

For the peristaltic migration mode, the time evolutions of endoplasmic flow and $[Ca^{2+}]i$ were found to have opposite phases at the front of the *Physarum* fragment (Figure 4.12*a*). The time evolutions of endoplasmic flow and traction stress also had opposite phases at the fragment front (Figure 4.12*b*), implying that the oscillations in $[Ca^{2+}]i$ and traction stress were in phase. The same relationship between $[Ca^{2+}]i$, endoplasmic flow and the traction stresses can be deduced from the time profiles of these variables recorded at the

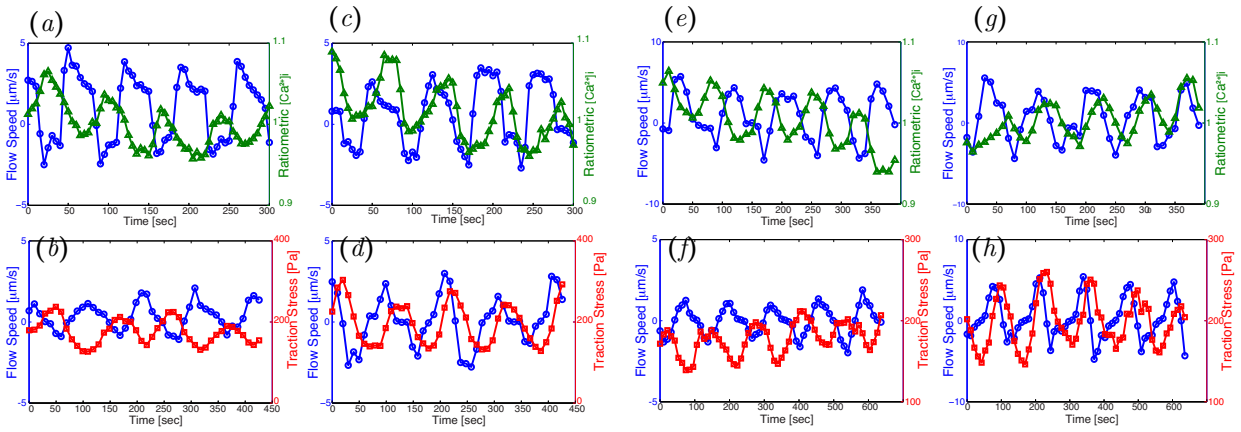

Figure 4.12: Top row (*a*, *c*, *e*, *g*): Time histories of endoplasmic flow velocity (—○—) and ratiometric measurement of $[Ca^{2+}]$i (—△—), averaged along the width of a peristaltic fragment (panels *a* and *c*) and an amphistaltic fragment (panels *e* and *g*). Bottom row (*b*, *d*, *f*, *h*): Time histories of endoplasmic flow velocity (—○—) and peripheral traction stress (—□—), averaged along the width of a peristaltic fragment (panels *b* and *d*) and an amphistaltic fragment (panels *f* and *h*). Panels (*a*, *b*, *e*, *f*): Fragment front. Panels (*c*, *d*, *g*, *h*): Fragment rear.

rear of peristaltic *Physarum* fragments (Figure 4.12*c*, *d*). In amphistaltic fragments (Figure 4.12*e*–*h*), the phase coordination between the waves of $[Ca^{2+}]$i, flow speed and traction stress was the same as in peristaltic fragments. Our finding that the calcium concentration is in phase with traction stresses agrees with previous observations [63, 85, 86]. Yoshiyama *et al.*[63] interpreted this result as an indication that calcium inhibits acto-myosin contractility in *Physarum* because the maximum calcium concentration coincides with the onset of relaxation. However, the kinetics of the involved biochemical reactions could make this response more complicated [87].

4.4 Conclusion

The multi-nucleated slime mold *Physarum polychephalum* can be used to generate amoeboid-like motile cells by excision of $\sim$ 100 μm-long fragments from the parent mold. These fragments are formed by a cortical gel-like ectoplasm that surrounds a sol-like endoplasm. Periodic contractions of the ectoplasm drive shuttle flows in the endoplasm, which transport the nutrients and calcium ions necessary for contraction. The feedback among these processes can lead to rich spatio-temporal dynamics that significantly affect the migration behavior of *Physarum* fragments. However, our understanding of these dynamics is limited

by a lack of direct measurements of quantitative variables. This study provides detailed concurrent measurements of the spatio-temporal distribution of endoplasmic and ectoplasmic flow, contractile forces and $[Ca^{2+}]i$ in migrating fragments of *Physarum* plasmodia. To the best of our knowledge, this is the first experimental quantification of mechano-chemical dynamics in a model organism of flow-driven amoeboid migration.

The spatio-temporal patterns found in the measured quantities suggests that the mechano-chemical dynamics of these fragments can lead to a variety of both disorganized and organized states. We focused our attention on two particularly stable organized states associated with periodic oscillations in flow, contractile forces and $[Ca^{2+}]i$. In the most stable (*i.e.* frequently observed) state, the mechano-chemical dynamics of the fragment are organized in the form of traveling waves that propagate from the rear to the front of the fragment, in good agreement with the *peristaltic* behavior studied in previous works [15, 21]. We also investigated a second stable dynamical state that we termed *amphistaltic* because it consists of alternate anti-phase contractions and relaxations of the fragment's front and back (from $\alpha\mu\phi$ß in Greek meaning "on both sides"). These anti-phase contractions are associated with standing waves of traction stresses and $[Ca^{2+}]i$, but they lead to traveling waves of endoplasmic flow with alternating propagation directions; waves of forward flow propagate backward and viceversa, leading to clear V-shape patterns in spatio-temporal flow kymographs.

Our data suggest that the transport of calcium ions by the endoplasmic flows observed in *Physarum* fragments may be fundamental to coordinate the spatio-temporal patterns of traction stresses that drive their locomotion. Specifically, we showed that the forward traveling waves of endoplasmic flow found in peristaltic fragments can sustain traveling waves of calcium concentration, consistent with our experimental measurements of $[Ca^{2+}]i$. In a similar fashion, the flow waves of alternating propagation direction observed in amphistaltic fragments can sustain standing waves of $[Ca^{2+}]i$, also consistent with our experimental measurements. Furthermore, we showed that the patterns of concentration of calcium ions evolve in space and time with the same phase as those of the traction stresses.

Apart from the organization of their mechano-chemical dynamics, we did not observe significant differences between the properties of peristaltic and amphistaltic *Physarum* fragments. Both types of fragments were found to have similar sizes and shapes, and their traction stresses and internal flow speeds were found to have similar magnitudes and oscillation periods. Nevertheless, the average migration speed of peristaltic fragments was

measured to be 3 times higher than the migration speed of amphistaltic fragments. We argued that this difference could be caused in part by the spatio-temporal dynamics of the endoplasmic flows in the two types of fragments. In peristaltic fragments both positive and negative endoplasmic velocity waves propagate forward, which allows for positive net endoplasmic motion every oscillation cycle [15]. On the other hand, in amphistaltic fragments positive and negative velocity waves propagate in opposite directions, which leads to zero net endoplasm motion.

Albeit slowly, amphistaltic fragments undergo peristent directional migration over long periods of time. Thus, it is evident that analyzing the symmetry of endoplasm flow is not sufficient to capture the migratory behavior of *Physarum* fragments. In contrast to the endoplasm, we observed that the ectoplasm of both peristaltic and amphistaltic fragments flows faster forward than it does backward, leading to a significant amount of net motion per cycle. In a previous study [21], we used numerical modeling to illustrate that this type of asymmetry in ectoplasm motion would require tight coordination between the generation of contractile forces and the adhesion of the ectoplasm to the substratum. We explored this coordination by comparing the time evolutions of the traction stresses generated by the *Physarum* fragments and of the motion of their ectoplasm. Our experimental results suggest that the spatio-temporal coordination between these two quantities may be realized by means of stick-slip transitions. We occasionally observed stationary "hotspots" in the measured traction stresses (see *e.g.* Figure 4.1*a*), which might be associated with the stick-slip transitions observed at the fragment tail. These stationary adhesions are however more common in other types of amoeboid cells such as *Amoeba proteus* or *Dyctiostelium discoideum*. In both cell types, the adhesion sites remain stationary as the cells migrate over them, leaving a clear signature in the kymographs that consists of horizontal bands [13, 14]. This behavior significantly contrasts with the dynamics of the traction stresses observed in migrating *Physarum* fragments. Finally, our data provide preliminary evidence that these transitions might be organized in the form of traveling or standing waves, consistent with the dynamics of endoplasmic flow, contractility and calcium distribution. Further experiments and analyses are needed to confirm and expand this mechanistic model.

4.5 Acknowledgements

Chapter 4, in part, has been published in the *Journal of Physics D: Applied Physics*. Zhang, Shun ; Guy, Robert D ; Lasheras, Juan C ; del Álamo, Juan C. 2017. The title of this paper is "Self-organized mechano-chemical dynamics in amoeboid locomotion of *Physarum* fragments". The dissertation author was the primary author of this paper.

Chapter 5

Locomotor adaptability of the schistosome pathogen to changes in its physical environment: mechanical principles and implications for drug discovery

5.1 Introduction

Schistosomiasis is a 'neglected' infectious disease of the tropics that infects more than 240 million of the world's poorest people in Africa, South-East Asia and South America [88]. The three principal species of this flatworm infecting humans are *Schistosoma mansoi*, S. *haematobium* and S. *japonicum*. Mature flukes live in the venous blood system where they mate and produce eggs which eventually exit the body via the feces or urine, depending on species. Many eggs, however, become trapped in various internal tissues and organs, inducing chronic inflammation and fibrosis that manifest as pain, malaise and a decreased ability to attend school or perform manual labor. Given its morbidity, schistosomiasis is a focus of various (inter)national drug delivery campaigns to decrease prevalence and incidence.

Infection is established via free swimming larvae (cercariae) that are released from snail intermediate hosts. After penetration of the skin, the larvae ($\sim 200 \times 100$ μm) transform to schistosomula which traverse the lungs and eventually establish in the venous blood

system. Worms mature as males or females (each up to 1 cm long): maturation of the female depends on intimate contact with the male worm which enfolds the female in a specialized gynecophoral canal. Males are responsible for transporting the slender cylindrical females around the venous system for deposition of eggs.

Schistosomes are soft-bodied, acoelomate triploblastic metazoa that possess a complex muscular system made up of circular, oblique and longitudinal muscles intricately interlaced with a nervous system that utilizes both classical and peptidergic signaling systems [89]. This neuromuscular complexity results in a remarkable plasticity/pliancy in parasite shape and movement that are augmented by two anteriorly-placed oral and ventral suckers which, presumably, maintain the worm's position on the vein wall and aid in locomotion. S. *mansoni* is found throughout the hepatic portal and mesenteric veins, which possess marked transitions in vessel lumen diameter (D) and blood flow speed (v), ranging from $D > 1$ cm and $v \sim 30$ cm/s within the hepatic portal vein [90] to $D < 0.1$ mm and $v \sim 1$ mm/s within the mesenteric veins. Considering that the body diameter of a mature male worm is around 0.5 mm, it is conceivable that the suckers aid movement in larger veins whereas crawling and squeezing is employed in the more confined veins, however, locomotion by the adult has neither been formally investigated nor quantified. In organisms without extremities, crawling and squeezing typically rely on the exertion of periodic waves of shear stress (also known as traction stress) on the surrounding environment [9, 91–95]. Organisms relying on this mechanism of locomotion can control and modify the characteristics of these waves in order to adapt their migration to diverse properties of the surrounding environment, such as surface roughness, adhesiveness and confinement [9–11, 21, 44].

The mechanics underlying schistosome locomotion are unknown. Neither is it known whether and how the flatworm adapts its locomotion to the varying conditions of flow shear stress and physical confinement encountered in different parts of the hepatic portal and mesenteric venous systems. Specifically, how the pathogen organizes the traction stress generated by its suckers and body to achieve persistent locomotion is unknown. Nor is it clear whether the parasite employs crawling or squeezing when confined. Moreover, we do not understand whether the pathogen can engage muscle and sucker movement in a coordinated / synergistic manner. Understanding these activities, would complement recent insights into the physical organization of the pathogen's neuromuscular system. Further, given that the neuromuscular system of parasitic worms is a rich source of drug targets, being able to quantify and differentiate the action of experimental chemistries on schistosome locomotion,

including relative to the only drug available for treatment, praziquantel, would offer value in the discovery and development of new drugs.

In this study, we explored the mechanics of locomotion of the schistosome pathogen under physiologically relevant conditions using self-designed experimental setups and devices. We revealed, for the first time, that S. *mansoni* change the locomotion mechanisms when facing different physiologically relevant mechanical challenges. S. *mansoni* exclusively use their oral and ventral suckers generating forces to migrate in the environment without confinement around their body. When subjecting to flow of varying magnitude, S. *mansoni* actively adjust their grabbing strength via their suckers to remain attached to the substrate. However, S. *mansoni* switched to a completely different locomotion strategy when crawling through restrictive conditions by applying traveling waves of strong traction stress along the body. Strikingly, we discovered the sucker action and body contraction wave can be coordinated to achieve faster locomotion when migrating under restrictive environment.

5.2 Methods

5.2.1 Ethics statement

Maintenance and handling of small vertebrate animals were carried out in accordance with a protocol approved by the Institutional Animal Care and Use Committee (IACUC) of the University of California San Diego. UCSD-IACUC derives its authority for these activities from the United States Public Health Service (PHS) Policy on Humane Care and Use of Laboratory Animals, and the Animal Welfare Act and Regulations (AWAR).

5.2.2 Preparation of S. *mansoni*

The acquisition, preparation and in vitro maintenance of S. *mansoni* have been described. We employ a Puerto Rican isolate of S. mansoni that is cycled between Biomphalaria glabrata snails and female Golden Syrian hamsters (Simonsen Laboratories; infected at 4-6 weeks of age) as intermediate and definitive hosts, respectively. Briefly, adult worms are harvested from hamsters 42 days post-infection in RPMI or DMEM, and washed 5 times prior to maintenance overnight at 37 °C and 5 % CO_2 in Basch medium containing 4 % FBS, 500 μg/ml streptomycin and 500 U/ml penicillin.

5.2.3 Polyacrylamide Gel fabrication

Collagen-coated PA gels of 1.5 mm thickness were prepared for traction force microscopy as previously described [28]. The gels contained a thin top layer (10 μm) impregnated with 1 μmfluorescent beads (FluoSperes; molecular probes) that were used as fiduciary markers to track substrate deformation. Gels were fabricated using 5 % acrylamide and 0.3 % bisacrylamide (Fisher BioReagents), resulting in a Young's modulus of 8.73 kPa. The Poisson's ratio of the gel was measured to be 0.46, following an elastographic traction force microscopy method developed by our group [29]. Gels were activated with sulfo-SANPAH (Thermal Scientific) under UV light and coated with 0.15 mg/ml collagen I (Corning).

5.2.4 Flow Chamber Experiments

To carry out experiments with adult S. *mansoni* worms under flow conditions representative of their in vivo environment, a flow chamber device was fabricated. The device was assembled using 5 laser-cut acrylic sheets (labeled P1 - P5 in Figure 5.1B), with features tailored to create an inlet that sequentially leads to a reservoir, a rectangular test section that can house a polyacrylamide (PA) gel at its bottom, another reservoir and the outlet. Silicon grease was applied between each sheet to prevent leaking, and the whole setup was fastened by screws.

Prior to each experiment, the device was assembled and filled with the culture medium described above. Subsequently, a 1 mL pipette was used to gently introduce adult male S. *mansoni* worms into the device from the inlet. After that, the inlet was connected to a 60-ml syringe (BD) filled with culture medium. The syringe was then gently pushed to drive S. *mansoni* onto the PA gel. Then the whole system was placed on the stage of microscope for image acquisition (see below), with the syringe installed on a NE-4000 double syringe pump (Pump Systems Inc).

A flow rate of Q = 2.24 ml/min was applied after S. *mansoni* adhered to the PA substrate. Then the flow rate was increased in a stepwise manner to Q = 11.2, 56.1 and 100 ml/min, with each flow step lasting for at least 10 seconds. At each flow step, if a worm was able to adhere for at least 5 seconds, it was regarded as an adhering worm. The recording was stopped when the worm detached from the substrate or the maximum flow rate had been reached. We followed the exact solution of the velocity profile in a rectangular channel presented by Boussinesq [96] to calculate relevant flow properties from

Q and the chamber geometry, including the Reynolds number, maximum flow velocity, wall shear stress and pressure gradient (Table 5.1). The viscosity of culture medium was measured as $\mu = 8.54 \times 10^{-4}$ Pa·s at 37°C using particle tracking microrheology methods previously calibrated by us [97, 98].

The flow rates in our experiments were chosen to cover the physiologically relevant induced wall shear stress ranging from human vena cava to venules [99]. Among all vessels encountered by S. *mansoni*, the portal vein has the highest flow velocity. Thus a reference value for wall shear stress in the hepatic portal vein [90] was calculated by assuming a Poiseuille profile with maximum velocity of 30 cm/s in the center, vessel diameter of 1 cm and blood viscosity of blood = 2.73×10^{-3} Pa·s at 37 °C, resulting in $\tau_{wall} = 0.3275$ Pa. This value falls into the range of wall shear stress induced by the flow steps applied in our device.

Table 5.1: Calculated relevant flow properties with flow rate Q = 2.24, 11.2, 56.1 and 100 ml/min.

Flow rate (ml/min)	2.24	11.22	56.1	100
Wall shear stress (Pa)	0.0191	0.0955	0.4775	0.851
Max flow velocity (m/s)	0.0056	0.028	0.14	0.25
Reynold's number	3.28	16.39	81.95	146.1
Pressure gradient (Pa/m)	38.26	191.28	956.4	1704.8

5.2.5 Experiments in a confined environment

To mimic the physically restrictive environment encountered by S. *mansoni* in narrow veins, we sandwiched the worms between the polyacrylamide (PA) gel used for traction force microscopy (see below) and an agar cap (0.8 % agarose, 18 mm diameter and 1.5 mm thickness), as in our previous work [11, 21]. To generate varying levels of confinement, the cap is fabricated with a gap of different depths (see Figure 5.1C). The cap was soaked in culture medium for 30 minutes before the experiment, and was placed on top of the PA gel with S. *mansoni* immediately after transferring the worms. In this setup, the worms are sandwiched in a gap of either 100 or 300 μm, which, considering that the thickness of an adult male S. *mansoni* is ~ 500 μm, generated different levels of confinement on the worms. Nevertheless, the constraint was not severe enough to arrest the motion of the worms.

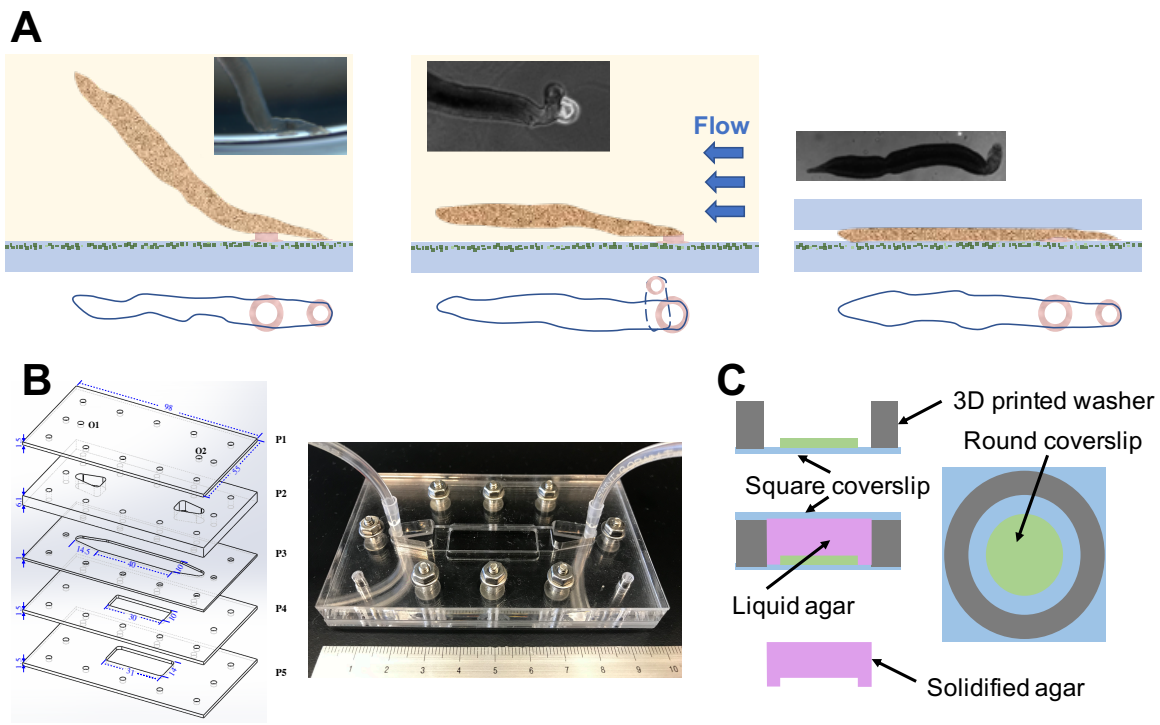

Figure 5.1: (**A**) Schematics of a free adhesive (sucker-based) locomotion (left), a worm adhering against flow (center), and a worm moving under confinement (right), with corresponding bright-field images (**A**1, lateral view; **A**2 and **A**3, dorsal views) captured during our experiments; VS and OS refer to the ventral and oral suckers, respectively. (**B**) Flow chamber design. The image to the left is a diagram of the device layer design, with all important dimensions indicated in mm. O1 and O2 are inlet and outlet orifices. The image to the right is a photograph of the assembled device. (**C**) Fabrication scheme of the agar caps system used to generate controlled confinement. A 3D printed PLA washer (grey) and a round coverslip (green) are glued on a square coverslip (blue). An agar solution (purple) is poured and covered with a square coverslip to flatten its surface while the solution solidifies. Varying the number of round coverslips controls the gap produced in the agar gel.

5.2.6 Microscopy

A Leica DMI 6000B inverted microscope controlled by a computer running Micro-Manager software was used for image acquisition [30]. All experiments were performed at 37 °C. Different acquisition protocols were followed for the various experiments reported here. The experiments performed under no confinement (including the flow chamber experiments) were imaged under 5X and at 1 frame per second (fps) in both bright and fluorescent fields. This field of view was sufficient to capture the oral and ventral suckers. Under confinement, we imaged at 2X in order to capture the traction stresses generated along the length of the body. In addition, we acquired time-lapse image sequences at 10 and 100 fps in bright field

only. The complete acquisition protocols are listed in table 5.2.

Table 5.2: Acquisition protocols followed in this study under various combinations of flow rate and constrains.

Experimental setup	Channel	Magnification	FPS	Purpose
No constrain, no flow	BF/FLUO	5X	1	Movement, traction stress under sucker
No constrain, with flow	BF/FLUO	5X	1	Traction stress under sucker
Constrain, no flow	BF/FLUO	2X	1	Movement and body wave, traction stress under body and sucker
Constrain, no flow	BF	2X	10	High temporal resolution of body wave and sucker coordination
constrain, no flow	BF	5X	100	Velocity of material points on the body

5.2.7 Traction Force Microscopy

The in-plane deformation of the top surface of the PA substrate by moving S. *mansoni* was measured by tracking the motion of the fluorescent beads as reported by del Álamo *et al.*[28]. Each instantaneous fluorescent image was cross-correlated with a reference image which was recorded at the end of experiment, after the worms had moved out of the field of view. Using these measurements as boundary conditions and assuming the deformation in z direction is 0, we solved the equation of mechanical equilibrium for the PA gel as previously described [28, 31]. Using this solution, we computed the deformation field in the whole polyacrylamide substrate, as well as the traction stress vector $\boldsymbol{\tau} = (\tau_{xz}, \tau_{yz})$ on its top surface. The spatial resolution was 20 μmand 50 μmunder 5X and 2X, respectively.

5.2.8 Kymograph Representation

We generated kymographs to analyze the spatio-temporal dynamics of S. *mansoni* locomotion. At each instant of time (t), the centerline of the worm's body is determined from bright field images. Then, the distance along the centerline from the tail is used as an independent variable together with time to create 2D representations by stacking together data from different time instants. In particular, we plot the spatiotemporal distributions of worm width $w(s,t)$, and longitudinal traction stress $\tau_s(s,t) = \boldsymbol{\tau_w}(s,t) \cdot \boldsymbol{e_s}(s,t)$, where $\boldsymbol{\tau_w}$ represents the local average of the traction stress across the worm's body width, and $\boldsymbol{e_s}$ is a unit vector parallel to the body's centerline.

5.3 Results

Using a custom-built apparatus, we measured the mechanics of S. *mansoni* locomotion in environments designed to replicate those encountered by the parasite *in vivo*. Figure 5.1A illustrates the three experimental designs employed, namely (i) free adhesive (sucker-based) locomotion, (ii) locomotion without confinement subjecting to directional flow and (iii) locomotion under two levels of environment (mild and severe).

5.3.1 The oral and ventral suckers are responsible for schistosome adhesion and locomotion in a non-confined environment

In the absence of confinement and when adhering to over a flat surface, we observed that adult male S. *mansoni* exclusively use their oral and ventral suckers to apply forces (Figure 2). Both suckers generated various coordinated patterns of traction stress on their substrate, namely contraction, expansion and rotation. Most frequently, we recorded an inward contractile pattern (Figure 5.2A, D), which could be sustained by worms for prolonged periods of time. This inward contractility is consistent with a suction pressure difference being generated inside the sucker. The same pattern was also observed in other environmental conditions, such as under flow and when physically confined (see below). Outward stress patterns also occurred in some cases for both suckers (Figure 5.2B,E). However, these force-generation events were transient and not observed when S. *mansoni* was subjected to flow. The data suggest that the suckers of S. *mansoni* are sessile that generate pressure differences by expanding and contracting the suction cup, as opposed to stalk suckers with

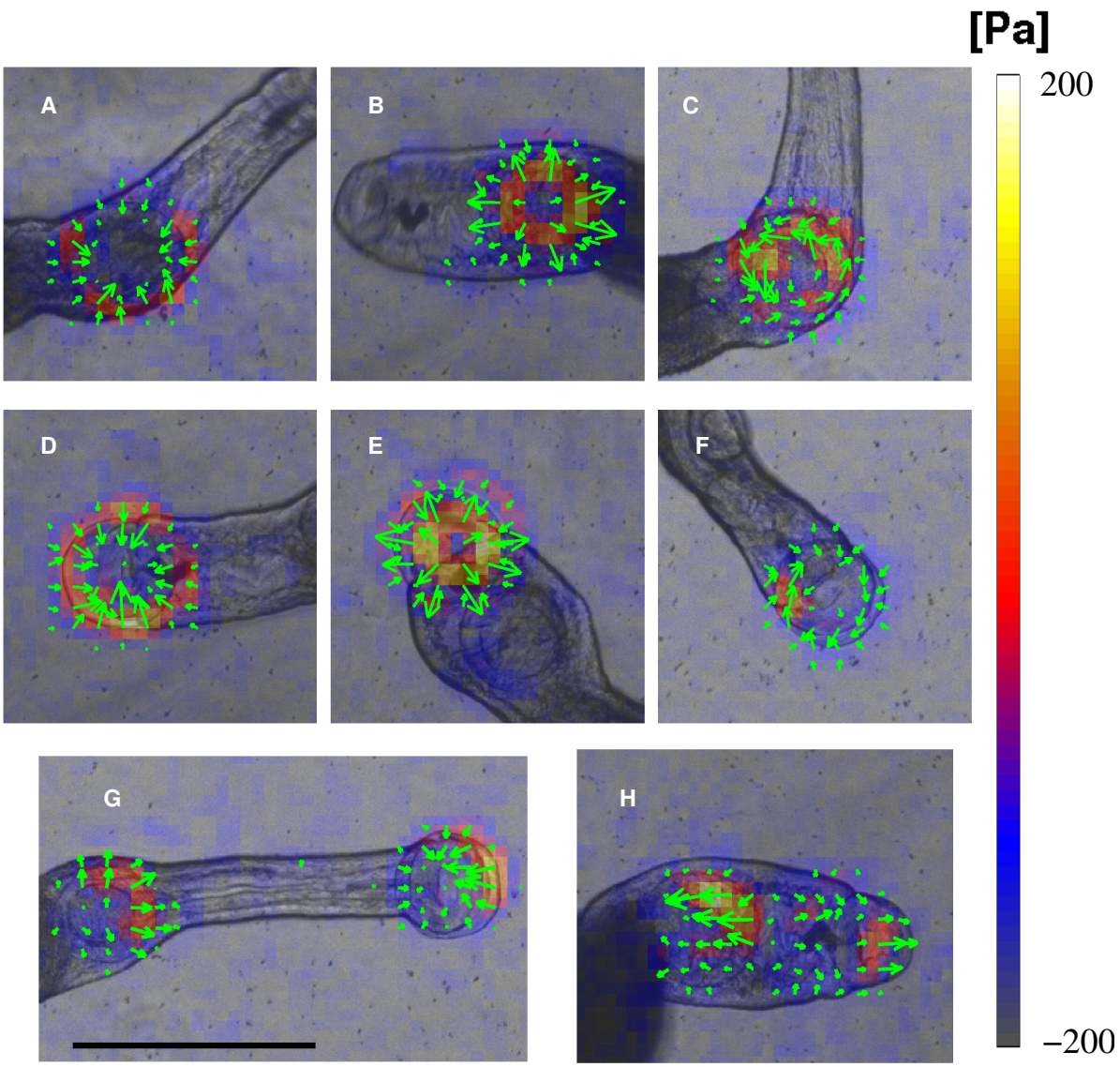

Figure 5.2: Instantaneous traction stress patterns applied by S. *mansoni* suckers in an unconfined environment. (**A**, **B**, **C**) Inward, outward and rotational patterns induced by the ventral sucker alone. (**D**, **E**, **F**) Inward, outward and rotational patterns induced by the oral sucker alone. (**G**) Contractile traction stress pattern applied by coordination of the oral and ventral suckers. (**H**) Expanding traction stress pattern applied by coordination of the oral and ventral suckers. The arrows and color map indicate the direction and magnitude of the traction stress vector, and have been superimposed on bright field images of the worm. Scale bar = 1 mm.

a rigid cylinder and generate pressure differences by pulling on the stalk which is connected with a piston [100].

Rotational traction stress patterns were also often observed under the suckers (Figure 5.2C,F), typically coinciding with changes in the worm's direction of motion or with in-

plane rotations of the body. This result indicates that the suckers of S. *mansoni* are crucial for pivoting during locomotion. To understand whether the suckers actively coordinate chiral contractility, or whether the observed chiral patterns were a passive reaction to net hydrodynamic torque acting on the body of the worm, we performed experiments with worms that had been cut just posterior to the ventral sucker. In these worm fragments, we observed both contractile and expansive traction stress patterns in the suckers, but not rotational ones. Thus, the rotational traction stress patterns observed in whole worms are passive and not actively generated by the suckers.

While resting, S. *mansoni* typically adhered with just one sucker, either the oral or the ventral one. However, we observed coordinated adhesion and traction force patterns during locomotion, which involved the two suckers as well as the body ('neck') between the suckers. This coordination resulted in "marching". When marching forward, the neck elongates supported by the ventral sucker until the oral sucker adheres to the substrate. Then, the ventral sucker detaches and the neck contracts, dragging the entire worm forward towards the oral sucker, which, in turn, detaches after the ventral sucker re-adheres to the substrate. The reverse sequence of actions was also observed for backward marching. The marching is somewhat similar to the motion of an inchworm, however, for S. *mansoni* , both adhesion points are located in a relatively small anterior 'neck' region.

In many instances, while marching, the neck elongated or contracted before one of the suckers had detached from the substrate, which allowed us to measure a pattern of contractile (Figure 5.2G) or expansive (Figure 5.2H) traction stress coordinated between the two suckers. This result suggests that the suckers may sense mechanical forces to regulate the adhesion and locomotion of S. *mansoni* .

5.3.2 Sucker adhesion strength increases in response to increasing flow stress

In vivo, mature S. *mansoni* reside in the hepatic portal and the mesenteric veins where they are subjected to blood flow stress of varying magnitude. To study the adhesion and motility of S. *mansoni* under physiologically representative flow conditions, we performed experiments in a customized flow chamber (Figure 5.1A2) designed to supply varying levels of flow rate and shear stress on worms.

Figure 5.3A shows as the flow rate was increased through the flow chamber, the

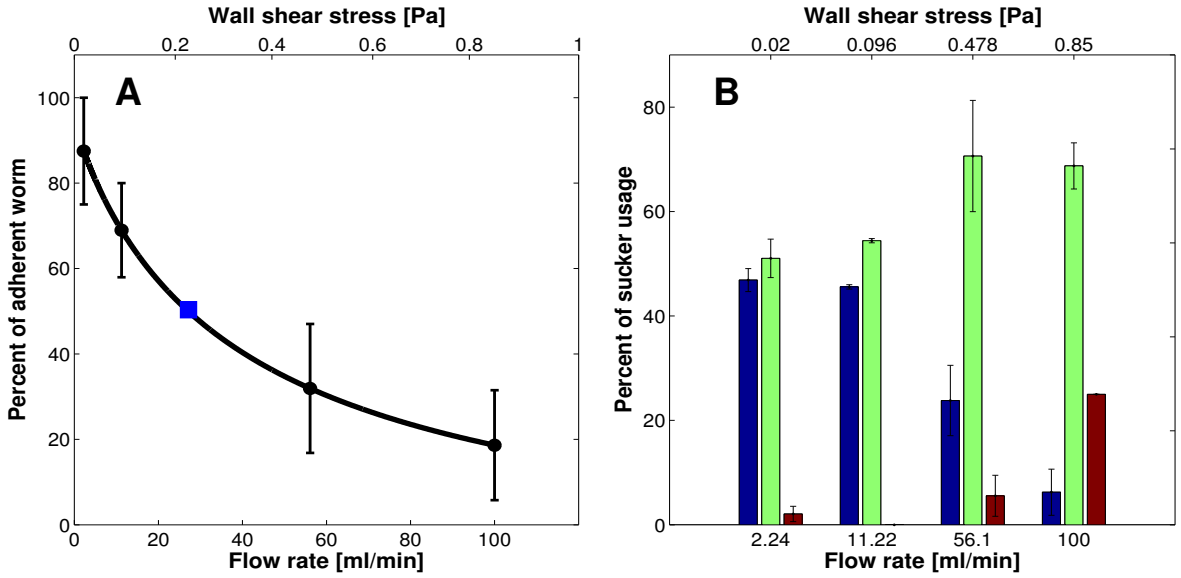

Figure 5.3: Substrate adherence of S. *mansoni* under flow. (**A**) Percentage of adherent S. *mansoni* as a function of flow rate and corresponding wall shear stress (average +/- standard error, n=4 worm batches with 11, 20, 5 and 5 worms). A dose-response curve based on fitting to the Hill Equation is plotted in black. The blue square indicates the 50% detachment flow rate based on the model. (**B**) Distribution of sucker usage as a function of flow rate and corresponding wall shear stress (Blue – oral sucker alone; green – ventral sucker alone; red – both suckers, data are average +/- standard error).

percentage of S. *mansoni* that could withstand the hydrodynamic drag and remain attached to the substrate decreased sharply. The corresponding wall shear stress associated with the flow rate is also labeled in the figure. The sucker primarily responsible for adhesion was the larger ventral sucker. Whereas $> 80\%$ of the worms remained attached at the lowest flow rate of 2.24 ml/min, $\sim$80% of the worms were washed away at the highest flow rate of 100 ml/min. As this behavior is reminiscent of the dose-response curve of a drug effect, we fitted our data using the Hill equation [101, 102] and found that the 50% detachment flow rate was $Q_{50} = 26.6$ ml/min. The traction stress measured in the flow chamber (Figure 4) is consistent with the observed response in attachment. At low flow rates, the ventral sucker exerts a contractile pattern of traction stress, as indicated by the dipolar structure of both the flow (τ_{xz}) and the cross-flow (τ_{yz}) components of the stress (Figure 5.4A, D, G). This pattern is similar to that observed in the flow-free condition (Figure 2A). As Q increased, so did the hydrodynamic drag experienced by the worm, which was balanced by the traction stress under the ventral sucker. Consequently, τ_{xz} increased markedly in magnitude and lost its dipolar structure, becoming unidirectional (Figure 5.4 D-F).

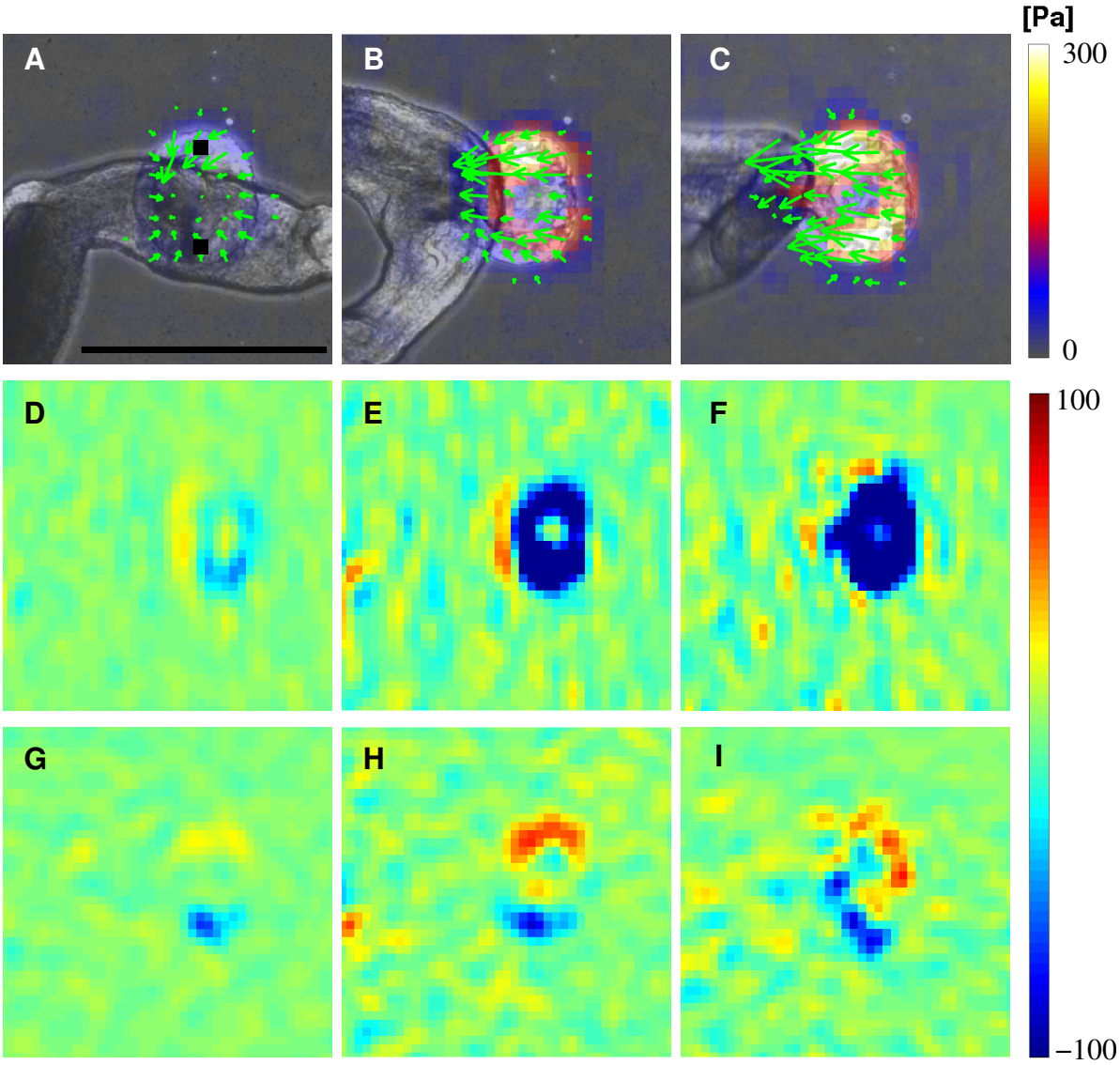

Figure 5.4: Instantaneous traction stress patterns applied by S. *mansoni* anchoring against flow. (**A**, **B**, **C**) Traction stress patterns for different flow rates. The arrows and color map indicate the direction and magnitude of the traction stress vector. (**D**, **E**, **F**) Traction stresses in the flow direction for different flow rates. (**G**, **H**, *I*) Traction stresses perpendicular to the flow direction for different flow rates. (**A**, **D**, **G**) Flow rate = 11.22 ml/min, (**B**, **E**, **H**) 56.1 ml/min or (**C**, **F**, **I**) 100 ml/min. The black squares in A indicate positions where grabbing strength is calculated from traction stress. Scale bar = 500 μm.

Our experimental data suggest that there is a maximum level of traction stress the ventral suckers of S. *mansoni* can withstand before detaching from their substrate. Consistent with this finding, the worms transitioned from using either the oral or ventral sucker to attach to the substrate under no flow, to preferentially using the stronger ventral sucker, and then, increasingly, both suckers as Q was raised (Figure 5.3B). By applying equilibrium

of forces for the highest flow rate condition, it should be possible to estimate the maximum traction stress τ_{max} that one sucker is able to withstand before detaching. Assuming that the flow around the worm is dominated by viscous stress (i.e. steady flow with negligible inertia),

$$\tau_{max} \sim \frac{\mu U}{R} \times \frac{2\pi RL}{A_{lip}} = \frac{18L\mu U}{5R^2} \sim 150Pa, \tag{5.1}$$

where the worm is assumed to have a cylindrical shape of length $L \sim 10^{-2}m$ and radius $R \sim 0.25 \times 10^{-3}m$, $\mu \sim 10^{-3}Pa \cdot s$ is the molecular viscosity of the medium, $U \sim 0.25m/s$ is the centerline velocity in the flow chamber, and $A_{lip} \sim \pi(R + \frac{2R}{3})\frac{R}{3} = \frac{5}{9}\pi R^2$ is the area of the sucker lip in contact with the substrate, which has been assumed to have a width equal to $R/3$ (see Figure 5.1A). This estimation agrees reasonably with the values of the traction stress measured in the flow chamber for the highest flow rate (Figure 5.4F). Using similar arguments, the value of $\tau_{max,50}$ corresponding to $Q_{50} = 26.6$ ml/min can be estimated to be $\tau_{max,50} \sim 40$Pa.

Interestingly, the cross-flow traction stress kept their contractile pattern but also increased in magnitude with the flow rate (Figure 5.4G-I). This result suggests that S. *mansoni* senses hydrodynamic forces and responds to them by grabbing the substrate with increasing strength via their suckers in order to remain attached to the substrate. To test this hypothesis, we plotted the grabbing strength of adult male worms vs. Q for each worm normalized by its corresponding value for $Q = 0$ (Figure 5.5). We quantified grabbing strength from the cross-flow component of the traction stress τ_{yz}, as the average magnitude of τ_{yz} at two diametrically opposed regions under the adhering sucker in the axis perpendicular to the flow (black regions in Figure 5.4A). We then used our estimation of Q_{50} to categorize each worm as adherent if they remained attached for $Q > Q_{50}$ or non-adherent otherwise. These results indicate that adherent worms gradually increased their grabbing strength in response to increasing flow rate.

5.3.3 Locomotion of S. *mansoni* under varying degrees of confinement

To study the motility of S. *mansoni* in a setup that mimics the more narrow bores of mesenteric veins, we sandwiched worms between a PA substrate and agar caps that created varying levels of confinement (see Methods section). The traction stress exerted by the

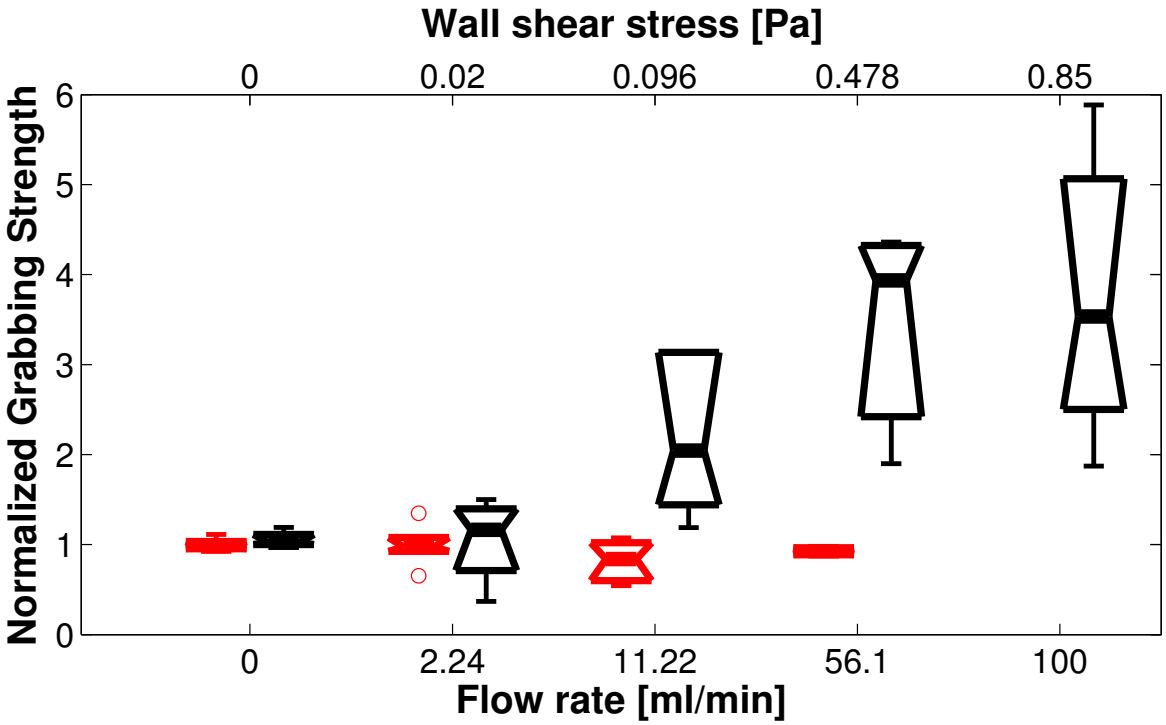

Figure 5.5: Adhesive strength of S. *mansoni* subjected to stepwise increases in flow rate. The adhesive strength is calculated from the traction stresses perpendicular to the flow direction and normalized with its value at zero flow rate. The black boxplots correspond to worms that remain attached to the substrate for flow rates $Q > Q_{50}$. The red boxplots corresponds to worms that detached from the substrate for $Q > Q_{50}$.

worms varied notably with the level of confinement. As explained above, S. *mansoni* employs its suckers to move under no confinement, so that no measureable traction stress was recorded along the main body (Figure 5.6A-D). When the gap between the PA gel and the agar cap was slightly narrower (300 μm) than the diameter of the worm's body ($\sim$ 500 μm), S. *mansoni* maintained the same inch worm-like mechanism used on free surfaces, but also generated traction stress along the body with coordinated body contractions. In these conditions of increased substrate resistance, the traction stress applied by the suckers increased dramatically in magnitude (generally more than 10 times larger than in no confinement condition) to account for the additional friction created between the body and the substrate (Figure 5.6E-H).

Remarkably, S. *mansoni* switched to a completely different locomotion strategy when crawling through more restrictive conditions whereby the gap between the PA gel and the agar cap was decreased to 100 μm. Specifically, traveling waves of strong traction stress

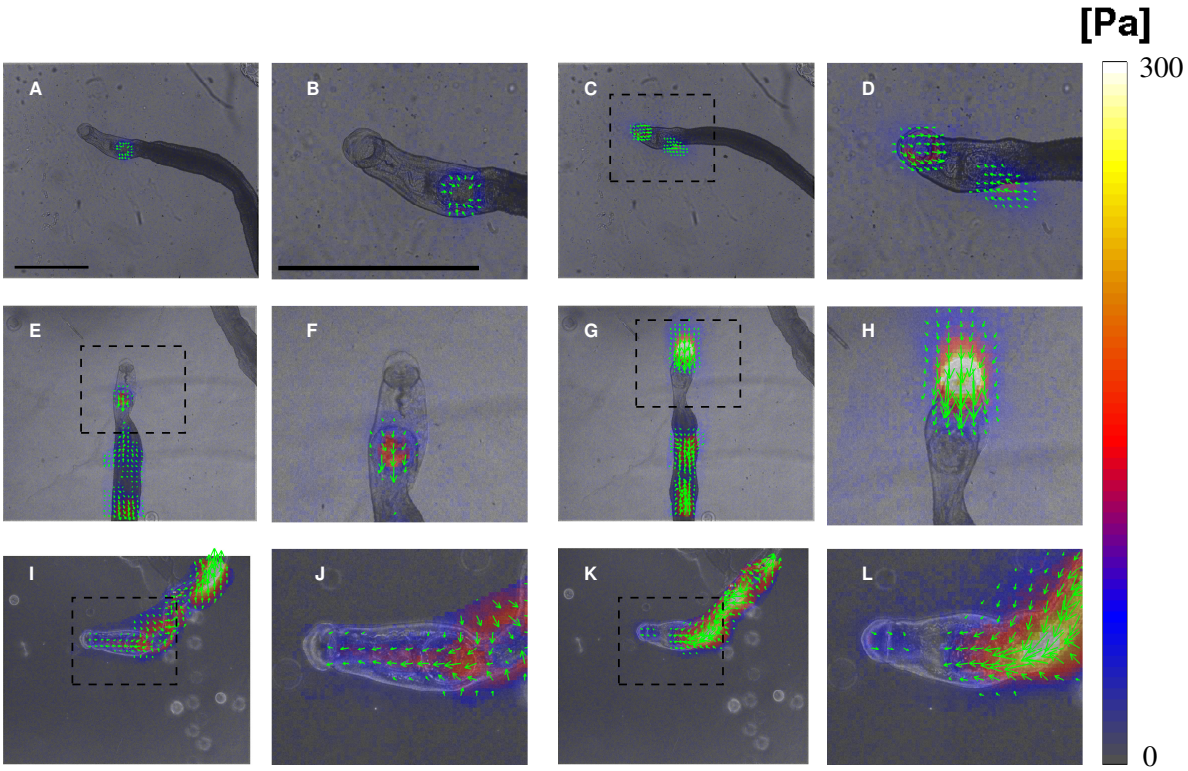

Figure 5.6: Instantaneous traction stress patterns exerted by S. *mansoni* under varying levels of confinement. (**A**-**D**) No confinement. (**E**-**H**) Gentle confinement (300 μmgap between substrate and agar cap). (**I**-**L**) Severe confinement (100 μmgap). (**A**, **E**, **I**) Traction stress exerted while extending the oral sucker forward. (**C**, **G**, **K**) Traction stress exerted while contracting the neck region between the oral and ventral suckers. Panels **B**, **D**, **F**, **H**, **J**, **L** are enlarged views of the boxed areas in panels **A**, **C**, **E**, **G**, **L**, **K**. The arrows and color map indicate the direction and magnitude of the traction stress vector, and have been superimposed on bright field images of the worm. Scale bar = 1 mm.

along the body of the worm were recorded (Figure 5.6I-L). These waves exhibited a rich variety of spatio-temporal patterns which could emerge from any position along the body and propagate towards the anterior or posterior at various wave speeds, leading to a wide range of locomotion behaviors. Here we focus on persistent forward locomotion, which was always achieved by peristaltic waves of muscle contraction and traction stress, by performing a series of experiments with the gap size of 100 μm.

Figure 5.7B displays a representative kymograph of worm body width, revealing that 2-3 peristaltic waves of muscle contraction were present along the worm's body at any given time. These contraction waves always (red bands in the kymograph) originated at the anterior part of the main body, immediately behind the ventral sucker (green dot in Figure 5.7A), and traveled backwards with a wave speed $c \approx 1$ mm/s. Of note, while the contraction

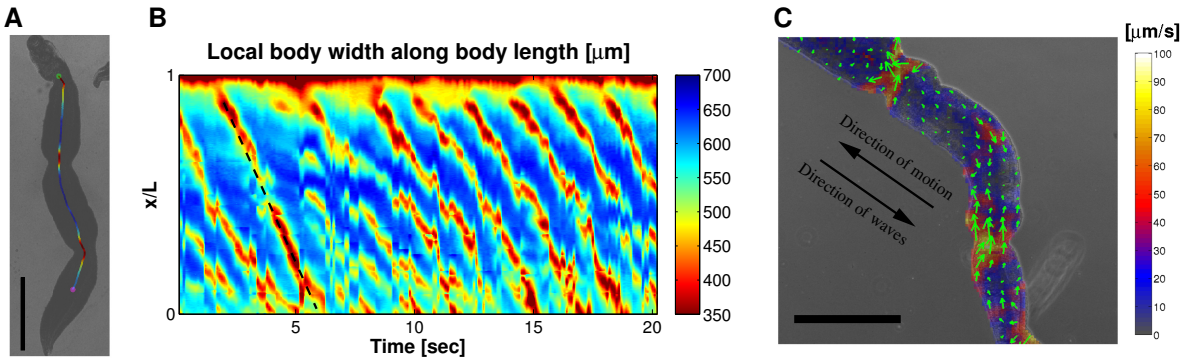

Figure 5.7: Kinematics of S. *mansoni* movement under confinement. (**A**) Instantaneous body width of a worm (represented in color along the worm's centerline) in a 100 μmgap, showing three contraction waves. The green and magenta dots indicate the starting (just behind the ventral sucker) and final (500 μmfrom the posterior tip) positions of the body width measurement. (**B**) Kymograph of body width represented as a function of time and normalized position along the centerline (1=anterior end and 0=posterior end). (**C**) Instantaneous map of body movement velocities. The arrows and color map represent the direction and magnitude of the velocity vector, and have been superimposed on bright field images of the worm. Scale bar = 1 mm.

waves traveled backwards, the body of the worm experienced fast ($\sim$ 100 μm/s) forward displacement in the wave regions, as shown in Figure 5.7C. This figure maps the velocities of material points on the surface of the worm, which were measured by tracking their associated texture in bright-field image sequences via cross-correlation analysis, similar to Lai *et al.*[9]. On the other hand, the regions between contractions, i.e., the interwave regions, experienced very slow ($\sim$ 10 μm/s) backward displacement.

These data suggest that S. *mansoni* exploits passive friction to generate thrust forces at the interwave regions, and that these forces balance the resistance created by the forward displacement of the body in the wave regions. To confirm this idea, we measured the deformations and traction stress exerted by S. *mansoni* during locomotion, and mapped them together with bright field images of the worm body (Figure 5.8A-F). As expected, these maps showed that the longitudinal substrate deformations and traction stress were propulsive, i.e., point backwards, in the interwave regions, whereas they were resistive in the wave regions. The peristaltic contraction waves also co-localized with regions of strong transversal deformation and traction stress. Consequently, the profiles of worm width and longitudinal traction stress along the body of S. *mansoni* had opposite phases (Figure 5.8G), with traction stress maxima co-localizing with areas of body contraction. The kymographs of body width and longitudinal traction stress (Figure 5.9) indicate that the spatio-temporal

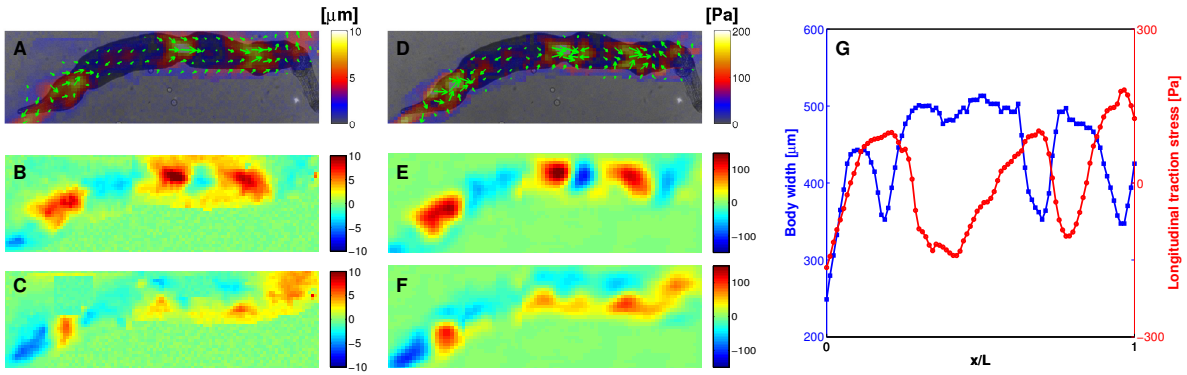

Figure 5.8: Dynamics of S. *mansoni* movement under confinement. (**A**) Instantaneous substrate deformation patterns exerted by a moving worm in a 100 μmgap. (**B**, **C**) Maps of instantaneous substrate deformation in the directions longitudinal (**B**) and transverse (**C**) to worm body motion. (**D**) Instantaneous traction stress patterns exerted by a migrating worm. (**E**, **F**) Maps of instantaneous traction stress in the directions longitudinal (**E**) and transverse (**F**) to worm body motion. In panels (**A**) and (**D**), the arrows and color maps represent the direction and magnitude of the deformation and traction stress vectors, and have been superimposed on bright field images of the worm. Scale bar = 1 mm. (**G**) Simultaneous measurements of worm body width (blue) and longitudinal traction stress (red) along the worm's centerline (0 = posterior end, 1 = anterior end).

dynamics of these quantities are similar, all exhibiting retrograde traveling waves with the same period and wave speed. To migrate within the narrow vessels, S. *mansoni* also need to be able to move backward since there is no room to rotate the whole body. As expected, backward locomotion can be achieved by reversing the direction of the wave to propagate from the tail to the head.

5.3.4 Sucker action and peristaltic body contractions can be coordinated during locomotion under confinement

During locomotion in confined environments, about 75% (14 out of 19) of the worms analyzed employed peristaltic body waves and not their suckers. The other 25% of worms employed their suckers in addition to body waves. To understand whether these two independent locomotor mechanisms could be coordinated, we measured the length of the head region between the oral and ventral suckers and plotted its time evolution together with that of the width of the anterior part of the worm's main body (Figure 5.10A). The data indicate that, for worms using both their suckers and peristaltic waves, the waves were initiated when the head region reached its minimum length and the ventral sucker completed

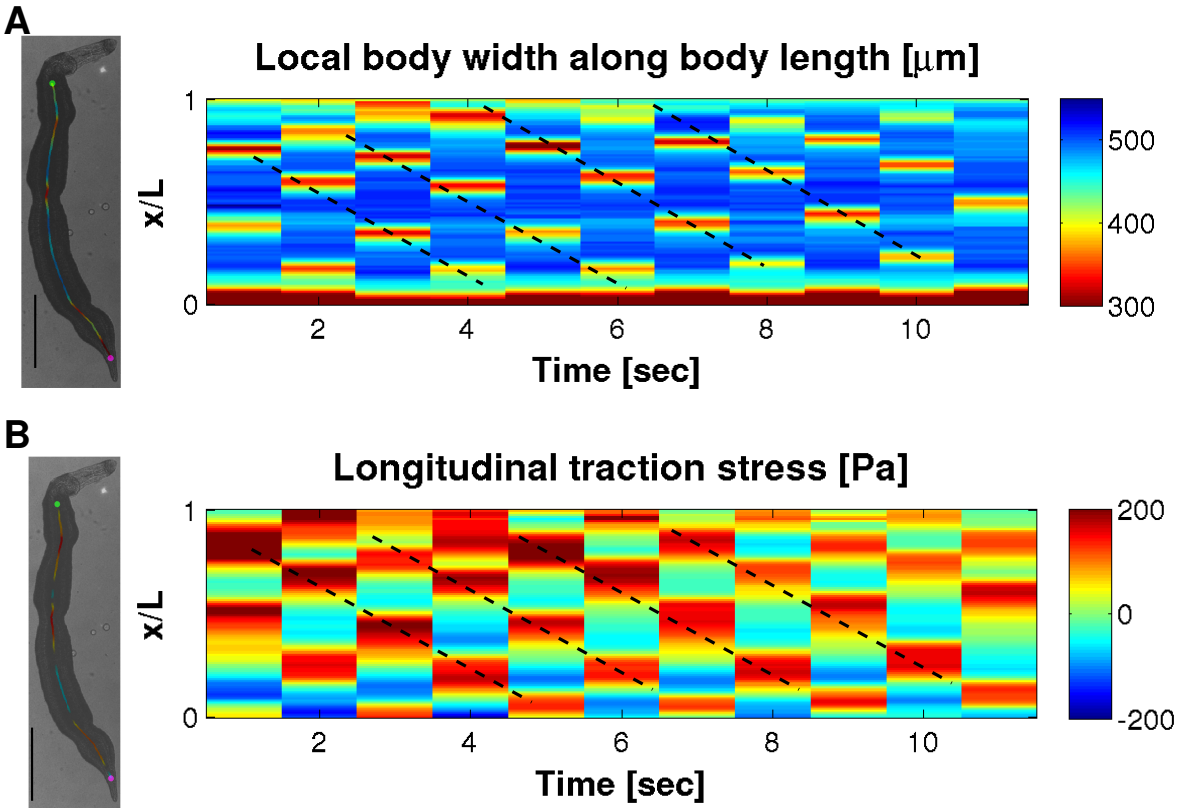

Figure 5.9: Peristaltic waves of body contractions and propulsive stresses. (**A**) Kymograph of body width along the body of S. *mansoni* moving under confinement (100 μm gap). (**B**) Kymograph of longitudinal traction stress recorded simultaneously with body width for the same worm. The dashed lines in both kymographs correspond to peristaltic waves of body width and longitudinal traction stress propagating backward. The worm image insets on the left-hand side show instantaneous body width and traction stress measurement along the worm's centerline.

its forward step toward the oral sucker before establishing a new adhesion. This behavior can be appreciated in bright-field images of migrating worms (Figure 5.10B). It leads to the continuous propagation of a wave of forward displacement from the anterior to the posterior of the worm via coordination of two markedly different mechanisms (Figure 5.10C) leading to faster locomotion.

We also observed that S. *mansoni* could switch their locomotion between peristaltic waves alone, and suckers and peristaltic wave coordination. We analyzed all 19 specimens that sustained more than eight cycles in a given mode and found that worms with sucker - peristaltic wave coordination migrated significantly faster than those employing peristaltic waves alone (median speeds 80.6 μm/s vs. 25.7 μm/s; Mann-Whitney test p-value < 0.01; see Figure 5.11A). This difference could be explained by considering that, on average, worms

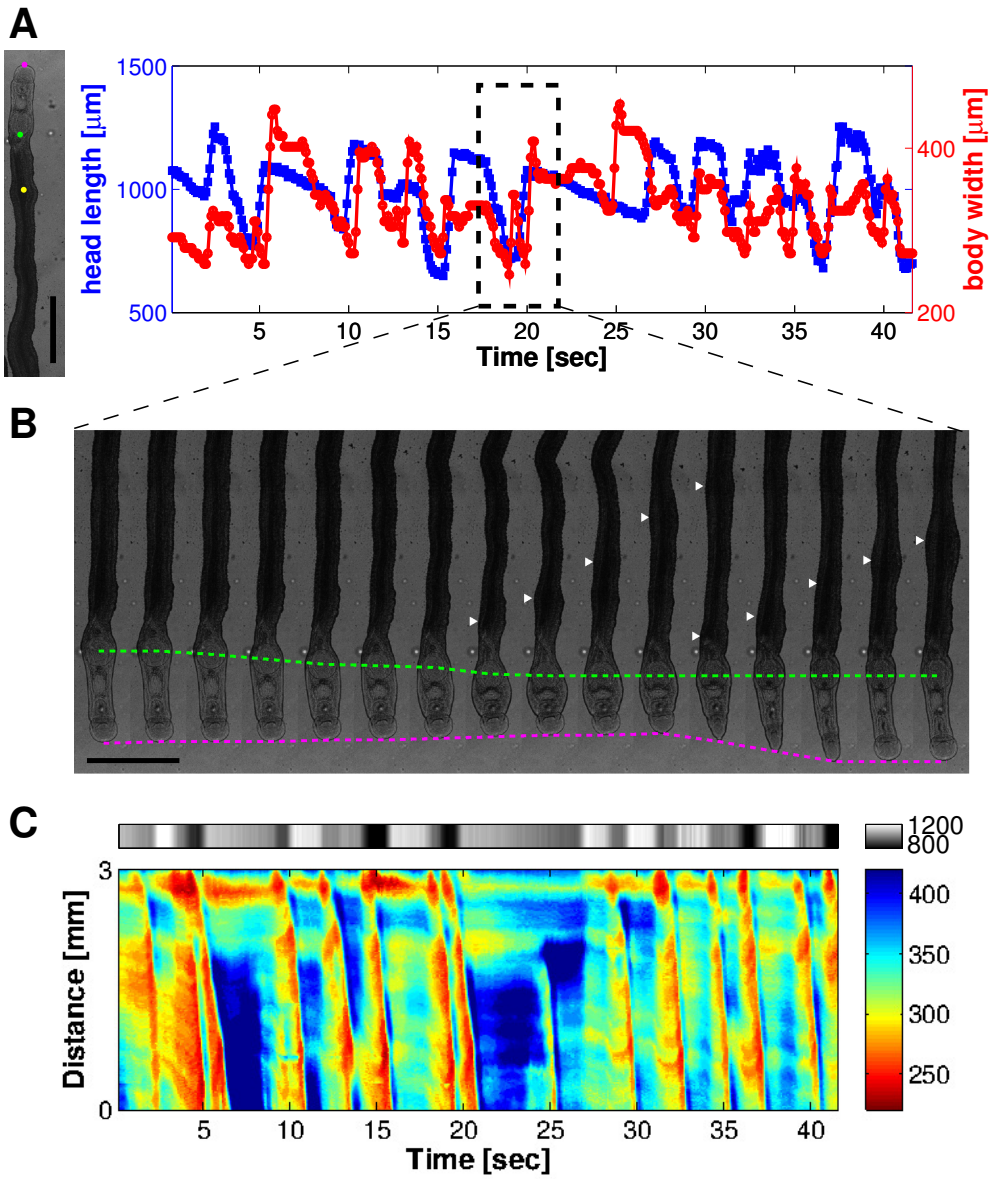

Figure 5.10: Coordination between body contractions and sucker-mediated propulsion in S. *mansoni* migrating under confinement. (**A**) Head length of a worm as a function of time (red) together with body width at a longitudinal position near the head (blue) under confinement (100 μm gap). The magenta and green points in the bright field image of the worm to the left mark the anterior and posterior ends of the head region, whereas the yellow point marks the location at which body width was plotted. (**B**) Montage of bright field images. White triangles mark the position of body wave, the green dashed line shows the position of ventral sucker and the magenta dashed line indicates the position of oral sucker. (**C**) Composite kymograph of head length (top, grey color map) and body width (bottom, rainbow color map). The data show multiple instances when peristaltic body contraction waves (red ridges) firing at the point when the head length is shortest (dark grey).

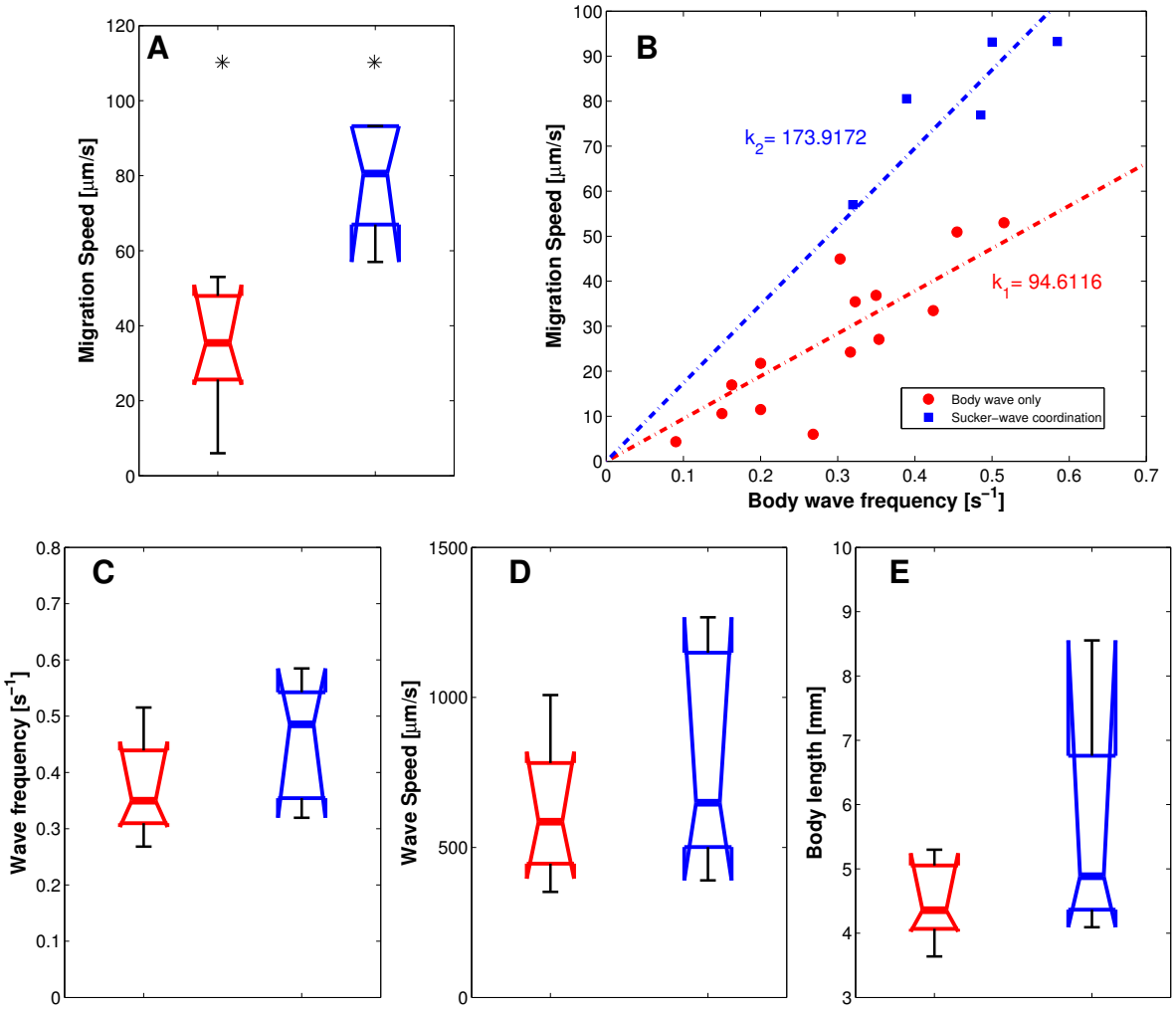

Figure 5.11: Coordination between peristaltic body contractions and sucker-mediated propulsion in S. *mansoni* migrating under confinement. (**A**) Box plots of S. *mansoni* worm speeds (100 μm gap) using exclusively peristaltic waves of body contractions (red, n=8) or by coordinating sucker motion with peristaltic body waves (blue, n=5). Asterisks denote statistically significant differences between medians (Mann-Whitney test p-value < 0.01). (**B**) Scatter plot of movement speed versus frequency of peristaltic waves. Red circles – peristaltic waves only; blue squares – sucker - peristaltic wave coordination. Linear least square fits through the origin are applied to each data set. (**C**-**E**) Box plots of motility parameters for worms migrating exclusively by peristaltic waves of body contractions (red, n=8) or by sucker - peristaltic wave coordination (blue, n = 5): (**C**) average wave frequency, (**D**) average wave speed and (**E**) average body length.

migrated forward a fixed distance with each wave cycle, i.e., a stride length (the slope of the regression lines in Figure 5.11B). Then, engaging the suckers in the motion cycle results in a longer stride (174 μm vs 95 μm, see Figure 5.11B). In an attempt to find additional differences between the two locomotion modes, we compared their wave frequency, wave

speed and worm body length. Because we found a trend for wave frequency to be higher in worms with sucker - peristaltic wave coordination, we compared wave speed and body length in a subgroup of experiments with wave frequency more than 0.3 Hz. However, we did not find significant differences in these variables (Figure 5.11C, D, E). Overall, the data indicate that S. *mansoni* , under confinement, move via peristaltic waves along the long axis of the worm which can be coordinated with the marching action of the oral and ventral suckers.

5.4 Discussion

Soft bodied animals are generally lack of extremities. Instead, they utilize a fluid skeleton as mechanism of locomotion. The fluid skeleton does not necessarily have to contain fluid which can flow freely. However, tissue structures loosely constructed is enough to allow small changes in shape and permit muscular antagonism for motility. During locomotion, soft-bodied organisms generate waves of muscular contractions. The energy of muscle contraction is then transmitted by the fluid of the hydraulic system to the surface of the organism and dynamically vary their shape, which exerts traction stress against the environment and acts as the propeller [1]. In general there seems to be comparatively few ways in which the demands of robust locomotion can be met, so it is not surprising that soft-bodied organisms of different phyla exhibit convergent evolution and show similar adaptations in response to similar mechanical problems.

In this work, we provided detailed experimental data and have shown that S. *mansoni* uses coordinate dynamics between oral and ventral suckers generating forces to migrate in the environment without confinement. When subjecting to flow of varying magnitude, S. *mansoni* actively adjust its grabbing strength via suckers to remain attached to the substrate. Similar mechanisms of sucker usage are also found in nemertine *Malacobdella* [91] and leech *Hirudo* [6]. When migrating under confined environment, S. *mansoni* switched to a completely different locomotion strategy and generating peristaltic retrograde waves traveling along the body to migrate forward. This is essentially the same mechanism utilized by earthworm to move on the surface of substrate or burrow into soft materials. It should be noted that as earthworms crawl forward, they actively extend the setae on the wider part of the segments to provide stronger anchorage on the substrate and retract the setae at the thinner segment to reduce the friction [10]. The scanning electron microscopy of S. *mansoni* revealed tubercles scattered irregularly over the surface of their body [103–105].

However, whether and how these structures are actively involved in the migration by varying the spatio-temporal distribution of adhesion coefficient still need further investigation.

During the migration under constrained environment, we found two different locomotion mechanism yielding distinct characteristic migration speed, depending on whether the suckers are involved in the locomotion. The ones actively utilize their suckers and synchronized with the generation of body waves exhibit a significant higher migration speed compare with the ones migrating using body waves only. This phenomenon can be explained as the passive suckers induce a pure friction with the surrounding environment, thus hinder the worm to achieve a high migration speed. On the other hand, the active sucker dynamics can be regarded as an extended anterior-most part of the body wave. Because of the synchronization with the body wave, suckers only need to exert a small magnitude anchorage forces on the substrate to overcome the friction of the anterior most segment of the body. We do observed that the worms under strongly constrained environment exert weaker stress under the suckers compared with under gently constrained environment or in free moving environment without constrain. Interestingly, recent studies revealed that S. *mansoni* has two brains. Our data poses a fundamental question for the brain functions of complex neuromuscular control for dynamical behaviors of body wave and sucker dynamics.

Throughout this study, we have thoroughly investigated the mechanisms of locomotion when S. *mansoni* facing different mechanical challenges, and provided many quantities involved in locomotion such as the detachment rate and grabbing strength to various flow rate, the migration velocity and body wave frequency as well as traction stress under suckers and body. All of these would offer significant values in discovery and development of new drugs.

5.5 Acknowledgements

Chapter 5, in part, has been submitted. Zhang, Shun ; Skinner, Danielle; Joshi, Prateek ; Lasheras, Juan C ; Caffrey, Conor R ; del Álamo, Juan C. 2018. The title of this paper is "Locomotor adaptability of the schistosome pathogen to changes in its physical environment: mechanical principles and implications for drug discovery". The dissertation author was the primary author of this paper.

Chapter 6

Conclusion

This work mainly focused on the mechanics of flow, contractility and adhesion during soft adhesive locomotion using *Physarum* polycephalum as the model organism. To this end, we combined measurements of traction force, fragment morphology, endoplasmic and ectoplasmic velocity, ectoplasmic microrheology properties and endoplasmic Ca^{2+} concentration with experimental manipulations of cell-substrate adhesion, cortical strength and cell size. In parallel, we worked closely with mathematicians to develop a computational model which includes forces from the viscous cytosol, a poro-elastic, contractile cytoskeleton and adhesive interactions with the substrate.

Our results suggest a hydrodynamic instability governs motility initiation of flow-driven amoeboid cell, and the process is determined by capillary number, which involves the interplay of size, cortical strength and cell-substrate adhesion. We also found that most migrating *Physarum* fragments exhibit two types of wave patterns in endoplasmic flow, contractility and chemical signaling. Slow-moving fragments display standing wave patterns similar to amoeboid cells such as leukocytes or Dictyostelium. Fast-moving fragments exhibit traveling wave patterns of traction stress, which are conserved in larger organisms such as annelids or gastropods, and are reminiscent of leg density waves in myriapod locomotion. Combined our experimental data with computational model, we show that traveling waves of traction stress require tight coordination between contractility and substrate adhesion. A specific phase difference $3\pi/2$ between adhesion and contractility in the computational model generates most similar wave patterns of endoplasmic flow and traction stress with the experimental observations. Furthermore, we found this specific phase difference provide the most robust migration speed in the presence of heterogeneous friction from the environment,

which suggests *Physarum* choose robustness over maximum migration speed in nature.

Standing and traveling wave patterns result from the nonlinearity nature of the interplays between intracellular flow, traction stress, chemical signaling and adhesion. Interestingly, we found similar wave patterns of traction stress on higher organisms with much complex neuromuscular coordination. We thoroughly investigated the mechanics of locomotion of the flatworm *Schistosoma mansoni* (the most prevalent human endoparasite) under varying levels of confinement, representative of the environments this flatworm encounters in its migratory route from the liver to the intestine. Our results reveal that S. *mansoni* migrates by exerting standing waves of traction stresses with its suckers under no or gentle confinement, but transitions to exerting traveling waves of traction stress along its body when crawling through in highly restrictive conditions. Furthermore, we find the traveling waves of body contraction and the standing waves of sucker actions can be coordinated to achieve faster locomotion with a longer stride length, which is defined as the distance S. *mansoni* migrated as one body wave propagates across the body.

In Chapter 2, we have combined traction force and morphology measurements with experimental manipulations of cell-substrate adhesion, cortical strength and cell size of *Physarum* fragments to understand the contribution of these mechanical factors to symmetry breaking and motility initiation in flow driven amoeboid cell. Our experimental evidence suggests a close dependence of probability of motility initiation with size and morphology. Furthermore, this relation is strongly affected by cell-substrate adhesion and cortical strength.

In Chapter 3, we have examined the relationship between spatio-temporal coordination of intracellular flow and traction stress and the speed of amoeboid locomotion of microplasmodia of *Physarum polycephalum*.We simultaneously perform particle image velocimetry and traction stress microscopy to measure the velocity of cytoplasmic flow and the stresses applied to the substrate by migrating *Physarum* microamoebae. In parallel, we develop a mathematical model of a motile cell which includes forces from the viscous cytosol, a poro-elastic, contractile cytoskeleton and adhesive interactions with the substrate. Our experiments show that flow and traction stress exhibit back-to-front-directed waves with a distinct phase difference. The model demonstrates that the direction and speed of locomotion are determined by this coordination between contraction, flow and adhesion. Using the model, we identify forms of coordination that generate model predictions consistent with experiments. We demonstrate that this coordination produces near optimal migration speed

and is insensitive to heterogeneity in substrate adhesiveness.

In Chapter 4, we measure the spatio-temporal distributions of the velocities of the endoplasm and ectoplasm of migrating *Physarum* fragments, the traction stresses it generates on the substratum, and the concentration of free intracellular calcium. Using these unprecedented experimental data, we classify migrating *Physarum* fragments according to their dynamics, finding that they often exhibit spontaneously coordinated wave patterns of flow, contractility and chemical signaling. We show that *Physarum* fragments exhibiting symmetric spatio-temporal patterns of these quantities migrate significantly slower than fragments with asymmetric patterns. In addition, our joint measurements of ectoplasm velocity and traction stress at the substratum suggest that forward motion of the ectoplasm is enabled by a succession of stick-slip transitions, which we conjecture are also organized in the form of waves. Combining our experiments with a simplified convection-diffusion model, we show that the convective transport of calcium ions may be key for establishing and maintaining the spatio-temporal patterns of calcium concentration that regulate the generation of contractile forces.

In Chapter 5, we explored the mechanics of locomotion of the schistosome pathogen under physiologically relevant conditions using self-designed experimental setups and devices. We revealed, for the first time, that S. *mansoni* change the locomotion mechanisms when facing different physiologically relevant mechanical challenges. S. *mansoni* exclusively use their oral and ventral suckers generating forces to migrate in the environment without confinement around their body. When subjecting to flow of varying magnitude, S. *mansoni* actively adjust their grabbing strength via their suckers to remain attached to the substrate. However, S. *mansoni* switched to a completely different locomotion strategy when crawling through restrictive conditions by applying traveling waves of strong traction stress along the body. Strikingly, we discovered the sucker action and body contraction wave can be coordinated to achieve faster locomotion when migrating under restrictive environment.

Bibliography

[1] Trueman ER. Locomotion of soft-bodied animals. Edward Arnold; 1975.

[2] Lämmermann T, Sixt M. Mechanical Modes of 'Amoeboid' Cell Migration. Current Opinion in Cell Biology. 2009 Oct;21(5):636–644.

[3] Charras G, Paluch E. Blebs Lead the Way: How to Migrate Without Lamellipodia. Nature Reviews: Molecular Cell Biology. 2008 Sep;9(9):730–736.

[4] Lämmermann T, Bader BL, Monkley SJ, Worbs T, Wedlich-Söldner R, Hirsch K, et al. Rapid Leukocyte Migration by Integrin-Independent Flowing and Squeezing. Nature. 2008 May;453(7191):51–55.

[5] Miller P, Wilson R. Migration of the schistosomula of Schistosoma mansoni from the lungs to the hepatic portal system. Parasitology. 1980;80(2):267–288.

[6] Gray J, Lissmann H, Pumphrey R. The mechanism of locomotion in the leech (Hirudo medicinalis Ray). Journal of Experimental Biology. 1938;15(3):408–430.

[7] Wheater P, Wilson R. Schistosoma mansoni: a histological study of migration in the laboratory mouse. Parasitology. 1979;79(1):49–62.

[8] Fetterer RH, Pax RA, Bennett JL. Schistosoma mansoni: Direct method for simultaneous recording of electrical and motor activity. Experimental Parasitology. 1977;43(1):286–294.

[9] Lai JH, Alamo JC, Rodríguez-Rodríguez J, Lasheras JC. The Mechanics of the Adhesive Locomotion of Terrestrial Gastropods. Journal of Experimental Biology. 2010 Nov;213(22):3920–3933.

[10] Quillin KJ. Kinematic scaling of locomotion by hydrostatic animals: ontogeny of peristaltic crawling by the earthworm lumbricus terrestris. Journal of Experimental Biology. 1999;202(6):661–674.

[11] Zhang S, Guy RD, Lasheras JC, del Alamo JC. Self-organized mechano-chemical dynamics in amoeboid locomotion of Physarum fragments. Journal of Physics D: Applied Physics. 2017;50(20):204004.

[12] Mavroidis C, Ferreira A. Nanorobotics: past, present, and future. In: Nanorobotics. Springer; 2013. p. 3–27.

[13] Alvarez-Gonzalez B, Meili R, Bastounis E, Firtel RA, Lasheras JC, Del Alamo JC. Three-Dimensional Balance of Cortical Tension and Axial Contractility Enables Fast Amoeboid Migration. Biophysical Journal. 2015 Feb;108(4):821–832.

[14] Bastounis E, Meili R, Alvarez-Gonzalez B, Francois J, Del Alamo JC, Firtel RA, et al. Both Contractile Axial and Lateral Traction Force Dynamics Drive Amoeboid Cell Motility. Journal of Cell Biology. 2014 Mar;204(6):1045–1061.

[15] Matsumoto K, Takagi S, Nakagaki T. Locomotive Mechanism of Physarum Plasmodia Based on Spatiotemporal Analysis of Protoplasmic Streaming. Biophysical Journal. 2008 Apr;94(7):2492–2504.

[16] Ridgway E, Durham A. Oscillations of calcium ion concentrations in Physarum polycephalum. The Journal of cell biology. 1976;69(1):223–226.

[17] Yoshimoto Y, Matsumura F, Kamiya N. Simultaneous oscillations of Ca^{2+} efflux and tension generation in the permealized plasmodial strand of Physarum. Cell motility. 1981;1(4):433–443.

[18] Joanny JF, Prost J. Active gels as a description of the actin-myosin cytoskeleton. HFSP journal. 2009;3(2):94–104.

[19] Kruse K, Joanny JF, Jülicher F, Prost J, Sekimoto K. Generic theory of active polar gels: a paradigm for cytoskeletal dynamics. The European Physical Journal E. 2005;16(1):5–16.

[20] Yoshida K, Soldati T. Dissection of amoeboid movement into two mechanically distinct modes. Journal of cell science. 2006;119(18):3833–3844.

[21] Lewis OL, Zhang S, Guy RD, del Álamo JC. Coordination of contractility, adhesion and flow in migrating Physarum amoebae. Journal of The Royal Society Interface. 2015;12(106).

[22] Piovanelli M, Fujie T, Mazzolai B, Beccai L. A Bio-Inspired Approach Towards the Development of Soft Amoeboid Microrobots. In: Biomedical Robotics and Biomechatronics, the IEEE RAS EMBS International Conference on. IEEE; 2012. p. 612–616.

[23] Goehring NW, Grill SW. Cell polarity: mechanochemical patterning. Trends in cell biology. 2013;23(2):72–80.

[24] Radszuweit M, Alonso S, Engel H, Bär M. Intracellular Mechanochemical Waves in an Active Poroelastic Model. Physical Review Letters. 2013;110(13):138102.

[25] Radszuweit M, Engel H, Bär M. An Active Poroelastic Model for Mechanochemical Patterns in Protoplasmic Droplets of Physarum polycephalum. PLOS ONE. 2014 06;9(6):1–12.

[26] Banerjee S, Marchetti MC. Instabilities and oscillations in isotropic active gels. Soft Matter. 2011;7(2):463–473.

[27] Barnhart E, Lee KC, Allen GM, Theriot JA, Mogilner A. Balance between cell-substrate adhesion and myosin contraction determines the frequency of motility initiation in fish keratocytes. Proceedings of the National Academy of Sciences. 2015;112(16):5045–5050.

[28] Del Alamo JC, Meili R, Alvarez-Gonzalez B, Alonso-Latorre B, Bastounis E, Firtel R, et al. Three-Dimensional Quantification of Cellular Traction Forces and Mechanosensing of Thin Substrata by Fourier Traction Force Microscopy. PLoS ONE. 2013 Sep;8(9):e69850.

[29] Alvarez-Gonzalez B, Zhang S, Meili R, Firtel RA, Lasheras JC, Del Alamo JC. Two-Layer Elastographic 3-D Traction Force Microscopy. Scientific Reports. 2017;7:39315.

[30] Edelstein A, Amodaj N, Hoover K, Vale R, Stuurman N. Computer Control of Microscopes Using Micro-Manager. Current Protocols in Molecular Biology. 2010 Oct;Chapter 14:14.20.1–14.20.17.

[31] Del Alamo JC, Meili R, Alonso-Latorre B, Rodriguez-Rodriguez J, Aliseda A, Firtel RA, et al. Spatio-Temporal Analysis of Eukaryotic Cell Motility by Improved Force Cytometry. Proceedings of the National Academy of Sciences. 2007 Aug;104(33):13343–13348.

[32] Kukulies J, Stockem W. Function of the microfilament system in living cell fragments of Physarum polycephalum as revealed by microinjection of fluorescent analogs. Cell and tissue research. 1985;242(2):323–332.

[33] Oettmeier C, Lee J, Döbereiner HG. Form follows function: ultrastructure of different morphotypes of Physarum polycephalum. Journal of Physics D: Applied Physics. 2018;51(13):134006.

[34] Callan-Jones A, Joanny JF, Prost J. Viscous-fingering-like instability of cell fragments. Physical review letters. 2008;100(25):258106.

[35] Bray D. Cell Movements. From Molecules to Motility. New York: Garland; 2001.

[36] Allen RD, Pitts WR, Speir D, Brault J. Shuttle-Streaming: Synchronization with Heat Production in Slime Mold. Science. 1963 Dec;142(3598):1485–1487.

[37] Ohl C, Stockem W. Distribution and Function of Myosin II as a Main Constituent of the Microfilament System in Physarum Polycephalum. European Journal of Protistology. 1995 May;31(2):208–222.

[38] Kukulies J, Brix K, Stockem W. Studies on Microplasmodia of Physarum polycephalum. VI. Functional analysis of a cortical and fibrillar actin system by use of fluorescent-analog cytochemistry. Cell and Tissue Research. 1987 Oct;250(1):125–134.

[39] Koya S, Ueda T. The Onset of Rhythmic Streaming in the Physarum Plasmodium. ACH, models in chemistry. 1998;135(3):297–304.

[40] Rieu JP, Delanöe-Ayari H, Takagi S, Tanaka Y, Nakagaki T. Periodic Traction in Migrating Large Amoeba of Physarum polycephalum. Submitted;.

[41] Willert CE, Gharib M. Digital Particle Image Velocimetry. Experiments in Fluids. 1991 Jan;10(4):181–193.

[42] Brix K, Stockem W. Studies on Microplasmodia of Physarum polycephalum. V. Correlation of Cell Surface Morphology, Microfilament Organization and Motile Activity. Cell Biology International Reports. 1987 Jun;11(7):529–536.

[43] Dembo M, Wang YL. Stresses at the Cell-to-Substrate Interface During Locomotion of Fibroblasts. Biophysical Journal. 1999 Apr;76(4):2307–2316.

[44] Rieu JP, Barentin C, Maeda Y, Sawada Y. Direct Mechanical Force Measurements During the Migration of Dictyostelium Slugs Using Flexible Substrata. Biophysical Journal. 2005 Nov;89(5):3563–3576.

[45] Strychalski W, Guy RD. A Computational Model of Bleb Formation. Mathematical Medicine and Biology : A Journal of the IMA. 2013 Jun;30(2):115–130.

[46] Radszuweit M, Engel H, Bär M. An Active Poroelastic Model for Mechanochemical Patterns in Protoplasmic Droplets of Physarum polycephalum. PLoS ONE. 2014;9(6):e99220.

[47] Strychalski W, Copos CA, Lewis OL, Guy RD. A Poroelastic Immersed Boundary Method with Applications to Cell Biology. Journal of Computational Physics. 2015;282(0):77 – 97.

[48] Hayase M, Maekawa A, Yubisui T, Minami Y. Properties, Intracellular Localization, and Stage-Specific Expression of Membrane-Bound Beta-Glucosidase, BglM1, From Physarum Polycephalum. The International Journal of Biochemistry & Cell Biology. 2008;40(10):2141–2150.

[49] Srinivasan M, Walcott S. Binding Site Models of Friction Due to the Formation and Rupture of Bonds: State-Function Formalism, Force-Velocity Relations, Response to Slip Velocity Transients, and Slip Stability. Physical Review E. 2009;80(4):046124.

[50] Jay PY, Pham PA, Wong SA, Elson EL. A Mechanical Function of Myosin II in Cell Motility. Journal of Cell Science. 1995 Jan;108 (Pt 1):387–393.

[51] Tozluoğlu M, Tournier AL, Jenkins RP, Hooper S, Bates PA, Sahai E. Matrix Geometry Determines Optimal Cancer Cell Migration Strategy and Modulates Response to Interventions. Nature Cell Biology. 2013 Jul;15(7):751–762.

[52] Blanchoin L, Boujemaa-Paterski R, Sykes C, Plastino J. Actin Dynamics, Architecture, and Mechanics in Cell Motility. Physiological Reviews. 2014 Jan;94(1):235–263.

[53] Tanaka Y, Ito K, Nakagaki T, Kobayashi R. Mechanics of Peristaltic locomotIon and Role of Anchoring. Journal of the Royal Society Interface. 2012 Feb;9(67):222–233.

[54] Umedachi T, Idei R, Ito K, Ishiguro A. True-Slime-Mould-Inspired Hydrostatically Coupled Oscillator System Exhibiting Versatile Behaviours. Bioinspiration & Biomimetics. 2013 Sep;8(3):035001.

[55] Álvarez-González B, Bastounis E, Meili R, del Álamo JC, Firtel R, Lasheras JC. Cytoskeletal mechanics regulating amoeboid cell locomotion. Applied mechanics reviews. 2014;66(5):050804.

[56] Umedachi T, Idei R, Ito K, Ishiguro A. True-slime-mould-inspired hydrostatically coupled oscillator system exhibiting versatile behaviours. Bioinspiration & biomimetics. 2013;8(3):035001.

[57] Kamiya N. Protoplasmic streaming. vol. 8 of Protoplasmatologia. Springer; 1959.

[58] Allen RD, Allen NS. Cytoplasmic streaming in amoeboid movement. Annual review of biophysics and bioengineering. 1978;7(1):469–495.

[59] Goldstein RE, van de Meent JW. A physical perspective on cytoplasmic streaming. Interface focus. 2015;5(4):20150030.

[60] Aldrich H. Cell Biology of Physarum and Didymium V1: Organisms, Nucleus, and Cell Cycle. Elsevier; 2012.

[61] Nagai R, Yoshimoto R, Kamiya N. Cyclic production of tension force in the plasmodial strand of Physarum polycephalum and its relation to microfilament morphology. Journal of cell science. 1978;33(1):205–225.

[62] Rieu JP, Delanoë-Ayari H, Takagi S, Tanaka Y, Nakagaki T. Periodic traction in migrating large amoeba of Physarum polycephalum. Journal of The Royal Society Interface. 2015;12(106).

[63] Yoshiyama S, Ishigami M, Nakamura A, Kohama K. Calcium wave for cytoplasmic streaming of Physarum polycephalum. Cell biology international. 2010;34(1):35–40.

[64] Zhang S, Guy R, del Alamo JC. Coordinations of Intracellular Flow, Calcium Signal and Cellular Contraction in Migrating Physarum. In: Proc. of the 9th EAI Int. Conf. on Bio-inspired Information and Communications Technologies (formerly BIONETICS); 2016. p. 609–610.

[65] Rodiek B, Takagi S, Ueda T, Hauser MJ. Patterns of cell thickness oscillations during directional migration of Physarum polycephalum. European Biophysics Journal. 2015;44(5):349–358.

[66] Alonso S, Strachauer U, Radszuweit M, Bär M, Hauser MJB. Oscillations and uniaxial mechanochemical waves in a model of an active poroelastic medium: Application to deformation patterns in protoplasmic droplets of Physarum polycephalum. Physica D: Nonlinear Phenomena. 2016;318–319:58 – 69. Nonlinear Models in Molecular and Cell Biology.

[67] Tse JR, Engler AJ. Preparation of Hydrogel Substrates with Tunable Mechanical Properties. Current protocols in Cell Biology. 2010 Jun;Chapter 10:10.16.1–10.16.16.

[68] Meili R, Alonso-Latorre B, Del Álamo JC, Firtel RA, Lasheras JC. Myosin II Is essential for the spatiotemporal organization of traction forces during cell motility. Molecular biology of the cell. 2010;21(3):405–417.

[69] Delanoë-Ayari H, Rieu J, Sano M. 4D traction force microscopy reveals asymmetric cortical forces in migrating Dictyostelium cells. Physical Review Letters. 2010;105(24):248103.

[70] Alim K, Amselem G, Peaudecerf F, Brenner MP, Pringle A. Random network peristalsis in Physarum polycephalum organizes fluid flows across an individual. Proceedings of the National Academy of Sciences. 2013;110(33):13306–13311.

[71] Romanovskii YM, Teplov V. The physical bases of cell movement. The mechanisms of self-organisation of amoeboid motility. Physics-Uspekhi. 1995;38(5):521–542.

[72] Gawlitta W, Wolf KV, Hoffmann HU, Stockem W. Studies on Microplasmodia of Physarum polycephalum. I. Classification and Locomotion Behavior. Cell and tissue research. 1980;209(1):71–86.

[73] Takagi S, Ueda T. Emergence and transitions of dynamic patterns of thickness oscillation of the plasmodium of the true slime mold Physarum polycephalum. Physica D: Nonlinear Phenomena. 2008;237(3):420 – 427.

[74] Takagi S, Ueda T. Annihilation and creation of rotating waves by a local light pulse in a protoplasmic droplet of the Physarum plasmodium. Physica D: Nonlinear Phenomena. 2010;239(11):873 – 878. Emergent Phenomena in Spatially Distributed SystemsIn Honor of Stefan C. MüllerEmergent Phenomena in Spatially Distributed Systems.

[75] Zhang S, Guy R, Del Alamo JC. Feedback between intracellular flow, signaling and active stresses in Physarum plasmodial fragments. In: APS Meeting Abstracts; 2016. .

[76] Barnhart EL, Allen GM, Jülicher F, Theriot JA. Bipedal Locomotion in Crawling Cells. Biophysical Journal. 2010;98(6):933 – 942.

[77] Bastounis E, Meili R, Alonso-Latorre B, del Álamo JC, Lasheras JC, Firtel RA. The SCAR/WAVE complex is necessary for proper regulation of traction stresses during amoeboid motility. Molecular biology of the cell. 2011;22(21):3995–4003.

[78] Donahue BS, Abercrombie RF. Free diffusion coefficient of ionic calcium in cytoplasm. Cell Calcium. 1987;8(6):437 – 448.

[79] Kamm KE, Stull JT. The function of myosin and myosin light chain kinase phosphorylation in smooth muscle. Annual review of pharmacology and toxicology. 1985;25(1):593–620.

[80] Karaki H, Ozaki H, Hori M, Mitsui-Saito M, Amano KI, Harada KI, et al. Calcium movements, distribution, and functions in smooth muscle. Pharmacological reviews. 1997;49(2):157–230.

[81] Endo M. Calcium release from the sarcoplasmic reticulum. Physiological Reviews. 1977;57(1):71–108.

[82] Watras J, Ehrlich BE, et al. Bell-shaped calcium-response curves of lns (l, 4, 5) P3-and calcium-gated channels from endoplasmic reticulum of cerebellum. Nature. 1991;351(6329):751.

[83] Clapham DE. Calcium signaling. Cell. 2007;131(6):1047–1058.

[84] Rizzuto R, Pozzan T. Microdomains of intracellular Ca2+: molecular determinants and functional consequences. Physiological reviews. 2006;86(1):369–408.

[85] Zhang Y, Kawamichi H, Tanaka H, Yoshiyama S, Kohama K, Nakamura A. Calcium-dependent regulation of the motor activity of recombinant full-length Physarum myosin. Journal of biochemistry. 2012;152(2):185–190.

[86] Nakamura A, Kohama K. Calcium regulation of the actin-myosin interaction of Physarum polycephalum. International review of cytology. 1999;191:53–98.

[87] Smith D, Saldana R. Model of the Ca2+ oscillator for shuttle streaming in Physarum polycephalum. Biophysical journal. 1992;61(2):368.

[88] Colley DG, Bustinduy AL, Secor WE, King CH. Human schistosomiasis. The Lancet. 2014;383(9936):2253–2264.

[89] Mair G, Maule A, Day T, Halton D. A confocal microscopical study of the musculature of adult Schistosoma mansoni. Parasitology. 2000;121(2):163–170.

[90] Brown H, Halliwell M, Qamar M, Read A, Evans J, Wells P. Measurement of normal portal venous blood flow by Doppler ultrasound. Gut. 1989;30(4):503–509.

[91] Bilbao A, Wajnryb E, Vanapalli SA, Blawzdziewicz J. Nematode locomotion in unconfined and confined fluids. Physics of Fluids. 2013;25(8):081902.

[92] Lebois F, Sauvage P, Py C, Cardoso O, Ladoux B, Hersen P, et al. Locomotion control of Caenorhabditis elegans through confinement. Biophysical journal. 2012;102(12):2791–2798.

[93] Mesce KA, Pierce-Shimomura JT. Shared strategies for behavioral switching: understanding how locomotor patterns are turned on and off. Frontiers in behavioral neuroscience. 2010;4:49.

[94] McKee A, Voltzow J, Pernet B. Substrate attributes determine gait in a terrestrial gastropod. The Biological Bulletin. 2013;224(1):53–61.

[95] Gillis GB. Environmental effects on undulatory locomotion in the American eel Anguilla rostrata: kinematics in water and on land. Journal of Experimental Biology. 1998;201(7):949–961.

[96] Boussinesq J. Mémoire sur l'influence des Frottements dans les Mouvements Réguliers des Fluids. J Math Pures Appl. 1868;13(2):377–424.

[97] Gómez-González M, Del Alamo JC. Two-point particle tracking microrheology of nematic complex fluids. Soft matter. 2016;12(26):5758–5779.

[98] Mason TG, Weitz D. Optical measurements of frequency-dependent linear viscoelastic moduli of complex fluids. Physical review letters. 1995;74(7):1250.

[99] Papaioannou TG, Stefanadis C. Vascular wall shear stress: basic principles and methods. Hellenic J Cardiol. 2005;46(1):9–15.

[100] Smith A. Cephalopod sucker design and the physical limits to negative pressure. Journal of Experimental Biology. 1996;199(4):949–958.

[101] Weiss JN. The Hill equation revisited: uses and misuses. The FASEB Journal. 1997;11(11):835–841.

[102] DeLean A, Munson P, Rodbard D. Simultaneous analysis of families of sigmoidal curves: application to bioassay, radioligand assay, and physiological dose-response curves. American Journal of Physiology-Endocrinology And Metabolism. 1978;235(2):E97.

[103] Shuhua X, Binggui S, Chollet J, Utzinger J, Tanner M. Tegumental changes in adult Schistosoma mansoni harbored in mice treated with artemether. Journal of Parasitology. 2000;86(5):1125–1132.

[104] Manneck T, Haggenmüller Y, Keiser J. Morphological effects and tegumental alterations induced by mefloquine on schistosomula and adult flukes of Schistosoma mansoni. Parasitology. 2010;137(1):85–98.

[105] Machado-Silva JR, Pelajo-Machado M, Lenzi HL, Gomes DC. Morphological study of adult male worms of Schistosoma mansoni Sambon, 1907 by confocal laser scanning microscopy. Memórias do Instituto Oswaldo Cruz. 1998;93:303–307.